# NOVEL MEASUREMENTS OF THE FREQUENCY DEPENDENT MICROWAVE SURFACE IMPEDANCE OF CUPRATE THIN FILM SUPERCONDUCTORS

by

James Clay Booth

Dissertation submitted to the Faculty of the Graduate School
of The University of Maryland in partial fulfillment
of the requirements for the degree of
Doctor of Philosophy
1996


**UNIVERSITY OF MARYLAND**

**DEPARTMENT OF PHYSICS**

**COLLEGE PARK, MARYLAND 20742**

# Abstract

Title of Dissertation: Novel Measurements of the Frequency Dependent Microwave Surface Impedance of Cuprate Thin Film Superconductors

James Clay Booth, Doctor of Philosophy, 1996

Dissertation directed by: Professor Steven M. Anlage
Department of Physics

A novel broadband experimental technique has been developed to study the microwave electrodynamics of high $T_c$ superconducting films over the continuous frequency range from 45 MHz - 50 GHz. In zero applied magnetic field this technique is used to study thermal fluctuation effects in the ac conductivity at the normal to superconducting phase transition. In the presence of a perpendicular external magnetic field, the measurement system is employed to study the motion of magnetic vortices in the mixed state at microwave frequencies. Both experimental investigations yield fundamental new information about the nature of superconductivity in the high $T_c$ materials that is unobtainable using conventional fixed-frequency microwave techniques.

From measurements in zero field, experimental evidence is presented for critical behavior in the frequency and temperature dependent microwave conductivity of $YBa_2Cu_3O_{7-\delta}$ (YBCO) thin films as the transition temperature is approached from above. For $T-T_c \leq 1$ K, the data shows scaling behavior in both the magnitude and phase of the frequency-dependent fluctuation conductivity over three decades in frequency, with critical exponents $\nu=1.0$-$1.5$ and $z=2.3$-$3.0$. These results describe a

fluctuation lifetime that diverges much more quickly than predicted by Gaussian fluctuation theory as the transition temperature is approached from above. In addition, by utilizing the critical exponents derived from the frequency dependent analysis, it is possible to collapse both the temperature dependent and frequency dependent data onto the same universal curve within the critical region, which is estimated to be 1-2 K wide above $T_c$.

From measurements of YBCO films in a perpendicular magnetic field, it is found that for a range of temperatures and fields there exists a cross-over frequency $f_x$ which separates two very different regimes of vortex motion. The experiments show that below $f_x$ the response of the vortex system can be well described by scaling theories based on the vortex liquid to glass phase transition, which explicitly take into account vortex-vortex interaction. At high enough frequencies ($f>f_x$) the experimental data is more successfully described by conventional single-particle (or mean-field) theories of vortex motion, which ignore inter-vortex interactions.

# NOVEL MEASUREMENTS OF THE FREQUENCY DEPENDENT MICROWAVE SURFACE IMPEDANCE OF CUPRATE THIN FILM SUPERCONDUCTORS

by

James Clay Booth

Dissertation submitted to the Faculty of the Graduate School
of The University of Maryland in partial fulfillment
of the requirements for the degree of
Doctor of Philosophy
1996

Advisory Committee:

Assistant Professor Steven M. Anlage, Chair/Advisor
Professor H. Dennis Drew
Professor Richard L. Greene
Professor Chi H. Lee
Professor Christopher Lobb

# Dedication

To my parents

# Acknowledgements

Earning a graduate degree is about learning and the pursuit of knowledge. For me the most valuable resource for this endeavor has been the many people with whom I have interacted during the tenure of my graduate studies. There are so many different facets to a graduate degree and career in physics research that one cannot hope to succeed without the involvement of a large number of extremely talented people who must be willing and eager to share their knowledge freely. I feel that I am extremely fortunate to have been able to pursue my graduate degree in such an intellectually rich and stimulating environment.

I would like to acknowledge my thesis advisor, Professor Steven Anlage, for skillfully guiding me through all the phases of my research at the University of Maryland. I have come to appreciate having an advisor who is actively involved with his students, and who is extremely knowledgeable about virtually every aspect of experimental physics. I also appreciated being allowed the freedom to pursue my own independent ideas and directions for my research.

I also want to acknowledge Dr. Dong Ho Wu for teaching me a lot about being a successful research physicist (mostly by example), and for his patience in teaching me the art of technical writing. I think I learned the most from my close interaction with my fellow high frequency group members Mike Pambianchi and Jian Mao, who provided helpful discussions on a daily basis. I would also like to thank the undergraduate students who worked in our lab, Tony De Marco and Ali Gokirimak, for the considerable help they also have provided.

I would also like to acknowledge the help of my fellow graduate students in the Center for Superconductivity Research. In particular I want to thank the people who provided samples for my measurements, including Alp Findikoglu, Chris Doughty,

M.(Raj) Rajeswari, Alberto Pique, Vitaly Talyanski, and Chuhee Kwon. I also want to thank Alp, Raj and Alberto for teaching me the basics of pulsed laser deposition.

I am also indebted to the staff of the Center for Superconductivity Research, including Belta Pollard, Monica Pogue and Dawn Leavell. I would also like to thank Brian Straughn and Doug Bensen, who were happy to help no matter how many problems I brought to them. I would also like to thank Mrs. Jane Hessing of the Physics Department, for answering countless questions about departmental requirements and forms.

I would also like to thank the faculty of the Center for Superconductivity Research, who provided a wealth of experience and knowledge about an incredibly broad range of subjects. In particular I would like to thank the members of my Dissertation Committee, Professors Dennis Drew, Rick Greene, Chi Lee and Chris Lobb. I would also like to thank Chris Lobb, Fred Wellstood and Dong Ho Wu for providing letters of reference.

I am most indebted to my parents for providing both the motivation and support for my somewhat lengthy education. I owe to them my ambition and the self-confidence necessary to achieve my goals.

Finally I would like to thank my wife Susie for bearing with me for such a long time while I pursued my own educational and professional goals. I cannot even begin to count the number of different ways that she has helped me along the way. Much of the sacrifice and hardship that is necessary to earn a Ph. D. has been borne by her, and I could not have accomplished it without her.

James C. Booth

College Park, Maryland

June 6, 1996

# Table of Contents

# List of Tables

# List of Figures

# Chapter 1
# Introduction

## 1.1 Surface Impedance Measurements of Superconductors

Surface impedance measurements at microwave frequencies have historically provided a wealth of essential information about the fundamental properties of the superconducting state.[1,2] Microwave experiments typically have very high sensitivity, allowing for detailed measurements of the very low losses characteristic of superconductors. In addition, measurements at finite frequencies allow for the determination of the electrodynamic response of both the superconducting condensate as well as the quasiparticle excitations that exist at finite temperatures. Microwave measurements have the advantage that the frequency is still well below the maximum gap frequency, and contributions from both the condensate and the quasiparticles are large enough to be measurable.

In recent years, microwave surface impedance measurements have played a vital role in the ongoing effort to understand the mechanism of superconductivity in the newly discovered high transition temperature (high $T_c$) superconductors.[3,4] In particular, microwave penetration depth measurements on single crystals have provided compelling evidence in the effort to determine the symmetry of the order parameter in the high $T_c$ materials.[5,6] Microwave measurements also provide a very stringent test of sample quality, and are therefore well suited to help separate intrinsic and extrinsic effects in these exotic and complicated materials, and also aid considerably in efforts to improve the quality of these materials.[7]

In addition to fundamental aspects such as the pairing state symmetry of the high $T_c$ superconductors, microwave measurements can also be used to help develop a general phenomenological picture of superconductivity in these materials, in the

absence of a fundamental theory. Microwave techniques have also been used extensively in studying the dynamic properties of magnetic vortices in the mixed state of the high $T_c$ superconductors, and can be used to determine the relevant physical parameters of these materials, such as the lower critical field $H_{c1}(T)$.[8]

Another very compelling reason to focus on the microwave properties of superconductors is because passive microwave devices represent a significant potential commercialization of high $T_c$ superconductivity. Rapid progress in film growth and in the optimization of materials properties has allowed for the successful fabrication of many practical superconducting devices, such as narrow band filters, delay lines, high-Q oscillators and high-performance antennas, all of which operate at temperatures above 77 K.[9,10] The very low values for the surface resistance obtainable with high $T_c$ superconductors (approximately 10-1000 times lower than the surface resistance of copper at 77 K at microwave frequencies) are very attractive for use in rf and microwave components and can yield orders of magnitude superior device performance compared to currently available technology, and at reasonable cost. Such a low surface resistance can even result in applications which are not possible at all using normal metal conductors.[10] In addition, the non-dispersive (frequency-independent) penetration depth of superconductors can be beneficial for some applications, such as broadband delay lines. The use of superconducting materials also results in smaller, denser circuits than is possible using normal metal conductors and conventional technology.

The use of high $T_c$ materials in actual commercial microwave circuits requires detailed knowledge of the microwave response of these new materials. Of particular concern is the fact that the high $T_c$ materials possess some detrimental non-linear properties,[11] the origin of which are not currently understood. These non-linear effects, absent in normal metal conductors, seriously limit the usefulness of these

materials for some commercial applications. A thorough understanding of the behavior of the high $T_c$ materials at microwave frequencies is essential in order to further the technological and commercial applications of high $T_c$ superconductivity.

The main focus of this thesis is on microwave experiments that explore the frequency dependence of the electrodynamic properties of high $T_c$ superconductors. In what follows, the difference in approach between resonant and broadband microwave measurements is discussed, with the emphasis being placed on measurements of the non-resonant variety. This is followed in section 1.2 by some motivation as to what can be learned from broadband measurements applied to the high $T_c$ superconductors.

### 1.1.1 Resonant Measurements

Most conventional microwave measurements of the surface impedance rely on resonance techniques, in which the sample under test forms all or part of a resonant structure. One then measures changes in the resonant frequency ($f_0$) and quality factor (Q) of the resonance as a function of temperature or some other independent variable. The resonant frequency shift and Q are then related to the surface resistance $R_s$ and change in penetration depth $\lambda$ of the superconductor under study. Such resonant techniques can achieve extremely high resolution for $R_s$ (~1-10 $\mu\Omega$) and $\Delta\lambda$ (~1 Å), due in part to the fact that the measured quantities in these experiments are frequencies, which can be measured with very high precision (1 part in $10^9$ is not uncommon). The value of resonant measurements for determining intrinsic properties of the superconducting state can not be understated. But while such techniques can potentially provide a very sensitive means of studying the surface impedance as a function of temperature or sometimes magnetic field, they are necessarily limited to at most a few discrete frequency points, and therefore cannot provide much information on how the surface impedance varies with frequency. The inability of resonance

techniques to measure any frequency dependence can be a serious drawback when interpreting experimental data, since it is often possible to describe results obtained at a single frequency by an uninformative parametrization of the data. The behavior of a system at many different frequencies will provide a much more stringent test of any theoretical model.

Some resonant techniques, such as stripline resonators,[12] obtain information about the frequency dependence of the surface impedance by measuring a number of higher order harmonics of a given fundamental mode. While these techniques can provide a measure of the frequency dependence in the low-loss superconducting state where non-resonant methods are not sensitive, one must be very careful in evaluating background contributions and other corrections at different frequencies, since different resonant modes have different microwave field and current distributions.

### 1.1.2 Broadband Measurements

Non-resonant experiments at microwave frequencies typically measure the transmission or reflection of a microwave signal incident on the sample. Since they do not make use of a resonant mode, there is much more freedom in choosing an operating frequency in these experiments than in their resonant counterparts. Some of the most important early microwave measurements on superconductors were the transmission measurements of Glover and Tinkham[2]. Broadband measurements are usually much less sensitive than high-Q resonant measurements, because the measured quantity is typically a voltage, not a frequency. In addition, in order to accurately measure both the real and imaginary parts of the response, one must use phase-sensitive measurement techniques, which become increasingly more difficult as the measurement frequency increases and the signal wavelength becomes much smaller than the measurement apparatus.

An example of a non-resonant technique that has been applied to the measurement of conventional superconductors is the waveguide transmission measurement.[13,14] In experiments of this type, a thin superconducting film is inserted between two sections of waveguide, and the ratio of the signal transmitted through the sample to the incident signal is measured. The complex conductivity of the sample can then be extracted from the measured transmission coefficient. Microwave transmission measurements of this kind have more recently been applied to measurements of the high $T_c$ superconductors at 9 GHz[15], and from 26.5 - 40 GHz[16]. Other transmission measurements on superconductors include quasi-optical techniques used at 60 GHz. [17] Microwave transmission measurements have also been used in combination with parallel plate resonator measurements[18] to determine an absolute value for the penetration depth $\lambda$ in high $T_c$ thin films. Waveguide transmission measurements have also been used to measure the properties of high $T_c$ thin films in magnetic fields (at 35 GHz).[19] Because of its non-resonant nature, the waveguide transmission measurement technique can be applied to investigate the frequency dependence of the electrodynamic response of superconductors (often in practice by measuring the temperature dependent conductivity at a number of different frequencies). Such measurements are however limited to the single mode operating frequency range of the waveguide used (for example, the operating frequency for an X-band waveguide is ~ 8-12 GHz), and have the disadvantage that it can be quite difficult to extract the surface impedance from the experimentally measured quantities.[20] In addition, there can be problems associated with the leakage of the signal around (rather than transmission through) the sample.

Non-resonant experiments at higher frequencies use coherent time-domain spectroscopy to measure the frequency dependent conductivity in the 500 GHz - 2.5 THz range.[21,22] These experiments employ a very short electromagnetic pulse and

obtain the frequency response by Fourier analysis. At still higher frequencies one can use far-infrared techniques, which measure the magnitude of the transmitted signal as a function of frequency, and can obtain the full complex conductivity versus frequency using a Kramers-Kronig relationship.[23]

The measurement system described in this work is a broadband type, but is different from the waveguide transmission measurements in a number of significant ways. This technique, referred to as the Corbino reflection technique,[24] measures the complex reflection coefficient (from 45 MHz - 50 GHz) of a thin film which forms an electrical short across a coaxial transmission line. The Corbino reflection technique is a swept-frequency method, which allows for the direct measurement of the full complex resistivity (or conductivity) of thin film samples as a function of frequency over three decades in the rf/microwave/mm wave range. The measurement utilizes the TEM mode in a coaxial geometry in order to maximize the frequency range accessible to the measurement. The coaxial transmission lines used here support exclusively the TEM mode up to approximately 70 GHz, and can be used at frequencies all the way down to dc due to the absence of a lower cutoff frequency for the TEM mode. The use of the TEM mode also results in a relatively simple field distribution within the thin film sample. Also, for the geometries used here, the measured reflection coefficient is rather simply related to the complex resistivity of the sample, which is a fundamentally interesting quantity.

## 1.2 Frequency Dependent Microwave Measurements

There are many fundamentally and practically interesting phenomena that can be studied using frequency dependent measurements in the microwave range. Access to the frequency dependence provides direct information about the time dependence of the system under study. If there are physical processes that take place on time scales of the

order of 1/f seconds (where $4.5 \times 10^7 \leq f \leq 5 \times 10^{10}$), then one can expect the frequency response of the system to change as the frequency is swept through the current measurement range. Due to the fact that most microwave measurements are resonant in nature, phenomena at microwave frequencies are primarily viewed from a fixed frequency point of view. As will be shown throughout this work, access to the frequency dependence can give a different and often valuable new perspective on physical phenomena.

The frequency dependent measurements described here are used to investigate two distinct, although related, physical systems in superconductors. The first application of the technique to be described is the measurement of thermal fluctuation effects on the conductivity of YBCO thin films in the vicinity of the superconducting phase transition in zero magnetic field. It is found that frequency dependent measurements can yield valuable information about the lifetime of fluctuation-induced Cooper pairs above $T_c$, information that is inaccessible using the temperature dependence measurements alone. Such measurements provide evidence of critical behavior at the phase transition in the high $T_c$ materials.

The second system studied extensively here is the dynamics of magnetic vortices in superconducting YBCO thin films in large magnetic fields. In these systems it is found that for certain regions of parameter space, the response of the system can change character dramatically depending on the driving frequency. Both sets of experimental studies illustrate the discovery of new or different time scales that add significantly to our understanding of high $T_c$ superconductors.

## Chapter 1 References

[1] A.B. Pippard, Proc. Roy. Soc. **A191**, 370 (1947).

[2] R.E. Glover, III, and M. Tinkham, Phys. Rev. **108**, 243 (1957).

[3] J.G. Bednorz and K.A. Müller, Z. fur Phys **64**, 189 (1986).

[4] M.K. Wu, J.R. Ashburn, C.J. Torng, P.H. Hor, R.L. Meng, L. Gao, Z.J. Huang, Y. Q. Wang, C.W. Chu, Phys. Rev. Lett. **58**, 908 (1987).

[5] W. N. Hardy et al., Phys. Rev. Lett. **70**, 3999 (1993).

[6] Jian Mao, D. H. Wu, J.L. Peng, R.L. Greene, and Steven M. Anlage, Phys. Rev. B **51**, 3316 (1995).

[7] Jian Mao, Ph. D. thesis, University of Maryland, 1995.

[8] Dong-Ho Wu and S. Sridhar, Phys. Rev. Lett., **65**, 2074 (1990).

[9] N. Newman and W. G. Lyons, J. Supercond. **6**, 119 (1993).

[10] Z. Y. Shen, "High - Temperature Superconducting Microwave Circuits", Artech House, Boston (1994).

[11] D. E. Oates, A. C. Anderson, D. M. Sheen, S. M. Ali, IEEE Trans. Microwave Th. Tech. **39**, 1522 (1991); D. E. Oates, P. P. Nguyen, G. Dresselhaus, M. S. Dresselhaus, C. W. Lam, and S. M. Ali, J. Supercond. **5**, 361 (1992).

[12] S. Revenaz, D.E. Oates, D. Labbe-Lavigne, G. Dresselhaus, and M.S. Dresselhaus, Phys. Rev. B **50**, 1178 (1994).

[13] N.M. Rugheimer, A. Lehoczky, and C.V. Briscoe, Phys. Rev. **154**, 414 (1967).

[14] D.A. Soderman and K. Rose, J. Appl. Phys. **39**, 2610 (1968).

[15] C.C. Nichols, N.S. Shiren, R.B. Laibowitz, and T.G. Kazyaka, Phys. Rev. B **38**, 11970 (1988).

[16] F.A. Miranda, W.L. Gordon, K.B. Bhasin, V.O. Heinen, and J.D. Warner, J. Appl. Phys. **70**, 5450 (1991).

[17] W. Ho, P.J. Hood, W.F. Hall, P. Kobrin, A.B. Harker, and R.E. DeWames, Phys. Rev. B **38**, 7029 (1988).

[18] R. C. Taber, P. Merchant, R. Hiskes, S.A. DiCarolis, and M. Narbutovskih, J.

Supercond. **5**, 371 (1992).

[19] E.K. Moser, W.J. Tomasch, J.K. Furdyna, M.W. Coffey, and J.R. Clem, IEEE Trans. Appl. Supercon. **3**, 1119 (1993).

[20] E.K. Moser, W.J. Tomasch, M.J. McClorey, J. K. Furdyna, M.W. Coffey, C.L. Petiette-Hall, and S.M. Schwarzbek, Phys. Rev. B **49,** 4199 (1994).

[21] M. C. Nuss, P.M. Mankiewich, M.L. O'Malley, E.H. Westerwick, and P.B. Littlewood, Phys. Rev. Lett **66**, 3305 (1991).

[22] B. Parks, S. Spielman, J. Orenstein, D. T. Nemeth, F. Ludwig, J. Clarke, P. Merchant, D. J. Lew, Phys. Rev. Lett. **74**, 3265 (1995).

[23] H.-T. S. Lihn, S. Wu, H.D. Drew, S. Kaplan, Qi Li, and D.B. Fenner, Phys. Rev. Lett. **76**, 3810 (1996).

[24] J.C. Booth, Dong Ho Wu, and Steven M. Anlage, Rev. Sci. Instrum. **65**, 2082 (1994).

# Chapter 2

# The Corbino Reflection Measurement Technique

## 2.1 The Corbino Disk Geometry

In this chapter the non-resonant experimental technique is described which allows the surface impedance of superconducting thin films to be measured at arbitrary frequencies in the rf and microwave range (from 45 MHz - 50 GHz). Measurements at lower frequencies have been accomplished using other methods.[1,2,3] The measurement technique, shown schematically in Fig. 2.1, employs a vector network analyzer to measure the complex reflection coefficient ($S_{11}$) of a thin film which forms an electrical short across the end of a coaxial cable. Once the complex reflection coefficient is measured, standard transmission line theory is used to extract the complex surface impedance of the film from $S_{11}$.[4] The measurement takes advantage of a special geometry in which the sample forms a thin disc between the inner and outer conductors of the coaxial cable. The use of such a measurement geometry -- referred to as a Corbino disk[5] geometry -- means that currents in the film flow in the radial

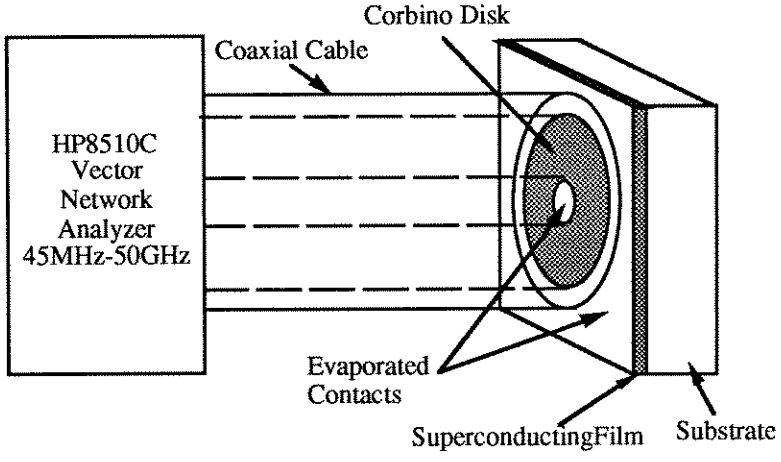


Fig. 2.1. Schematic diagram of Corbino measurement configuration

direction, producing magnetic fields only in the azimuthal direction, everywhere parallel to the surface of the film. The effects of the edges of the film are therefore effectively eliminated in the Corbino geometry (compare with a rectangular or microbridge geometry, where self fields due to the current can be perpendicular to the film surface, particularly at the edges). This geometry is particularly beneficial when studying the motion of magnetic vortices in the mixed state of superconductors, since the sample edge contribution to the creation and/or pinning[6] of vortices has been eliminated. An additional advantage of the technique is that it allows for the surface impedance to be determined over a wide range of experimental parameters, including temperature, magnetic field, frequency, rf power, and dc bias current.

The Corbino reflection measurement technique developed out of the historical use of the Corbino geometry for dc transport measurements.[5] Bluzer and collaborators[7] used the Corbino geometry to measure time-domain picosecond quasiparticle dynamics in zero field in low- and high- $T_c$ superconducting films. Their basic technique has been adapted to the frequency domain, and to the study of vortex dynamics and fluctuation conductivity in high $T_c$ superconductors.

This chapter describes in detail the application of the Corbino reflection technique to measurements of the surface impedance of superconducting thin films. Section 2.2 will give an overview of the two different implementations of the experimental technique used in this thesis, and section 2.3 will give a description of the crucial interface region between the coaxial transmission line and the thin film under study. This will be followed in section 2.4 by a discussion of absolute power measurements in the Corbino reflection geometry. Section 2.5 will then discuss the details of the preparation of superconducting thin film samples for the measurements presented here, and section 2.6 will briefly describe the dc resistivity measurements used to complement the microwave experiments.

## 2.2 Experimental Overview

Two different experimental set-ups are used to measure the reflection coefficient, depending on whether or not an external dc magnetic field is required. For both experimental configurations, the thin film under study is used to terminate a coaxial transmission line, and the complex reflection coefficient $S_{11}$ is measured over the continuous frequency range 45 MHz - 50 GHz using a Hewlett-Packard HP8510C vector network analyzer. The microwave source is a Hewlett-Packard HP83651A synthesized sweeper which operates over the frequency range 45 MHz - 50 GHz with 1 Hz resolution. The network analyzer is operated in step sweep mode to ensure phase coherence at each frequency point. Related experimental techniques use reflection coefficient measurements to obtain the complex dielectric constant of liquids[8,9] and solids[10,11] at room temperature. In our case, the dependence of the reflection coefficient on temperature, magnetic field, and frequency is of primary interest.

In addition to measurements at rf and microwave frequencies, this technique also allows for 2-point dc measurements to be performed. A dc bias current is applied to the coaxial cable, and the resulting voltage drop between the inner and outer conductors of the coaxial cable is measured at the location of the network analyzer (an rf choke internal to the HP8510C test set protects the high frequency detectors from the dc current). This ability to make dc measurements simultaneously with the microwave measurements is important because it allows direct comparison of the high frequency response with the more conventional dc behavior.

### 2.2.1 Measurements in Zero External Magnetic Field

Fig. 2.2 shows schematically the experimental set-up used for measurements in zero external magnetic field. The sample is mounted on the cold finger of a Janis model ST-100 continuous-flow cryostat, and is connected to the network analyzer by

means of a 0.086 inch outer diameter copper coaxial transmission line, which supports only the TEM mode up to approximately 70 GHz. The dielectric material for the coaxial transmission line is air-articulated PTFE (Teflon), which is used because it has the best available combination of thermal and electrical properties. A number of other coaxial cables with differing dielectric materials were tried, including solid PTFE and Isocore brand[12] PTFE. It was found experimentally that the solid PTFE was considerably more noisy, due to the expansion and contraction of the solid dielectric. The Isocore PTFE had by far the best thermal properties, but the phase velocity changed unpredictably with time at low temperatures. In this experimental configuration, the copper coaxial cable was a severe heat load for the system, and a stainless steel transmission line would have been preferable, but a stainless steel coaxial cable with the required air-articulated PTFE dielectric was not available. In order to minimize attenuation effects at higher frequencies, the transmission line is kept as short as possible, ~ 22 cm for the zero-field measurements.

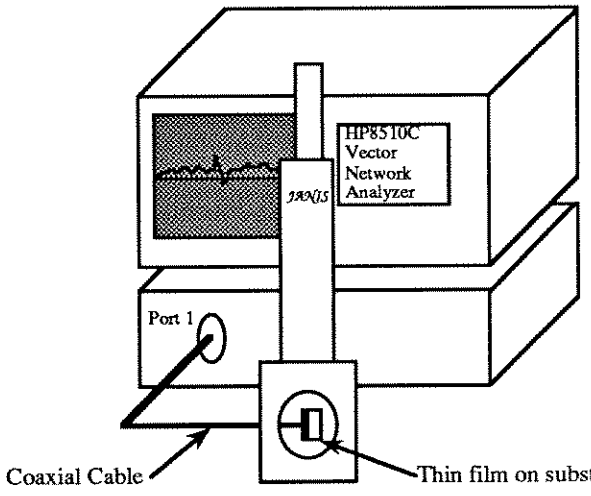


Fig. 2.2. Schematic diagram of experimental set-up for measurements in zero applied magnetic field.

To control the temperature, a silicon diode thermometer was mounted on the cold finger, and a Lakeshore model DRC-93CA temperature controller was used to

stabilize the temperature at the desired value. The temperature of the sample was monitored by an addition temperature sensor located on the cylindrical copper sample housing, because large temperature gradients can be present in this experimental configuration.

Before the sample is loaded into the cryostat, room temperature calibrations are performed directly at the position of the sample at the termination of the transmission line. Then the sample is connected first to the transmission line, and then to the cold finger of the cryostat. The main advantage of this set-up, other than the short transmission line, is the fact that after the transmission line is calibrated, the sample can be connected without disconnecting the transmission line from the test set. This provides the maximum accuracy, and a high quality calibration is crucial for an accurate measurement over such a wide frequency range. After the sample is attached to the cold finger, the cryostat is pumped down to a pressure of ~20 μm Hg before the helium transfer is begun. During the entire measurement, a continuous flow of liquid helium is maintained through the cryostat in order to achieve the necessary cooling power.

Measurements are performed in this configuration by slowly ramping the temperature set point up from its initial value. After the temperature is stabilized at each set point, the frequency dependent reflection coefficient is measured. From the full frequency dependence (usually consisting of 201 frequency points), several values of the reflection coefficient at preselected frequencies are written to a temperature dependent file, and the entire frequency trace is saved at periodic intervals. The data set from a given temperature ramp therefore consists of a file with the temperature-dependence of the reflection coefficient at several fixed frequencies, and a number of files containing the entire frequency dependence at different temperatures.

### 2.2.2 Measurements in Finite Magnetic Field

The experimental set-up used in the magnetic field dependent measurements is shown schematically in Fig. 2.3. In this case, the coaxial transmission line must be approximately 3 meters long in order to reach a Nb-Ti superconducting magnet. The much longer transmission line used for these measurements results in a much smaller measurement signal at high frequencies, and also reduced dynamic range in the incident microwave power at the location of the sample, due to the increased attenuation. The coaxial transmission line used for this set-up is also copper, with the same dielectric material as is used in the zero-field set-up (air-articulated PTFE).

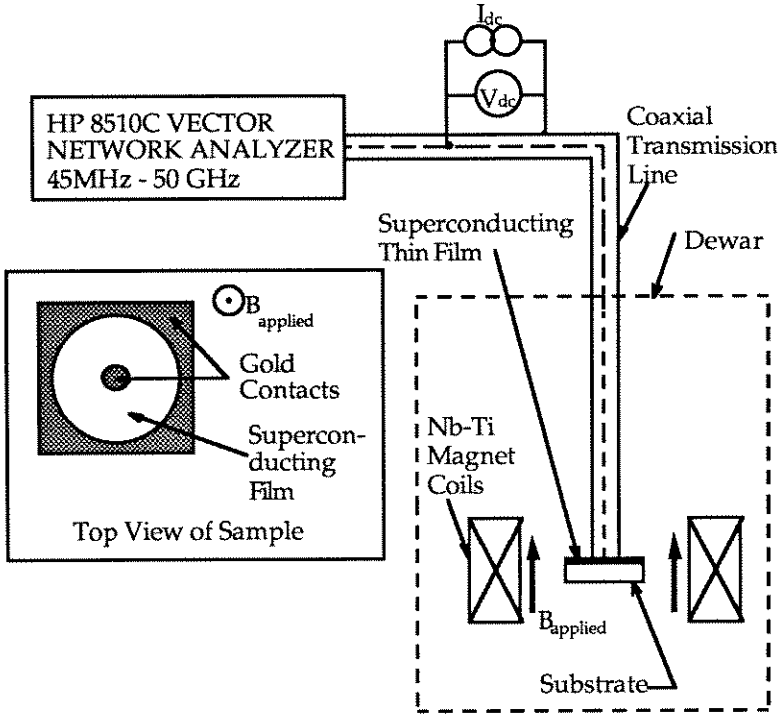


Fig. 2.3. Schematic diagram of experimental set-up for measurements in an external magnetic field.

In this experimental configuration room temperature calibrations are also performed at the location of the sample at the termination of the transmission line prior to each measurement. After calibrating, the transmission line must be disconnected

from the test set in order to load the sample, and the whole probe is inserted into a vacuum can. The vacuum can is pumped down to a pressure of ~ 50 μm Hg, and the whole assembly is inserted into the magnet or a helium storage dewar, before the transmission line can be reconnected to the network analyzer. As will be discussed in chapter 3, the process of disconnecting and reconnecting the transmission line to the test set after calibrations are performed necessarily leads to some degradation of the final calibration.

To perform the magnetic field measurements the vacuum can is immersed in a He vapor flow within the magnet. After the sample temperature drops to the desired range, the sample temperature is stabilized by controlling the temperature of the helium vapor with a heater on the magnet at the location of the helium vapor inlet, and also by means of a resistive heater on the probe itself. Measurements in finite magnetic field are generally made at constant temperature while the magnetic field is ramped from zero to a maximum value and then back to zero. Usually the data from every magnetic field point is saved as a frequency trace and as a magnetic field dependent file.

In addition to magnetic field dependent measurements, it is also possible to perform temperature dependent measurements with this experimental set-up. In this case the vacuum can is immersed in a helium storage dewar instead of the magnet system. Although the attenuation in this set-up is much larger than in the continuous-flow set-up, it has the advantage of smaller temperature gradients, and much smaller helium consumption.

## 2.3 Coaxial Cable/Thin Film Interface

A detailed diagram of the coaxial cable/film interface is shown in Fig. 2.4. Gold contacts a few thousand angstroms thick are evaporated through a washer-shaped shadow mask to form inner and outer electrical contacts on the film (see inset, Fig.

2.3). The portion of the film exposed between the contacts forms the Corbino disc proper, the inner and outer diameters of which are approximately 0.020 and 0.066 inch, respectively. Electrical contact is made to the inner and outer conductors of the coaxial cable through a modified microwave connector.[13] Direct contact is made between the outer conductor of the connector and the outer contact of the film, while contact is made between the inner contact of the film and the inner conductor of the cable by means of a small tapered pin inserted into the connector center conductor. The pin is tapered from a diameter of 0.020" down to 0.010", so that there is a restoring force in the direction of the film (the center conductor of the microwave connector is designed to spread open slightly in order to capture the center conductor of the mating connector), to ensure contact is maintained as the temperature is lowered. The size of this center conductor pin is crucial; if the diameter at the large end is much less that 0.020" the pin slides into the connector center conductor, and there is no restoring force. If the large end diameter is much greater than 0.020" the pin becomes a large perturbation within the connector, and can cause large resonant effects which make accurate frequency dependent measurements impossible. Contact is maintained as the

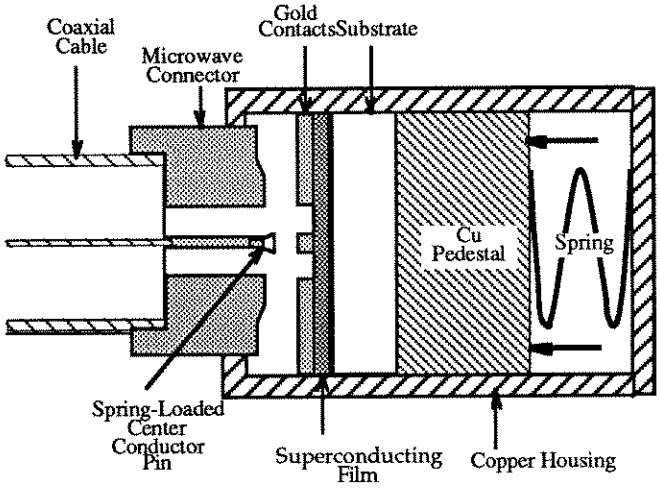


Fig. 2.4. Detailed view of thin film/connector interface, just prior to contact. Pressure is exerted on the aluminum pedestal by a spring in order to maintain contact between the film and connector throughout the temperature range.

temperature is changed by means of a copper pedestal and spring assembly which apply pressure to the backside of the substrate. Such a contact can reliably hold from room temperature to 4.2 K, with changes in the contact resistance of at most 15 mΩ over the entire temperature range.

In order to align the contacted film with the microwave connector properly, a special alignment jig is used to position the sample on the copper pedestal. Once the film is correctly positioned, the entire film/pedestal assembly[7] is loaded into a cylindrical copper housing, which also accepts the microwave connector, and ensures that the contacts on the film align with the connector as shown in Fig. 2.4.

## 2.4 Absolute Power Measurements

The fact that a modified microwave connector is used to contact the sample has a further advantage, because it allows for an HP437B power meter to be connected directly at the location of the sample in order to measure the actual microwave power incident on the thin film sample. This allows for the measurement the impedance of the film as a function of absolute power. This is in contrast to many resonant measurements which are in effect non-insertable devices, so that the actual power at the location of the sample can only be estimated. In addition, the power is usually set at the source, and compensation must be made for attenuation in the test set as well as the intervening transmission lines. In the present experiment, the actual microwave power reaching the sample is modified slightly by the changing attenuation of the coaxial cable as the temperature is lowered, but actual measurements suggest that changes in attenuation affect the signal by only a few percent (see section 3.3).

The minimum and maximum microwave power that can be used depends on a number of experimental factors. In general, the minimum power is a function of the

sensitivity of the microwave detectors internal to the HP8510C, with -30 dBm representing a readily achievable level at most frequencies without losing phase lock to the reference signal. At the lowest frequencies, however, one can lose the reference signal at power levels well above -30 dBm. When this occurs, one can simply employ internal attenuators built in to the network analyzer, which attenuate the output signal after the reference signal has separated out. Lower power levels are also more difficult to measure accurately with the power meter, and were not considered for this work.

The maximum microwave power available at the sample is limited by the maximum output power of the source, the maximum power that can be safely reflected back into the HP8510C test set (approximately +17 dBm), and the attenuation of the coaxial transmission line. As such, the maximum power incident at the sample is a strong function of frequency. Table 2.1 gives values for the power measured at the sample for a source power of +16 dBm for the two different experimental configurations described above.

Table 2.1. Maximum power levels available at the sample for various frequencies. The source output power is 16 dBm.

| Frequency | Maximum Power (dBm) Zero Field Experiment | Maximum Power (dBm) Finite Field Experiment |
|---|---|---|
| 45 MHz | 9.27 | 8.93 |
| 1GHz | 7.96 | 6.35 |
| 10GHz | 3.98 | -2.34 |
| 30GHz | -9.62 | -21.80 |
| 45GHz | -20.34 | -35.3 |

It is possible to perform a power-flattening calibration in order to make the power incident on the sample nearly the same for all frequencies. This is accomplished by connecting the power meter to the transmission line at the location of the sample, and initiating an automated power flatness calibration function available on the network

analyzer, with the power meter connected to the HP8510 system bus. The network analyzer then measures the power at each frequency in the measurement range and computes a correction factor that is stored in an internal register. After the flatness calibration is completed and power flatness is enabled, the power output from the source at each frequency point is adjusted so that the power at the sample is equal to the set source power at each frequency. It is important that the output power is set to a value small enough so that the source power does not become saturated, since this will lead to an unleveled power at the sample. Using the magnet set-up, power flatness can be enabled with the sample power set to -22 dBm, which delivers a frequency independent power at the sample from 45 MHz up to approximately 35 GHz, above which some roll-off does occur (see table 2.1). Setting the power to lower values results in the loss of phase lock to the reference signal at lower frequencies, as discussed previously.

In the Corbino disk geometry the rf currents flow in the radial direction, and the rf current density in the film is proportional to 1/r, where r is the distance from the center of the Corbino disk. The rf current density also depends on the film thickness and the rf power supplied by the source. If the sample is much thinner than the appropriate skin depth, the current density will be uniform in the film thickness. The (instantaneous) power transferred along the transmission line is given by the Poynting vector $\mathbf{P} = (\mathbf{E} \times \mathbf{H}^*)$ integrated over the cross section of the transmission line, which gives simply $P=I \cdot V$. Since the ratio of the voltage to the current is simply the characteristic impedance of the transmission line, $P=I^2Z_0$. The current density J is found by demanding that J(r) integrated over the volume of the Corbino disk be equal to the applied current I, which gives $J(r) = I/2\pi t_0 r$, where $t_0$ is the film thickness. The peak current density in the sample as a function of microwave power is therefore given by

$$J(r) = \frac{1}{2\pi t_0 r}\sqrt{\frac{P}{Z_0}} \qquad (2.1)$$

As an example, for a 1000 Å thick film and an applied rf power (at the sample) of zero dBm (=1 mW), and assuming the current density is uniform throughout the film thickness, the peak current density in the film is approximately $3x10^3$ amps/cm$^2$.

## 2.5 Sample Preparation

The superconducting thin films studied in this work are primarily several thousand angstroms of $YBa_2Cu_3O_{7-\delta}$ (YBCO) deposited on $LaAlO_3$ substrates (1/4" x 1/4" square, typically) by pulsed laser deposition.[14] Thin film samples were obtained from A. Findikoglu, C. Kwon, and M. Rajeswari within the Center for Superconductivity Research, and also from Alberto Pique at Neocera, Inc.

### 2.5.1 Thin Film Fabrication

In this section some of the relevant deposition information for samples used in this work is briefly summarized. Many more detailed accounts of pulsed laser deposition applied to the growth of high $T_c$ materials are widely available.[15,16] A substrate of $LaAlO_3$ is attached to a heater plate using silver paste, which has a high thermal conductivity. The substrate/heater assembly is loaded into a vacuum chamber, which is pumped down to approximately $2x10^{-5}$ Torr, at which point 300 mTorr of oxygen is admitted to the chamber and the substrate temperature is elevated gradually to above 700 °C. It is very important for sample homogeneity that the substrate temperature is uniform across the substrate throughout the deposition process. The laser pulses of wavelength 248 nm are focused on a rotating stoichiometric $YBa_2Cu_3O_7$ target at a rate of 10 Hz for a deposition rate of approximately 2-3Å/sec. The laser energy density is typically 1.7 J/cm$^2$. Immediately following deposition

approximately 400 Torr oxygen is admitted to the chamber, and the film is gradually cooled back to room temperature at variable rates. For the experiments described here it is desirable to have a $T_c$ in the range 89-91 K, but it is much more important to obtain a sample that is homogeneous over the area used for the measurement.

### 2.5.2 Metallic Contacts

In order to make concentric gold or silver contact pads as shown in Figs. 2.1 and 2.3, two different approaches were used: in-situ and ex-situ contact deposition. In the ex-situ technique a washer shaped shadow mask is used during evaporation of the contacts. The shadow mask is made from a magnetic material called COVAR which is an alloy of cobalt, nickel and iron, and is held in place by means of small magnets embedded in a specially designed substrate holder. The gold or silver is evaporated thermally or by electron beam evaporation, forming the inner and outer contact pads, and the masked part of the film becomes the Corbino disk. If the contact resistance between the gold or silver and YBCO is unsatisfactorily high ($\geq$ 25 m$\Omega$), as determined by a 3-point resistivity measurement when the film is superconducting (see section 2.6 below), the film is annealed in $O_2$ at 400-450 C for 1-8 hours. This normally results in a contact resistance of less than 15 m$\Omega$ (which gives a contact resistivity of approximately $3 \times 10^{-5}$ $\Omega cm^2$, assuming that the contact resistance is dominated by the smaller center contact). However, it is very important to ensure that no impurities are introduced during the contacting or annealing steps, since the subsequent annealing can destroy superconductivity in the film if some contamination has occurred.

The ex-situ technique described above was used for most of the samples studied in this work. However, an in-situ technique was also investigated. For the in-situ technique, a gold contact layer is deposited immediately following the film

deposition before the film is exposed to the atmosphere. After deposition a Corbino disk pattern is transferred to the gold/YBCO bilayer by standard photolithography techniques, and the gold is removed from the Corbino disk region using a gold etch (1g K/ 4g KI in 80 m$\ell$ deionized water). While the contact resistances were generally acceptable and no additional annealing was required, the samples subject to the in-situ process appeared to have been slightly damaged by the etching step. In order to be useful for the measurements described here, further optimization of the in-situ technique is required.

## 2.6 DC Resistivity Measurements

Measurements of the dc resistivity vs. temperature are made independently of the microwave measurements discussed above and serve several purposes. The temperature dependent resistivity measurements can be performed in about an hour, and are used to screen films so that only the best quality samples are used in the microwave measurements. Also, the dc measurements provide a sensitive measure of the contact resistance, which cannot be determined from the two-point resistance values obtained during the microwave measurements, and is difficult to determine directly from the microwave data. The dc measurements also serve as a check on the microwave surface impedance values, since in the thin film limit the real part of the effective impedance is just the real part of the resistivity, which is simply the dc resistivity for a thin normal metal. In addition, the dc resistivity measurements can be easily performed up to room temperature (which is difficult in the microwave setup), and can be instrumental in determining the temperature dependence of normal state properties for fluctuation conductivity analysis, for example.

The dc resistivity measurements are performed after the contacts are made, in a three point configuration, as illustrated in Fig. 2.5. Contact is made to the film by

means of beryllium-copper pins positioned on the film as shown in Fig. 2.5. The film itself is mounted on a copper block in which a silicon diode is embedded, and the whole assembly is immersed in a liquid helium storage dewar. The fourth contact is made to the beryllium copper pin on the center conductor, as close as possible to the film, because there is not sufficient room for two such pins to fit on the center contact pad. With this configuration, contact resistances down to 1 mΩ can be easily measured.

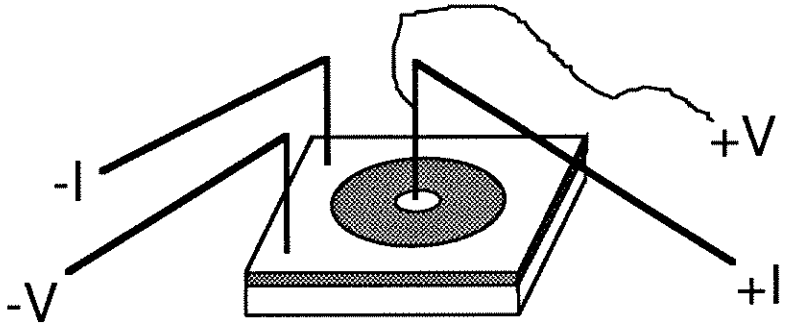


Fig. 2.5. Schematic diagram of contacts in 3 point resistivity vs. temperature measurement.

From measurements of the resistance in the above geometry, and knowing the inner and outer radii (a and b, respectively) of the Corbino disc, one can easily calculate the sheet resistance, $R_{square}$, from the measured resistance $R^{meas}$ according to

$$R^{meas} = R_{square} \cdot \frac{\ln(b/a)}{2\pi} \tag{2.2}$$

The sheet resistance is related to the resistivity simply by $R_{square} = \rho/t_0$, where $t_0$ is the film thickness. It is the sheet resistance which can then be compared to the effective impedance measured at microwave frequencies.

## Chapter 2 References


[1] H.K. Olsson, R.H. Koch, W. Eidelloth, and R.P. Robertazzi, Phys. Rev. Lett. **66**, 2661 (1991).

[2] N.-C. Yeh, D.S.Reed, W. Jiang, U. Kriplani, F. Holtzberg, A. Gupta, B.D. Hunt, R.P. Vasquez, M.C. Foote, and L. Bajuk, Phys. Rev. B **45**, 5654 (1992).

[3] H. Wu, N.P. Ong, and Y.Q. Li, Phys. Rev. Lett. **71**, 2642 (1993).

[4] S. Ramo, J.R. Whinnery, and T. Van Duzer, "Fields and Waves in Communication Electronics", Second Edition, John Wiley and Sons, New York (1984), p.225.

[5] O.M. Corbino, Nuovo Cimento **1** (1911); R.P. Heubner, "Magnetic Flux Structures in Superconductors" (Springer, Berlin, 1979), p.128.

[6] M.P. Shaw and P.R. Solomon, Phys. Rev. **164**, 535 (1967).

[7] N. Bluzer, D.K. Fork, T.H. Geballe, M.R. Beasley, M.Y. Reizer, S.R. Greenfield, J.J. Stankus, and M. Fayer, IEEE Trans. Magn. 27, 1519 (1991); N. Bluzer, J. Appl. Phys. **71**, 1336 (1992).

[8] Yan-Zhen Wei and S. Sridhar, Rev. Sci. Instrum. **60**, 3041 (1989).

[9] L. L. Li, N. H. Ismail, L. S. Taylor, and C. C. Davis, IEEE Trans. Biomed. Eng. **39**, 49 (1992).

[10] Nour-Eddine Belhadj-Tahar, A. Fourrier-Lamar, and H. DeChanterac, IEEE Trans. Microwave Theory Tech. **38**, 1 (1990).

[11] M. A. Saed, S. M. Riad, and W. A. Davis, IEEE Trans. Microwave Theory Tech. **39**, 485 (1990).

[12] This coaxial cable is manufactured by Rogers Corporation.

[13] The microwave connector used is a V101-F connector, made by Wiltron Corp.

[14] D.T. Dijikkamp, T. Venkatesan, X.D. Wu, S.A. Shaheen, N. Jisrawi, Y.H.

Min-Lee, W.L. McLean, and M. Croft, Appl. Phys. Lett. **51**, 619 (1987).

[15] C. Kwon, Ph. D. Thesis, University of Maryland, 1995.

[16] "Pulsed Laser Deposition of Thin Films", K. Hubler and D.B. Chrisey, Eds., John Wiley and Sons, New York (1994).

# Chapter 3
# Measurement Calibration and Error Correction

This chapter develops the data analysis tools necessary to correctly interpret the measured frequency dependent data on superconducting thin films. In section 3.1 the complex resistivity $\rho(\omega) = \rho_1(\omega) + i\rho_2(\omega)$ of thin films is extracted from the measured complex reflection coefficient $S_{11}(\omega)$. Section 3.2 then discusses in some detail the calibration procedures necessary for the accurate frequency measurement of the complex reflection coefficient over the broad frequency range from 45 MHz - 50 GHz, and the errors associated with such a calibration procedure. Sections 3.3 and 3.4 discuss errors that affect the frequency dependent measurements that are not addressed by standard calibration procedures, such as changes in the temperature of the transmission line (section 3.3), and transmission of the incident signal through the thin film under study and into the substrate (section 3.4). Finally in section 3.5 the full error correction procedure developed in this chapter for accurate frequency dependent measurements at cryogenic temperatures is summarized for the two different experimental configurations used in this work.

## 3.1 Relation of the Reflection Coefficient to the Complex Resistivity

In order to interpret our experimental data on conductors, it is necessary to extract the surface impedance $Z_s$ from our measurements of the reflection coefficient. The reflection coefficient $S_{11}$ is related to the load impedance $Z_L$ of the sample by the simple formula

$$S_{11} = \frac{Z_L - Z_0}{Z_L + Z_0} \tag{3.1}$$

where $Z_0$ is the characteristic impedance of the coaxial transmission line (assumed to be $50\Omega$ and real). The reflection coefficient is therefore a complex, dimensionless

quantity which measures the impedance mismatch between the transmission line and the load, and is bounded in magnitude between 0 and 1.

The load impedance $Z_L$ in Eq. 3.1 is the ratio of the total voltage across the Corbino disc to the total current flowing through the disc. This quantity depends on the dimensions of the Corbino disc, and assuming the presence of only the TEM mode, can be expressed in terms of the surface impedance $Z_s$ of the film as

$$Z_L = \Gamma Z_s \tag{3.2}$$

The scale factor $\Gamma$ in this expression simply relates the "ohmic" impedance $Z_{IV} = V/I$, and the field impedance $Z_{field} = E_r/H_\phi$ for the TEM mode in a coaxial system (here V and I represent the instantaneous voltage and current, respectively, across the coaxial cable, while $E_r$ and $H_\phi$ represent the instantaneous electric and magnetic fields, respectively, within the coaxial cable). The surface impedance $Z_s$ of the film is simply the field impedance $Z_{field}$ evaluated at the surface of the film.

To calculate $\Gamma$, assume that one has an ideal, lossless coaxial transmission line of inner radius a and outer radius b. For a given (instantaneous) current I flowing through the transmission line, the (instantaneous) magnetic field at a distance r from the transmission line axis is given by $H_\phi = I/2\pi r$ Amps/meter. Similarly, the (instantaneous) electric field generated by an (instantaneous) potential difference V between the inner and outer conductors is given by $E_r = V/[\ln(b/a)r]$ volts/meter. The ratio V/I in terms of $E_r$ and $H_\phi$ is given by $V/I = [\ln(b/a)/2\pi]\ (E_r/H_\phi)$. This gives the relationship between the field impedance $Z_{field}$ and the "ohmic" impedance $Z_{IV}$ for the TEM mode in the coaxial system, and yields $\Gamma = \ln(b/a)/2\pi$.

Once the reflection coefficient $S_{11}$ of the sample has been measured, one can obtain the surface impedance simply from Eqs. 3.1 and 3.2. If the load impedance $Z_L$ of the sample is small compared to $Z_0$ (which is normally the case for conductors), then evaluation of the geometric factor $\Gamma$ (with $2a=5.08 \times 10^{-4}$ meters and $2b=1.68$ x

$10^{-3}$ meters) yields the following approximate relationship between changes in the reflection coefficient and changes in the surface impedance:

$$\delta|Z_s| \approx (131.6\Omega) \cdot \delta|S_{11}| \tag{3.3}$$

Our measurement resolution for changes in $|S_{11}|$ at 1 GHz is approximately $5x10^{-4}$, implying a resolution for changes in the surface impedance of approximately 75 mΩ at this frequency.

For comparison, the surface impedance of a bulk metallic sample in the local limit is given by

$$Z_s^{\infty} = \sqrt{\frac{i\mu_0\omega}{\sigma}} \tag{3.4}$$

where $\sigma = 1/\tilde{\rho}$ is the conductivity of the material, which is in general complex ($\sigma = \sigma_1 - i\sigma_2$). For a numerical example, consider the superconductor $YBa_2Cu_3O_{7-\delta}$ (YBCO), which in the normal state just above $T_c$ has a resistivity $\rho_n \sim 100$ μΩ-cm. With a conductivity that is completely real, evaluation of Eq. 3.4 at a frequency of 1 GHz gives $Z_s \approx (1+i)$ 62.8 mΩ, which is comparable in magnitude to the sensitivity limit of our measurement calculated above. This example illustrates the limited sensitivity of the measurement system for bulk metallic samples, and means that the effective surface impedance of our samples must be somehow enhanced, particularly in the superconducting state, for our technique to be useful. This is accomplished in practice by working with thin samples, where the measured surface impedance is increased due to finite film thickness effects.[1,2,3] The use of thin films, combined with large external magnetic fields and temperatures near $T_c$, provides more than adequate enhancement of the effective surface impedance for meaningful measurements with this technique.

The effective surface impedance which one measures for a film of thickness $t_0$

is given by

$$Z_s^{eff} = Z_s^{\infty} \coth( kt_0 ) \tag{3.5}$$

where $Z_s^{\infty}$ is the surface impedance of a bulk sample [Eq. 3.4], and $k = (i\mu_0\omega\sigma)^{1/2}$ is the complex propagation constant in the film. [When the film is in the normal state, $k=(1+i)/\delta$, where $\delta$ is the normal metal skin depth; at temperatures much below $T_c$ the propagation constant reduces to $k\sim 1/\lambda$, where $\lambda$ is the superconductor magnetic penetration depth.] The expression in Eq. 3.5 implicitly assumes that the fields are zero at the backside of the film. Note also that Eq. 3.5 reduces to the bulk expression when the film thickness $t_0 >> 1/|k|$.

Equation 3.5 can often be further simplified when applied to thin metallic or superconducting samples. If the argument of the hyperbolic cotangent function is small (true when the film thickness $t_0 << \delta,\lambda$) we may approximate coth(x) by 1/x, and obtain the following remarkably simple expression for the effective surface impedance of a thin film, valid as long as $|k|t_0 << 1$:

$$Z_s^{eff} \approx \frac{\tilde{\rho}}{t_0} \qquad (\text{for } |k|\, t_0 << 1) \tag{3.6}$$

Using the normal state resistivity for YBCO given above, and a film thickness of $t_0$=1000 Å, Eq. (6) yields $Z_s^{eff} \approx 10\Omega$ in the normal state, just above $T_c$. Thus the effective surface resistance of a thin film is considerably enhanced relative to its infinite thickness value. In the superconducting state, when $T << T_c$, the effective surface impedance is dominated by the kinetic inductance of the film: $Z_s^{eff} \sim i\mu_0\omega\lambda^2(T)/t_0$, which is enhanced by a factor $\lambda(T)/t_0$ compared to the bulk value in the same limit.

Note that as a result of Eqs. 3.2 and 3.6 the measured quantity $Z_L^{eff}$ is directly related to the complex bulk resistivity $\tilde{\rho}$ of a thin film sample, which is a fundamentally interesting quantity. For instance, many theories of vortex dynamics give explicit

expressions for $\tilde{\rho}$ (B,T,ω), making comparisons between our experimental data and theory straightforward. Also, having obtained the complex resistivity, it is elementary to obtain the complex conductivity, which is also fundamentally interesting. We believe that one of the main utilities of our technique is the fact that we can directly measure the bulk complex resistivity or conductivity of a metallic or superconducting thin film sample. Yet another consequence of Eq. 3.6 is that in the normal state, where $\tilde{\rho}$ is completely real, we expect imaginary$\{Z_s^{eff}\} \rightarrow 0$, in contrast to the bulk case, where imaginary$\{Z_s^{\infty}\}$ = real$\{Z_s^{\infty}\}$ in the normal state.

## 3.2 Standard Calibration Methods

### 3.2.1 The Need for Calibration

The expression for the reflection coefficient given by Eq. 3.1 is valid only if the measurement is performed directly at the location of the impedance discontinuity. In practice the experimentally measured reflection coefficient will include effects due to the intervening transmission line, connectors, etc. which are necessary to perform a practical measurement. These effects become particularly important at higher frequencies, where the wavelength of the measurement signal is much smaller than the dimensions of the system. In what follows we will discuss in some detail the calibration procedures used to minimize the systematic errors involved in the measurement of the reflection coefficient versus frequency.

The measurement of the reflection coefficient $S_{11}^{actual}$ is in practice corrupted by attenuation and multiple reflections in the coaxial cable system, as well as by errors in the detection apparatus. These effects can be accounted for and eliminated from the data by means of a set of calibrations applied to the measured reflection coefficient $S_{11}^{meas}$. A general expression for the the measured reflection coefficient ($S_{11}^{meas}$) in terms of the actual reflection coefficient ( $S_{11}^{actual}$) can be obtained using microwave

network theory[4] and is given by

$$S_{11}^{meas} = E_D + \frac{E_R S_{11}^{actual}}{1 - E_S S_{11}^{actual}} \tag{3.7}$$

Here $E_D$, $E_R$, and $E_S$ are complex error coefficients that completely characterize the detection apparatus/ transmission line system.

### 3.2.2 Measured Error Coefficients

The error coefficient $E_D$ in Eq. 3.7 is the directivity, which arises from the imperfect nature of the directional couplers in the test set of the network analyzer, and from reflections due to connectors in the system. These effects result in a small "leakage" of the signal from the source directly into the detectors, by-passing the load entirely. The effect of this error is easily seen by considering a reflectionless load ($S_{11}^{actual} = 0$) in Eq. 3.7, which shows that the measured reflection coefficient is entirely due to the "leakage" signal in this limit. The magnitude of $E_D$ versus frequency is shown in Fig. 3.1 for a typical calibration in the zero-field experimental configuration (see Fig. 2.2). The value of $E_D$ has no systematic dependence on

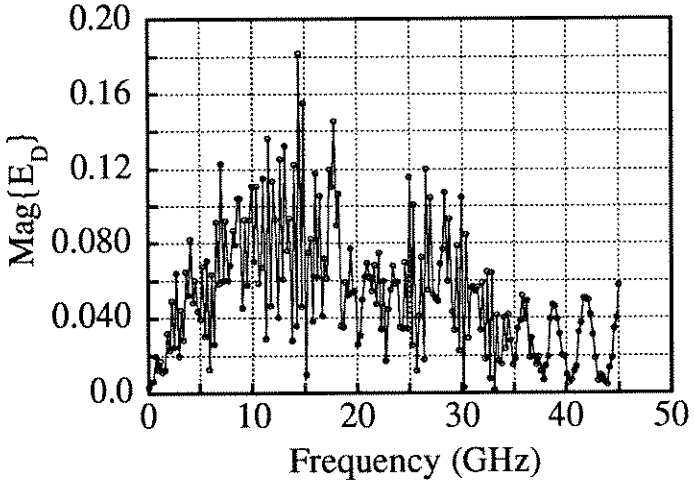


Fig. 3.1. Magnitude of the directivity error term $E_D$ vs. frequency for the zero-field measurement.

frequency as shown in Fig. 3.1, and the magnitude is bounded by approximately 0.15 for the systems used here.

The error term $E_R$ in Eq. 3.7 is called the reflection tracking, and corrects principally for the attenuation and phase delay introduced by the transmission line. For a system consisting of simply a load at the end of a transmission line of length $\ell$, and for which $E_D$ and $E_S$ are zero, one would obtain $S_{11}^{meas} = e^{-2\gamma\ell} S_{11}^{actual}$, where $\gamma$ is the complex propagation constant of the transmission line ($\gamma=\alpha+i\beta$, where $\alpha$ is the attenuation constant of the transmission line, and $\beta$ is the phase constant). Comparison with Eq. 3.7 shows that the error coefficient $E_R$ would be given by $E_R = e^{-2\gamma\ell}$ for this simple case. In practice one finds that the frequency dependence of $E_R$ strongly resembles $e^{-2\gamma\ell}$, with $\alpha$ increasing roughly as $\omega^{1/2}$, and $\beta=\omega/v_{phase}$, where $v_{phase}$ is the phase velocity in the transmission line. The magnitude of $E_R$, shown in Fig. 3.2, is close to 1 at low frequencies (indicating little attenuation), and decreases to approximately 0.2 at the high frequency limit of 45 GHz (which implies much stronger attenuation). The fact that $|E_R|$ is greater than 1 at low frequencies in Fig. 3.2 indicates that there are contributions to $E_R$ from other sources than the simple description given above.

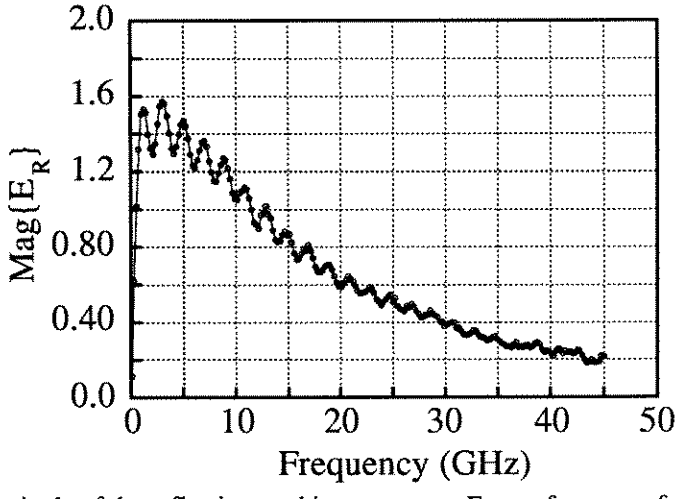


Fig. 3.2. Magnitude of the reflection tracking error term $E_R$ vs. frequency for the zero-field measurement.

The third error term $E_S$ in Eq. 3.7 is referred to as the source match, which arises due to the re-reflection of a portion of the signal at the measurement port, caused by the slight impedance mismatch between the detectors and the transmission line. This re-reflected signal interferes with the incident signal at the load, adding a small error to the incident signal. Since the reflection coefficient is defined as the ratio of the reflected signal to the incident signal, this error will also affect the reflection coefficient. Like $E_D$, the source match error coefficient shows no systematic dependence on frequency, and is also bounded in magnitude by approximately 0.15, as can be seen from the frequency dependence of $|E_S|$ shown in Fig. 3.3.

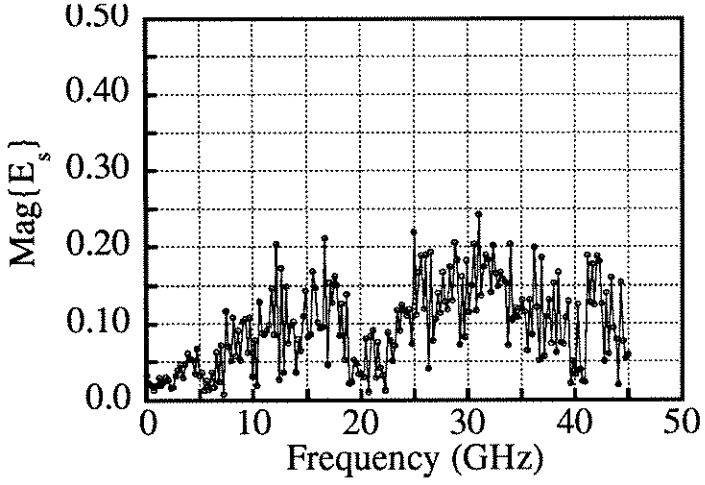


Fig. 3.3. Magnitude of the source match error term $E_S$ vs. frequency for the zero-field measurement.

### 3.2.3 Calibration Procedures

The three error coefficients described above are all frequency dependent. It is possible to ascertain values for all three error coefficients at each frequency point of interest through a calibration procedure involving the measurement of three standards for which $S_{11}^{actual}$ is known. As pointed out previously, by measuring a standard for which $S_{11}^{actual} = 0$, one can directly measure the error coefficient $E_D$. In practice one uses a standard short ($S_{11}^{actual} = -1$), a standard open ($S_{11}^{actual} = +1$) and a matched

load ($S_{11}^{actual} = 0$) to fully calibrate the system, although one can in principle use as a standard any load for which $S_{11}^{actual}$ vs. frequency is known. For measurements above 4 GHz, a sliding load must be used, because it is difficult to realize a matched load over such a broad frequency range.

Once values for all three error coefficients are obtained (at each frequency point of interest), Eq. 3.7 may be inverted to calculate $S_{11}^{actual}$ given $S_{11}^{meas}$ and $E_D$, $E_R$, and $E_S$. This calibration procedure involving the measurement of 3 known standards is performed at room temperature prior to every measurement. Since our measurement makes use of a modified microwave connector to contact the sample, the calibrations are performed using this same connector, directly at the location of the sample. With an accurate calibration, the inversion of Eq. 3.7 should yield the actual reflection coefficient of the load described by Eq. 3.1.

When such a procedure is followed, one obtains the reflection coefficient vs. frequency, which is shown for a thick silver film ($t > \delta$) on a $LaAlO_3$ substrate in Fig. 3.4 (magnitude $S_{11}$) and Fig. 3.5 (phase $S_{11}$). From the discussion in section 3.1, one expects the reflection coefficient to be $S_{11} \cong -1 + 0i$ for a metallic film of thickness $t >> \delta$ (where $\delta$ is the skin depth) to within the resolution limit of the measurement system. The fact that the reflection coefficient in Figs. 3.4 and 3.5 deviates from this expected behavior simply means that there are some residual systematic errors that the calibration procedure described above does not remove. This could be due to the fact that during the measurements on film samples, a tapered pin is used to make contact between the center conductor of the V101F connector and the film (see section 2.3), whereas the standards used for calibration all utilize a conventional 2.4 mm male connector to couple to the modified V101F connector that terminates the transmission line. The response shown in Figs. 3.4 and 3.5 is in general seen for a number of different bulk metallic samples. Note, however, that the reflection coefficient

magnitude is within 5% of its expected value over the entire 3 decades of frequency. Because the actual frequency dependence of the bulk metallic sample is known (it may be calculated simply from Eqs. 3.1, 3.2, and 3.4), it may be used as an additional calibration standard to improve the accuracy of the measurement.

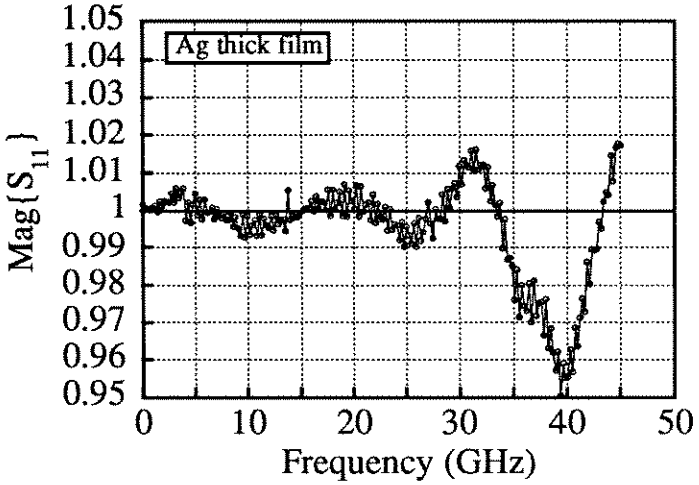


Fig. 3.4. Magnitude of the reflection coefficient $S_{11}$ of a thick silver film at room temperature.

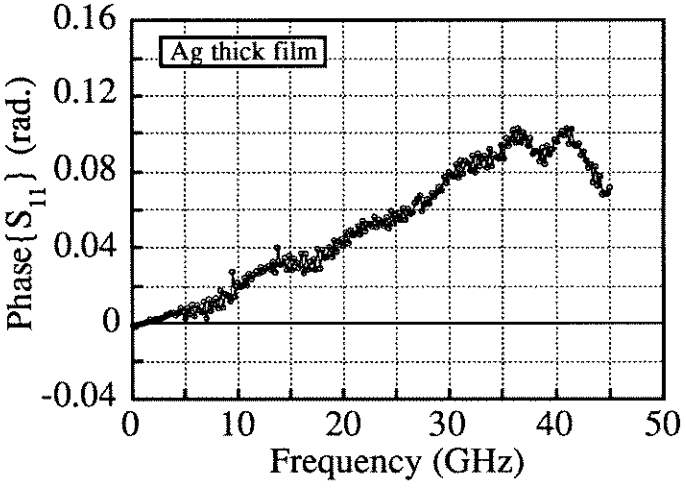


Fig. 3.5. Phase of the reflection coefficient $S_{11}$ of a thick silver film at room temperature.

### 3.2.4 Calibration Errors

The calibration procedure described above is strictly valid only as long as the

physical and electrical properties of the coaxial transmission line and test set are reproducible: the same during the measurement as during the calibration procedure. To maximize the accuracy of the calibration, semi-rigid coaxial cables are used to reduce physical changes in the transmission line system. In addition, in the zero-field set-up the calibrations and measurements can be performed without disconnecting the transmission line from the test set. This is important since reproducibility at connections is difficult to maintain through repeated connections/disconnections. In the magnetic field measurements, however, the transmission line must be disconnected in order to fit the probe into the magnet dewar.

In spite of the above considerations, errors do exist in the measurement system and in the calibration procedure. In what follows the errors that affect the calibrations will be discussed, in order to estimate the effect of such errors on the final measurements.

The inverse of Eq. 3.7 gives an expression for $S_{11}^{actual}$ in terms of $S_{11}^{meas}$ and the three error coefficients described in section 3.2 above. Labeling this expression for $S_{11}^{actual}$ as the corrected reflection coefficient $S_{11}^{correct}$ gives

$$S_{11}^{correct} = \frac{\left(S_{11}^{meas} - E_D\right)}{E_R + E_S\left(S_{11}^{meas} - E_D\right)} \tag{3.8}$$

Any error in the experimentally determined reflection coefficient, $\Delta S_{11}^{correct}$, is therefore a result of errors in the four experimentally measured quantities: $\Delta S_{11}^{meas}$, $\Delta E_D$, $\Delta E_R$, and $\Delta E_S$. One obvious disadvantage of the need to perform the calibration described above is the propagation of errors. Instead of just one (complex) measured quantity, we now have four, each with its own associated uncertainty.

The measurement errors that occur in $S_{11}^{correct}$ may be classified as either random or systematic. The random errors in $S_{11}^{correct}$ are due solely to the random

errors in the measured reflection coefficient $S_{11}^{meas}$. These errors may be estimated from the standard deviation obtained by performing a series of measurements on the system in the same state. The resulting upper bound for $\Delta S_{11}^{meas}$ is

$$\Delta \left| S_{11}^{meas} \right| \approx 2 \times 10^{-4} \tag{3.9}$$

It is assumed that there is no overall frequency dependence for the random errors $\Delta S_{11}^{meas}$ over the entire accessible frequency range (45 MHz-50 GHz). However, this is not true for the corresponding random errors in $\Delta S_{11}^{correct}$, since the errors in $S_{11}^{meas}$ must be propagated through Eq. 3.8 to obtain the errors in $S_{11}^{correct}$. Such an analysis shows that at low frequencies ( $\leq$ 2 GHz), the random errors in $S_{11}^{correct}$ are on the order of $5 \times 10^{-4}$, while at the highest measurable frequencies (50 GHz), the random errors in $S_{11}^{correct}$ approach approximately $2 \times 10^{-3}$. The fact that the measurement is more accurate at lower frequencies is due in part to the increased attenuation of the measurement signal by the transmission line at higher frequencies. These values for $\Delta S_{11}^{correct}$ determine the (frequency dependent) resolution of the measurement system, the smallest change in $S_{11}^{correct}$ that can be observed which is statistically significant. This is also the theoretical limit of the accuracy of the system, in the absence of any systematic errors.

In practice, the accuracy of the measurement system is limited by systematic errors generated by inaccuracies in the measured values of the error coefficients $E_D$, $E_R$, and $E_S$. These errors are in general much harder to quantify than the random errors discussed above. Since $E_D$, $E_R$, and $E_S$ are measured in the same way as $S_{11}^{meas}$, the uncertainty in their values is at least as large as $\Delta S_{11}^{meas}$. In addition, since the calibration is performed at room temperature, and the measurements on superconductors are made at much lower temperatures, changes in the attenuation and phase velocity of the transmission line also contribute to errors in the values of the

error coefficients. In order to reduce the effects of these systematic errors as much as possible, we exploit the fact that we know what the reflection coefficient of a superconductor should look like at low temperatures. This enables us to replace one of the three standards used for calibration by this "reference state" of the sample, and effectively recalibrate the system at low temperatures. This procedure will be discussed in detail in section 3.3 below.

## 3.3 Temperature Dependent Effects

### 3.3.1 Origin of Temperature Dependent Effects

A necessary requirement for the measurement system described here is the ability to vary the sample temperature. Since direct contact is made between the coaxial transmission line and the sample, the temperature of at least a portion of the transmission line necessarily changes during the measurement. Since the electrical properties of the transmission line depend on temperature, varying the sample temperature affects the accuracy of the room-temperature calibrations.

The electrical properties of the transmission line that are affected by changes in temperature are the attenuation constant $\alpha$ and the phase constant $\beta$. The attenuation constant $\alpha$ depends on the surface resistance $R_s$ of the inner and outer conductors of the coaxial cable:[5]

$$\alpha = \frac{R_s}{4\pi Z_0}\left(\frac{1}{b} + \frac{1}{a}\right) \tag{3.10}$$

where a and b are the inner and outer radii respectively of the coaxial transmission line, and $Z_0$ is the characteristic impedance of the line. The phase constant $\beta$ depends primarily on the dielectric constant of the material used to separate the inner and outer conductors in the coaxial cable, which in this case is air-articulated Teflon (PTFE):[5]

$$\beta = \omega\sqrt{\mu\varepsilon'} \tag{3.11}$$

where $\varepsilon'$ is the real part of the dielectric constant. It is therefore changes in the surface resistance of the copper conductors and changes in the dielectric constant of the Teflon which lead to changes in the electrical properties of the coaxial transmission line as the temperature is changed.

Figures 3.6 and 3.7 show the changes in the magnitude and phase, respectively, of the reflection coefficient $S_{11}$ of the silver thick film standard as the temperature is lowered from 290 K to 70 K in the zero field experimental configuration. In both figures the change in $S_{11}$ is defined as $\Delta S_{11} = S_{11}(72K) - S_{11}(290K)$. The change in the phase is roughly linear in frequency (as might be expected from Eq. 3.11), while the change in the (log) magnitude of $S_{11}$ is much smaller, and resembles $\omega^{1/2}$, which comes from the $\omega^{1/2}$ dependence of the surface resistance $R_s$ on frequency.

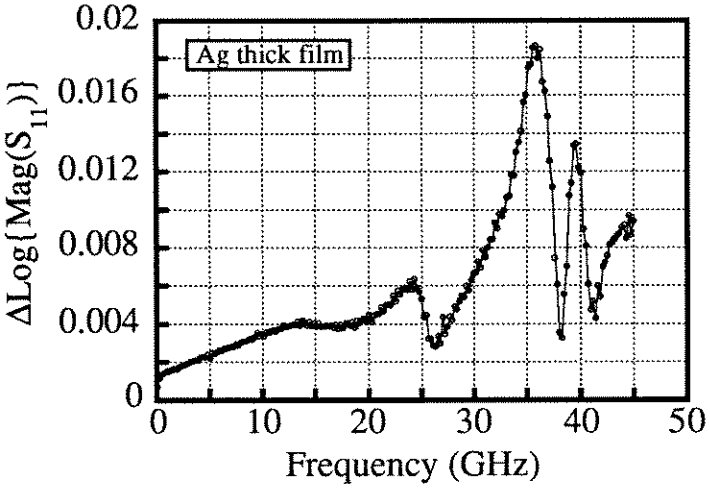


Figure 3.6. Change in the Log Magnitude of the reflection coefficient for the silver thick film between 290 K and 72 K in the zero field configuration.

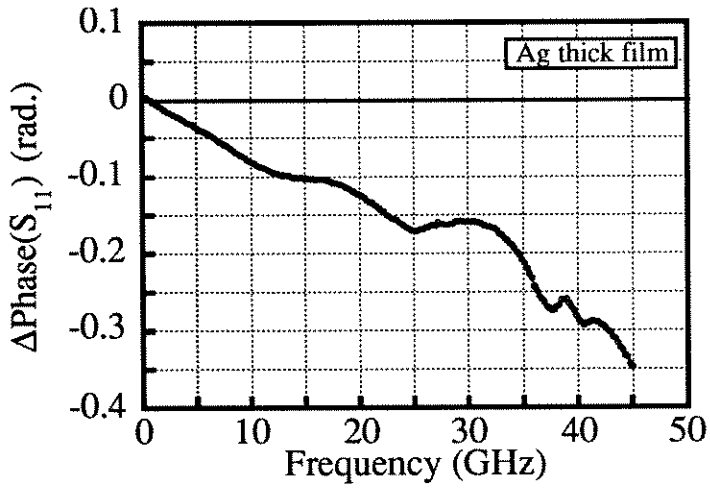


Figure 3.7. Change in the Phase of the reflection coefficient for the silver thick film between 290 K and 72 K in the zero field configuration.

In order to remove effects due to temperature changes in the coaxial line, two things are done. The measured reflection coefficient vs. temperature at a low temperature (typically ~ 70 K for the YBCO measurements) is used as a reference state, so that the data is in effect measured relative to this state, in order to correct for most of the effects due to the change in temperature of the transmission line. Also, the small changes with temperature that occur during the measurement are accounted for by measuring the change in the response of a thick silver film over the same temperature interval. This background contribution is then subtracted from the actual data.

### 3.3.2 Low Temperature Recalculation of $E_R$

In order to correct our experimental data for these temperature-dependent changes in the electrical properties of the transmission line, we can use a low-temperature measurement as an additional calibration standard. In order to achieve maximum accuracy in the additional calibration step, we use the measured response of the superconducting film itself at a sufficiently low temperature so that its response is nearly that of a perfect reflector. Figure 3.8 shows the magnitude of $S_{11}$ for a 1000 Å

thick YBCO film at 72 K in addition to $|S_{11}|$ for the silver thick film standard, also at 72K. This figure shows that the response of the superconducting film at 70 K is nearly identical to that of a thick normal conductor, and therefore should be appropriate to use as a calibration standard. For maximum accuracy, we assume that the response of the superconductor at this temperature is described by a two-fluid model, with the real and imaginary parts of the conductivity given at temperature $t=T/T_c$ by $\sigma_1 = t^4/\rho_n(T)$, and $\sigma_2 = (1-t^4)/\mu_0\omega\lambda_0^2$ and proceed to calculate the expected response (using Eqs. 3.4, 3.2, and 3.1), assuming reasonable values for $\lambda_0$ and $\rho_n(T)$. We use the calculated response ($S_{11}^{actual}$), the measured response ($S_{11}^{meas}$), and the measured values for the error coefficients $E_D$ and $E_S$ in Eq. 3.7 to recalculate the error coefficient $E_R$. We therefore make the explicit assumption that only the reflection tracking coefficient $E_R$ changes as the temperature is changed. In this manner we can correct for any residual systematic errors in the error term $E_R$.

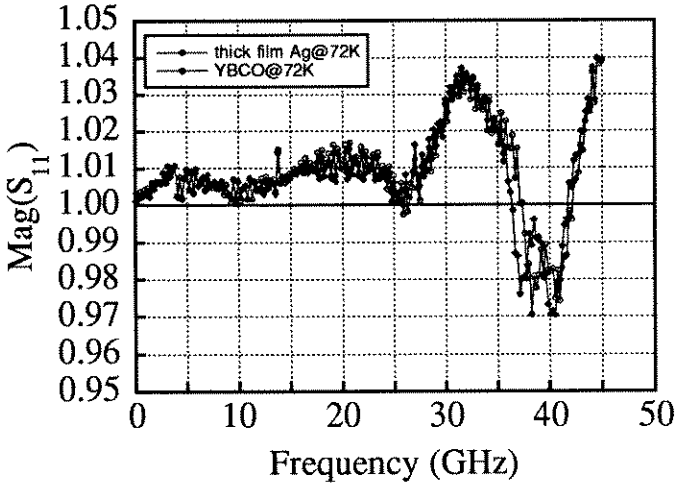


Fig. 3.8. Magnitude of the reflection coefficient of a superconducting YBCO film and Ag thick film at 72 K (both films on $LaAlO_3$ substrates).

### 3.3.3 Determination of the Background Contribution

A further correction step is necessary, however, to correct for the small changes in the cables that occur **during** the temperature ramp measurement. These errors are

deduced by measuring the response of the thick silver film (also on a $LaAlO_3$ substrate) over the same temperature interval as for the superconductor. These background changes in the frequency dependence as a result of temperature-dependent errors are subtracted off before the new error coefficients described above are applied. For example, if the frequency dependence is measured for a superconductor at 90 K, and the low-temperature reference state referred to above is 70 K, the background contribution is determined by measuring the difference in the frequency dependence of the silver thick film standard between 90 K and 70 K, and directly subtracting off this quantity from the frequency dependence of the superconductor measured at 90 K. Since these temperature dependent changes are primarily due to the changing propagation constant of the coaxial transmission line, the difference referred to above is calculated by taking the difference in the log magnitude and phase of the reflection coefficient.

## 3.4 Substrate Effects

### 3.4.1 Origin of Substrate Effects

Because we make use of thin samples in order to enhance our measured value of $Z_s^{eff}$, we expect to encounter errors due to the transmission of radiation through the film and into the substrate if the thickness of the film under study is made sufficiently small. In order to estimate the influence of such effects on our measurements, it is necessary to calculate the applicable corrections to Eq. 3.5 that result from allowing a non-zero value for the electric and magnetic fields within the substrate. A simple analysis involving only TEM waves yields the following expression for the effective surface impedance of a film of thickness $t_0$ backed by a substrate that has a field impedance $Z_s^{sub}$:

$$Z_s^{eff} = \frac{Z_s^{\infty}\coth(kt_0) + \frac{(Z_s^{\infty})^2}{Z_s^{sub}}}{\left(1 + \frac{Z_s^{\infty}\coth(kt_0)}{Z_s^{sub}}\right)} \tag{3.12}$$

Here again $Z_s^{\infty}$ is the surface impedance of a bulk sample, and k is the complex propagation constant, as in Eq. 3.5. One can think of $Z_s^{sub}$ as an effective substrate impedance that includes the effect of everything that lies behind the film, which for our geometry would include the copper pedestal. Note that the expression for $Z_s^{eff}$ in Eq. 3.12 reduces to Eq. 3.5 when $Z_s^{sub} \to \infty$. Unlike Eq. 3.5, however, this expression gives $Z_s^{eff} = Z_s^{sub}$ as $t_0 \to 0$. Under conditions where $|k|t_0 << 1$ [the same assumptions that led to Eq. 3.6] this expression simplifies to

$$Z_s^{eff} \approx \frac{\tilde{\rho}/t_0}{1 + \frac{\tilde{\rho}/t_0}{Z_s^{sub}}} \qquad (|k|t_0 << 1) \tag{3.13}$$

This expression clearly shows the conditions under which the influence of the substrate is important: when the effective impedance of the film is comparable to the impedance of the substrate. As will be shown in chapter 4, the actual substrate impedance depends on frequency approximately as $|Z_s^{sub}| \sim 1/\omega$, so the effect of the substrate on $Z_s^{eff}$ is more significant at higher frequencies. Also, the corrections to $Z_s^{eff}$ due to the substrate are most significant when the film is in the normal state, where $\rho/t_0$ is large. Note that Eq. 3.13 also implies that when the film is fully superconducting, the corrections due to the substrate are essentially negligible, even for a very thin film, as long as $|\rho|/t_0 << |Z_s^{sub}|$.

### 3.4.2 Experimental Determination of $Z_s^{sub}(\omega)$

In order to correct for the contribution of the substrate, it is necessary to extract

a measure of $Z_s^{sub}(\omega)$, so that Eq. 3.13 may be inverted to obtain $\rho/t_0$ as a function of frequency. This is accomplished by converting to an effective impedance $[Z_s^{eff}(\omega)]$ the reflection coefficient data obtained at an arbitrary temperature when the superconductor is in the normal state. This data will in general show some frequency dependence in both the real and imaginary parts, as Figs. 3.9 and 3.10 illustrate for a typical case, which is primarily due to the substrate contribution. The effective substrate impedance $Z_s^{sub}(\omega)$ is extracted by demanding that $\rho(\omega)/t_0$ in the normal state be constant as a function of frequency and equal to the measured dc value of R/square = $\rho_{dc}/t_0$. This is shown as a solid line in Figs. 3.9 and 3.10. With values of $Z_s^{eff}(\omega)$ and $\rho(\omega)/t_0$ so determined, Eq. 3.13 may be solved for $Z_s^{sub}(\omega)$. The results for $|Z_s^{sub}(\omega)|$, extracted from the data in Figs. 3.9 and 3.10, is shown in Fig. 3.11. The results of a first-principles calculation for the functional form of $|Z_s^{sub}(\omega)|$ will be shown for comparison in section 4.6. With the explicit assumption that $Z_s^{sub}(\omega)$ is temperature independent over the measurement interval, this value of $Z_s^{sub}(\omega)$ can be applied to the frequency dependence measured at other temperatures in order to obtain $\rho(\omega)/t_0$ at any desired temperature.

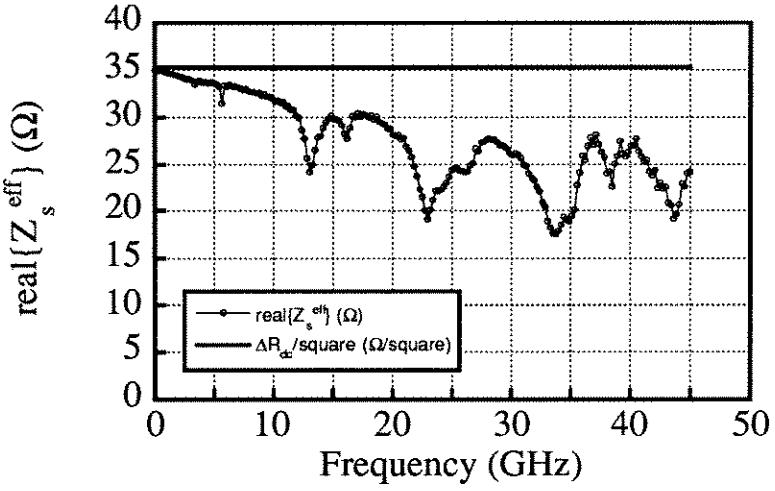


Fig. 3.9. Real part of the effective surface impedance $Z_s^{eff}$ for a YBCO film at 125 K. Also shown is the dc sheet resistance at the same temperature.

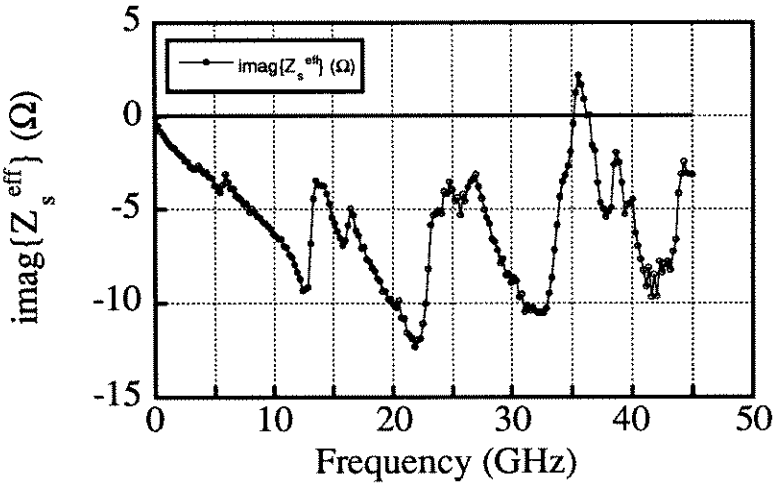


Fig. 3.10. Imaginary part of the effective surface impedance $Z_s^{eff}$ for a YBCO film at 125 K. The imaginary part of the dc sheet resistance is zero.

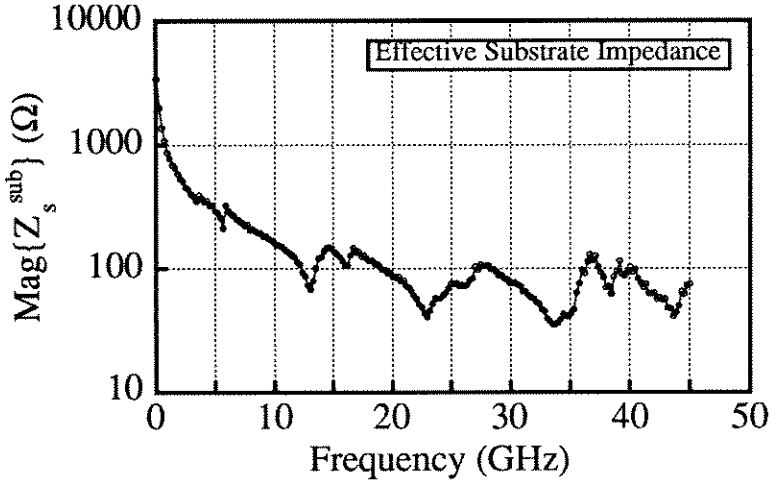


Fig. 3.11. Effective substrate impedance derived from effective impedance data at 125 K.

## 3.5 Error Correction Procedure

It is clear that the simple calibration scheme outlined in section 3.2 is not adequate to handle the further errors discussed in sections 3.3 and 3.4. The full error correction procedure that has been developed in this chapter to deal with the specific difficulties outlined above will be summarized in detail in this section.

### 3.5.1 Procedure for Zero-Field Measurements

The full error correction procedure is summarized schematically in Fig. 3.12, and can described by the following steps. In step 1 the reflection coefficient is measured at the temperature of interest utilizing the room temperature error coefficients as described above. This data is corrected for the temperature dependent changes in the cables during the temperature ramp in step 2 by directly subtracting off the changes in the measured response of a thick silver film measured over the same temperature interval that is used for the superconductor measurement. Following the background subtraction, the updated error coefficients, which are calculated in the reference state at low temperature, are applied in step 3. (The updated error coefficients, of course, give the calculated reference response when applied to the data at the reference temperature.) In step 4 the effective surface impedance is calculated by inverting Eq. 3.1, with $Z_0$ given by the field impedance of the TEM mode in the coaxial line [$Z_0 = \sqrt{(\mu/\varepsilon_r\varepsilon_0)} = 377\Omega/\sqrt{\varepsilon_r}$, where $\mu$ is the permeability and $\varepsilon_r$ is the relative permittivity of the dielectric material of the coaxial cable, and $\varepsilon_r$=2 for Teflon]. In step 5 the data is corrected for substrate effects as described in section 3.4, yielding the complex impedance as a function of frequency at the temperature of interest.

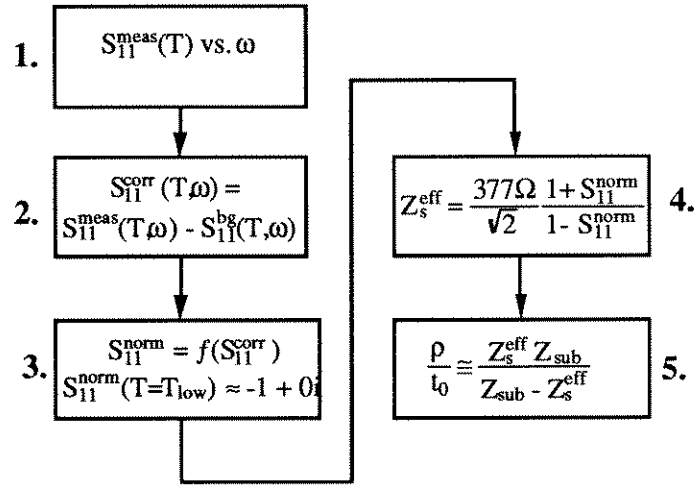


Fig. 3.12. Schematic diagram of the error correction procedure used in the zero-field measurements.

### 3.5.2 Procedure for Magnetic Field Measurements

The error correction procedure for the finite field measurements is slightly more complicated than that for the zero-field case, primarily due to the fact that for these measurements the transmission line must be disconnected from the source after calibration in order to mount the sample and load it into the magnet (see section 2.2.2). The disconnection of the transmission line results in additional errors so that the procedure described in section 3.5.1 is no longer the optimum one. In what follows a more accurate procedure for temperature-dependent measurements in the finite field setup is described (shown schematically in Fig. 3.13), followed by the procedure for the magnetic field-dependent measurements.

For temperature-dependent measurements in the finite-field procedure, steps 1 and 2 are the same as above. The difference comes about in step 3, where in the finite-field procedure two reference states, one below and one above $T_c$ are used to recalculate two of the error coefficient $E_R$ and $E_S$. After step 3 the effective impedance is calculated as above. Since a second reference state above $T_c$ is used in this procedure, it is only valid for samples for which the substrate effects described above are negligible, or for samples for which the substrate contribution is known.

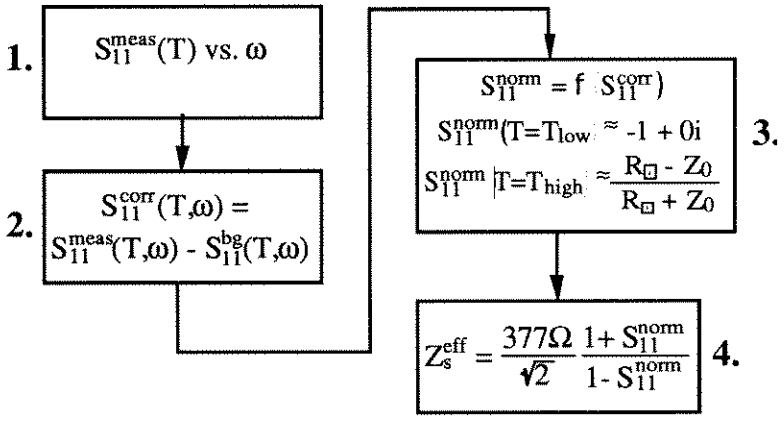


Fig. 3.13. Schematic diagram of complete error correction procedure used in the finite-field measurements.

The error correction procedure for magnetic field-dependent measurements is much simpler, because it is assumed that there are no field-dependent changes to the properties of the coaxial transmission line. The procedure used here is to assume that the zero-field frequency dependence is known (either from a temperature-dependent measurement, or from a theoretical calculation), and the measurement of the zero-field state is used to update the error coefficient $E_R$. There is only this one reference state known in the magnetic field dependent measurements, so only one error coefficient can be recalculated. This is usually sufficient, since the changes in the effective impedance with field are often smaller than the changes in the effective surface impedance with temperature. If greater accuracy is required, the updated error coefficient $E_S$ can be used from the temperature-dependent measurement.

In summary, this chapter has described the development and implementation of a novel low-temperature calibration scheme that is used to accurately calibrate the Corbino reflection technique for the measurement of thin film samples from 45 MHz - 50 GHz over the temperature range from 4.2 - 300 K.

## Chapter 3 References


[1] N. Klein, H. Chaloupka, G. Muller, S. Orbach, H. Piel, B. Roas, L. Shultz, U. Klein and M. Peiniger, J. Appl. Phys. 67, 6940 (1990).

[2] L. Drabeck, K. Holczer, G. Gruner and D. Scalapino, J. Appl. Phys. 68, 892 (1990).

[3] P. Hartemann, IEEE Trans. Applied Superconductivity 2, 228 (1992).

[4] See, for example, Hewlett Packard Application Note 183, p.39 (1978).

[5] S. Ramo, J.R. Whinnery, and T. Van Duzer, "Fields and Waves in Communication Electronics", Second Edition, John Wiley and Sons, New York (1984), p.252.

# Chapter 4

# Electromagnetic Field Distribution in the Corbino Geometry

## 4.1 Introduction

Broadband measurements in the microwave regime can be utilized to gain important information about the frequency dependence of the electrodynamic response of a wide range of materials. One approach to broadband measurements is to use the TEM mode in a coaxial waveguide in order to avoid the restriction of operating above a fixed cutoff frequency. There exist many examples of measurements that utilize an open-ended coaxial probe in order to measure dielectric constants of solids,[1] liquids,[2,3] and even living tissue.[4,5,6]

The particular geometry that is used in this work is shown in Fig. 4.1, and corresponds to an abrupt coaxial to circular waveguide transition (the cylindrical copper housing shown in Fig. 2.4 corresponds to the circular waveguide section). Calculations of the frequency response of such a discontinuity have been accomplished using a number of different theoretical techniques.[7,8,9] This chapter will focus on the development of a calculation based on a mode-matching technique that is used to mathematically model the frequency response in this geometry, in order to better understand the measured data obtained on superconductors. In particular, it is desirable to be able to calculate the effect of radiation propagating through a metallic or superconducting thin film sample into the substrate in the Corbino geometry, in order to understand the frequency response of the substrate effect discussed in section 3.4. In addition, such a calculation could be used to model the response of more complicated samples, such as superconductor/insulator structures and multilayers.

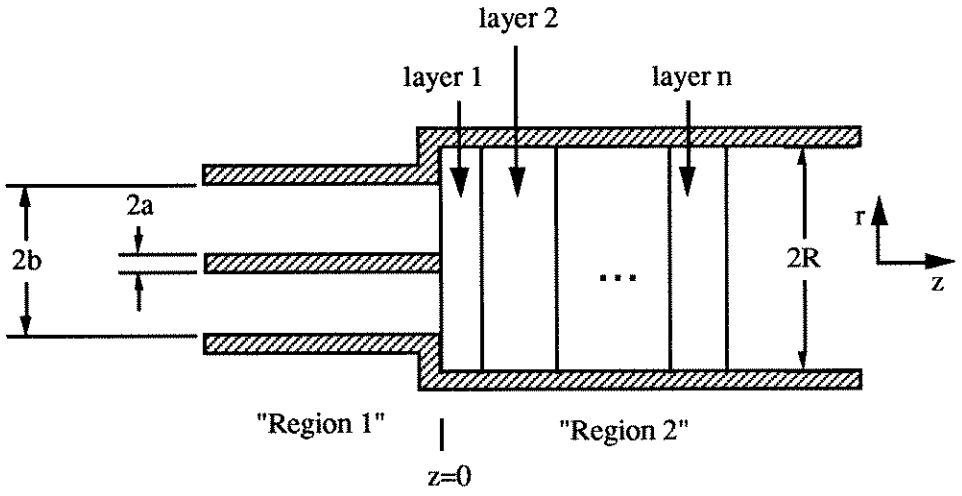


Fig. 4.1. Schematic diagram of coaxial/circular waveguide interface.

The objective of this calculation is to obtain an expression for the frequency-dependent reflection coefficient $S_{11}(\omega)$ at the location of the transition (z=0 in Fig. 4.1) for the general case of an arbitrary combination of metallic (or superconducting) and/or dielectric layers in the circular waveguide region (region 2). To accomplish this, first the normal modes for the two waveguide regions are calculated from Maxwell's equations in section 4.2. In section 4.3 the general mode-matching technique used to calculate the reflection coefficient of the TEM mode at the discontinuity is described, and in section 4.4 the coupling coefficients between the coaxial waveguide modes and the circular waveguide modes are calculated. In section 4.5 the frequency-dependent reflection coefficient is calculated for a number of different uniform dielectric materials filling the circular guide (including air, Teflon, and sapphire), and compared with actual measurements of these materials. Then in section 4.6 the substrate effect for thin metallic layers is modeled, and the frequency dependence of the substrate impedance is calculated and compared to that derived from actual measurements.

## 4.2 Waveguide Modes

### 4.2.1 Waveguide Equations

We begin,[10] as usual, by writing down Maxwell's equations:

$$\begin{aligned} \nabla\times\mathbf{H} &= \mathbf{J} + \frac{\partial \mathbf{D}}{\partial t} & \nabla\cdot\mathbf{D} &= \rho \\ \nabla\times\mathbf{E} &= -\frac{\partial \mathbf{B}}{\partial t} & \nabla\cdot\mathbf{B} &= 0 \end{aligned} \tag{4.1}$$

We assume a periodic time dependence of $e^{+i\omega t}$ for all fields and currents, and also assume the constitutive relations $J=\sigma E$, and $B=\mu H$. Then the time dependent Maxwell's equations can be written as

$$\nabla\times\mathbf{H} = i\omega\varepsilon\mathbf{E} \qquad \nabla\times\mathbf{E} = -i\omega\mu\mathbf{H} \tag{4.2}$$

with $\varepsilon=\varepsilon_0(\varepsilon_r - i\sigma/\omega\,\varepsilon_0)$. Combining the above equations yields the wave equation for E and H:

$$\left(\nabla^2 + \omega^2\mu\varepsilon\right)\begin{Bmatrix}\mathbf{E}\\ \mathbf{H}\end{Bmatrix} = 0 \tag{4.3}$$

We now assume a spatial variation of the fields in the z-direction of

$$\begin{aligned} \mathbf{E} &\sim \mathbf{E}(x,y)\, e^{(i\omega t \pm \gamma z)} \\ \mathbf{H} &\sim \mathbf{H}(x,y)\, e^{(i\omega t \pm \gamma z)} \end{aligned} \tag{4.4}$$

Writing the gradient operator as $\nabla^2 = \nabla_t^2 + \partial^2/\partial z^2$ gives the following equations for E and H:

$$\nabla_t^2\begin{Bmatrix}\mathbf{E}\\ \mathbf{H}\end{Bmatrix} = -\left(\gamma^2 + \omega^2\mu\varepsilon\right)\begin{Bmatrix}\mathbf{E}\\ \mathbf{H}\end{Bmatrix} \tag{4.5}$$

Note that $\gamma$ is found by solving equations (4.5) subject to the appropriate boundary conditions.

It is also useful to separate out the z-component of the fields, writing

$\mathbf{E}=\mathbf{E}_t+E_z\mathbf{k}$, and $\mathbf{B}=\mathbf{B}_t+B_z\mathbf{k}$, where $\mathbf{k}$ is a unit vector in the z-direction. Combining these expressions with the expanded form of the gradient operator ($\nabla^2 = \nabla_t^2 + \partial^2/\partial z^2$) allows one to rewrite Maxwell's equations in a form which explicitly separates the transverse and z components of the fields. From the first expression in Eq. 4.2, $\nabla\mathbf{x}\mathbf{H}=i\omega\varepsilon\mathbf{E}$ one obtains the following equations

$$\mathbf{k}\cdot\left(\nabla_t\times\mathbf{H}_t\right)=i\omega\varepsilon E_z \tag{4.6}$$

$$\frac{\partial\mathbf{H}_t}{\partial z}+i\omega\varepsilon\,\mathbf{k}\times\mathbf{E}_t=\nabla_t H_z \tag{4.7}$$

Similarly, from $\nabla\mathbf{x}\mathbf{E}=-i\omega\mu\mathbf{H}$ one obtains

$$\mathbf{k}\cdot\left(\nabla_t\times\mathbf{E}_t\right)=-i\omega\mu H_z \tag{4.8}$$

$$\frac{\partial\mathbf{E}_t}{\partial z}-i\omega\mu\,\mathbf{k}\times\mathbf{H}_t=\nabla_t E_z \tag{4.9}$$

Also, decomposing $\nabla\cdot\mathbf{D}=0$ and $\nabla\cdot\mathbf{B}=0$ gives

$$\nabla_t\cdot\mathbf{E}_t=-\frac{\partial E_z}{\partial z}\qquad\nabla_t\cdot\mathbf{H}_t=-\frac{\partial H_z}{\partial z} \tag{4.10}$$

The electromagnetic field configuration inside a waveguide can be expressed in terms of a complete set of orthogonal modes. These modes can be categorized by the presence or absence of the z-component of the electric or magnetic field, and are designated as TM (transverse magnetic, $H_z=0$), TE (transverse electric $E_z=0$), or TEM (transverse electromagnetic, $H_z=E_z=0$). The general procedure to obtain expressions for the modes in a cylindrical waveguide is as follows. First, solve Eq. 4.5 for $E_z$ or $H_z$ subject to the appropriate boundary conditions. Then use Eqs. 4.6-4.9 to solve for the transverse components of the field once $E_z$ or $H_z$ is known. This procedure will be used in the following sections to calculate the appropriate modes in a coaxial waveguide and in a circular waveguide.

### 4.2.2 Coaxial TEM Mode

The TEM mode has by definition no z-component for both the electric and magnetic fields. Substituting $H_z=E_z=0$ into Eqs. 4.8 and 4.10 gives the following equations for $\mathbf{E}_t$

$$\nabla_t \times \mathbf{E}_t = 0 \qquad \nabla_t \cdot \mathbf{E}_t = 0 \tag{4.11}$$

with similar equations for $\mathbf{H}_t$. The transverse electric field in the TEM mode can therefore be found by solving the following equation

$$\nabla_t^2 \mathbf{E}_t = 0 \tag{4.12}$$

Note that Eq. 4.12 combined with Eq. 4.5 gives the propagation constant for the TEM mode as $\gamma = \pm i\omega\sqrt{(\mu\varepsilon)}$, independent of the geometry of the system.

A solution to Eq. 4.12 in cylindrical coordinates is given by

$$\mathbf{E}_t = E_r(r,\theta) = \frac{A_0}{r} \tag{4.13}$$

where $A_0$ is a constant to be determined from normalization. The general normalization condition is $\int |e_j|^2 \cdot dA = 1$, where $e_j$ is the jth mode in the waveguide and the integration is carried out over the cross-sectional area of the waveguide. For the TEM mode in a coaxial waveguide of inner and outer radius a and b respectively, this normalization condition gives

$$E_r(r,\theta) = \frac{1}{\sqrt{2\pi \ln(b/a)}} \frac{1}{r} \tag{4.14}$$

The transverse magnetic field for the coaxial TEM mode can be found from Eq. 4.7 or Eq. 4.9, using the assumed z-dependence given by Eq. 4.4 and the fact that $E_z=H_z=0$, and for a wave traveling in the +z direction is given by

$$\mathbf{H}_t = \frac{i\omega\varepsilon}{\gamma}(\mathbf{k} \times \mathbf{E}_t) = \frac{\sqrt{(\varepsilon/\mu)}}{\sqrt{2\pi \ln(b/a)}} \frac{\hat{\phi}}{r} \tag{4.15}$$

Note that this gives for the field impedance of the coaxial TEM mode the following

$$Z_{TEM} = \frac{E_r}{H_\phi} = \sqrt{\frac{\mu}{\varepsilon}} \tag{4.16}$$

### 4.2.3 Higher Order Coaxial Modes

In addition to the TEM mode, higher order modes can be present in a coaxial transmission line. Under normal circumstances, the operating frequency of the coaxial transmission line is below the cutoff of any higher order modes, so that only the TEM mode (which has no cutoff frequency) can propagate. Higher order modes can be excited at the location of any discontinuity in the transmission line, and can make important contributions in these regions. In this section the orthonormal $TM_{mn}$ modes with m=0 will be calculated. TM modes with m≠0 and TE modes will not occur for an azimuthally symmetric coaxial waveguide.

To obtain the $TM_{0N}$ modes in the circular coaxial waveguide it is necessary to solve Eq. 4.5 in cylindrical coordinates for the z-component of the electric field, subject to the appropriate boundary conditions. The equation to solve is

$$\frac{1}{r}\frac{\partial}{\partial r}\left(r\frac{\partial E_z}{\partial r}\right) + \frac{1}{r^2}\frac{\partial^2 E_z}{\partial r^2} = -\alpha^2 E_z \tag{4.17}$$

where $\alpha^2 = (\gamma^2 + \omega^2\mu\varepsilon)$. This is simply Bessel's equation, and the azimuthally symmetric solutions for the coaxial region are a linear combination of Bessel and Neumann functions of order 0. The boundary conditions to be enforced are $E_z(r=a) = E_z(r=b) = 0$, and the solution is

$$E_z(r,\phi) = K\left[J_0(\alpha_{0N}\, a)\, N_0(\alpha_{0N}\, r) - N_0(\alpha_{0N}\, a)\, J_0(\alpha_{0N}\, r)\right] \tag{4.18}$$

where K is a constant and the eigenvalues $\alpha_{0N}$ are the solutions to

$$[J_0(\alpha_{0N}\,a)\,N_0(\alpha_{0N}\,b) - N_0(\alpha_{0N}\,a)\,J_0(\alpha_{0N}\,b)] = 0 \tag{4.19}$$

The first few eigenvalues for 2a=0.020" and 2b=0.065" are $(\alpha_{01} - \alpha_{04})$ = (1.3749, 2.7821, 4.1826, 5.5832).

The transverse fields are found by combining Eqs. 4.7 and 4.9 with $E_z$ given by 4.18, and are given by

$$E_r(r,\phi) = \frac{\gamma K_N}{\alpha_{0N}}[J_0(\alpha_{0N}\,a)\,N_1(\alpha_{0N}\,r) - N_0(\alpha_{0N}\,a)\,J_1(\alpha_{0N}\,r)] \tag{4.20}$$

$$H_\phi(r,\phi) = \frac{-i\omega\varepsilon K_N}{\alpha_{0N}}[J_0(\alpha_{0N}\,a)\,N_1(\alpha_{0N}\,r) - N_0(\alpha_{0N}\,a)\,J_1(\alpha_{0N}\,r)] \tag{4.21}$$

The constant $K_N$ will be determined from the normalization condition. Note that the field impedance of the TM modes is given by

$$Z_{TM} = \frac{E_r}{H_\phi} = \frac{i\gamma_N}{\omega\varepsilon} \tag{4.22}$$

where the propagation constant of the $TM_{0N}$ mode is given by $\gamma_N = \sqrt{(\alpha_{0N}^2 - \omega^2\mu\varepsilon)}$ (see Eq. 4.17).

The normalization constant $K_N$ is determined by demanding that the integral $|E_r|^2$ over the cross-sectional area of the coaxial waveguide be equal to unity. The result for the normalized modes $e_r$ is

$$e_r = \frac{1}{\sqrt{\pi}} \frac{Z_1(\alpha_{0N}r)}{\sqrt{b^2[Z_1(\alpha_{0N}b)] - a^2[Z_1(\alpha_{0N}a)]}} \tag{4.23}$$

The function $Z_1(\alpha_{0N}r)$ is simply a linear combination of Neumann and Bessel functions, given by $Z_1(\alpha_{0N}r) = J_0(\alpha_{0N}a)N_1(\alpha_{0N}r) - N_0(\alpha_{0N}a)J_1(\alpha_{0N}r)$.

### 4.2.4 Circular Waveguide Modes

To find expressions for the modes in a circular waveguide of radius $r_0$, the same procedure is followed as in section 4.2.3 above, with slightly different boundary conditions. The same considerations concerning azimuthal symmetry apply, so that the only modes allowed in the circular waveguide are the $TM_{0N}$, as was the case for the circular coaxial waveguide. The expression to solve for $E_z$ is given by Eq. 4.17, subject to the boundary conditions that $E_z(r=r_0)=0$, and $E_z(r=0)$ remain finite. The resulting solution for $E_z$ is

$$E_z(r,\phi) = A_N J_0\left(\frac{x_{0N}}{r_0} r\right) \tag{4.24}$$

where $J_0(x)$ is the Bessel function of order 0 and $x_{0N}$ is the nth root of $J_0(x_{0N})=0$. The propagation constant for this case is given by $\gamma_N^2 = (x_{0N}/r_0)^2 - \omega^2\sqrt{(\mu\varepsilon)}$. The corresponding expressions for the transverse electric and magnetic fields are also found in a manner analogous to section 4.2.3, and are given by

$$E_r(r,\phi) = \frac{\gamma_N A_N}{\alpha_{0N}} J_1\left(\frac{x_{0N}}{r_0} r\right) \tag{4.25}$$

$$H_\phi(r,\phi) = \frac{-i\omega\varepsilon A_N}{\alpha_{0N}} J_1\left(\frac{x_{0N}}{r_0} r\right) \tag{4.26}$$

Once again the field impedance of the TM modes is given by 4.22.

The constant $A_N$ is as usual found from the normalization condition. The fully normalized expression for the electric field is given by

$$e_r(r,\phi) = \frac{J_1\left(\frac{x_{0N}}{r_0} r\right)}{r_0 \sqrt{\pi}\, J_1(x_{0N})} \tag{4.27}$$

The normalized $h_\phi$ can of course be found from 4.27 and the expression for the field impedance, Eq. 4.22.

## 4.3 Mode Matching Calculation

In this section a general procedure for calculating the reflection coefficient at a discontinuity is described.[11] The fields on each side of the discontinuity (referred to as region 1 and region 2) are written in terms of the complete set of normal modes for the appropriate region. Then the coupling between the individual modes in each region at the location of the discontinuity is calculated. The goal in this work is to be able to calculate the reflection coefficient of the TEM mode in the coaxial transmission line as a function of the dielectric constant or conductivity of the material or materials filling the circular waveguide. Although we are interested in only the reflection coefficient of the coaxial TEM mode, it is necessary in general to include the effects of higher order modes in the coaxial transmission line because these modes are necessary to satisfy the boundary conditions on the electric and magnetic fields at the discontinuity.

### 4.3.1 Expansion in Normal Modes

The fields in each region are written in terms of forward (toward the interface) and backward (away from the interface) traveling waves. The electric and magnetic fields in region 1 can then be written as

$$E_r^{(1)} = \sum_{i=1}^{m} \left(F_i^{(1)} + B_i^{(1)}\right) \vec{e_i^{(1)}} \tag{4.28}$$

$$H_\phi^{(1)} = \sum_{i=1}^{m} \frac{\left(F_i^{(1)} - B_i^{(1)}\right)}{Z_i^{(1)}} \vec{e_i^{(1)}} \tag{4.29}$$

where $e_i^{(1)}$ is the normalized electric field for the mode i in region 1, and $Z_i^{(1)}$ is the field impedance of the mode i in region 1. The corresponding expressions for region 2 are

$$E_r^{(2)} = \sum_{j=1}^{n} \left(F_j^{(2)} + B_j^{(2)}\right) \vec{e}_j^{(2)} \tag{4.30}$$

$$H_\phi^{(2)} = -\sum_{j=1}^{n} \frac{\left(F_j^{(2)} - B_j^{(2)}\right)}{Z_j^{(1)}} \vec{e}_j^{(2)} \tag{4.31}$$

The minus sign in 4.31 comes from the different propagation directions for $F_j^{(2)}$ and $B_j^{(2)}$ relative to $F_i^{(1)}$ and $B_i^{(1)}$. The summations in Eqs. 4.28 - 4.31 in principle run to infinity, although in the calculations described later, only a finite number of modes are considered in the actual calculation.

### 4.3.2 Application of Boundary Conditions

Having expressed the fields in region 1 and region 2 in terms of normal modes, the next step is to enforce the appropriate boundary conditions at the location of the discontinuity (z=0 in Fig. 4.1). For the time being, it will be assumed that the walls of the waveguides are perfect conductors, and that the dielectric filling each region is lossless. Also, for the experimental configurations of concern here, the radius of the circular waveguide is greater that the outer radius of the coaxial waveguide (R>b).

The boundary condition that must be enforced at z=0 is simply that the transverse components of the **total** electric and magnetic fields must be continuous. The continuity of $E_t$ at z=0 is written as

$$\begin{aligned} \mathbf{E}_t^{(1)}(z=0) &= \mathbf{E}_t^{(2)}(z=0) \qquad a < r < b \\ 0 &= \mathbf{E}_t^{(2)}(z=0) \qquad r < a;\ r > b \end{aligned} \tag{4.32}$$

The second line in Eq. 4.32 is a consequence of the assumption of perfect conductivity in the walls of the waveguides. The next step is to write the transverse electric field in terms of the normal modes for each region. Substituting Eqs. 4.28 and 4.30 gives

$$\sum_{j=1}^{n}\left(F_j^{(2)}+B_j^{(2)}\right)\overrightarrow{e_j^{(2)}}=\sum_{i=1}^{m}\left(F_i^{(1)}+B_i^{(1)}\right)\overrightarrow{e_i^{(1)}} \qquad a<r<b$$
$$=0 \qquad r<a;\ r>b \tag{4.33}$$

The next step is to take the dot product of both sides of Eq. 4.33 with $\mathbf{e}_k^{(2)*}$, and integrate over the cross-sectional area of region 2:

$$\sum_{j=1}^{n}\left(F_j^{(2)}+B_j^{(2)}\right)\int_{S_2}\overrightarrow{e_j^{(2)}}\cdot\overrightarrow{e_k^{(2)*}}\,dS_2 =$$
$$\sum_{i=1}^{m}\left(F_i^{(1)}+B_i^{(1)}\right)\left[\int_{S_1}\overrightarrow{e_i^{(1)}}\cdot\overrightarrow{e_k^{(2)*}}\,dS_1+\int_{S_2-S_1}0\cdot\overrightarrow{e_k^{(2)*}}\,d(S_2-S_1)\right] \tag{4.34}$$

Utilizing the fact that the modes are orthonormal in region 2 gives

$$F_j^{(2)}+B_j^{(2)}=\sum_{i=1}^{m}P_{ji}\left(F_i^{(1)}+B_i^{(1)}\right) \tag{4.35}$$

where $P_{ji}$ is defined by

$$P_{ji}=\int_{S_1}\vec{e}_i^{(1)}\cdot\vec{e}_j^{(2)}\,dS_1 \tag{4.36}$$

where the integral is evaluated over the cross-sectional area of region 1.

Applying the same boundary condition to the tangential H field, then multiplying by $e_k^{(1)*}$ and integrating over the cross-sectional area of region 1 yields the following additional equation

$$F_i^{(1)}-B_i^{(1)}=-Z_i^{(1)}\sum_{j=1}^{n}\left(F_j^{(2)}-B_j^{(2)}\right)Y_j^{(2)}P_{ji} \tag{4.37}$$

where $Z_i^{(1,2)}$ and $Y_i^{(1,2)}$ are the field impedance and admittance, respectively, of the given mode in each region.

The set of coefficients $F_i$ and $B_i$, etc. can be written as 1-column matrices

$$\vec{F}^{(1)} = \begin{pmatrix} F_1^{(1)} \\ F_2^{(1)} \\ \vdots \\ F_m^{(1)} \end{pmatrix} \quad ; \quad \vec{B}^{(1)} = \begin{pmatrix} B_1^{(1)} \\ B_2^{(1)} \\ \vdots \\ B_m^{(1)} \end{pmatrix} \tag{4.38}$$

with analogous expressions for region 2. Then Eqs. 4.36 and 4.37 can be rewritten in the following form

$$\vec{F}^{(2)} + \vec{B}^{(2)} = \mathbf{P} \cdot \left(\vec{F}^{(1)} + \vec{B}^{(1)}\right) \tag{4.39}$$

$$\vec{F}^{(1)} - \vec{B}^{(1)} = -\mathbf{Z}^{(1)} \cdot \mathbf{P}^{\mathbf{T}} \cdot \mathbf{Y}^{(2)} \cdot \left(\vec{F}^{(2)} - \vec{B}^{(2)}\right) \tag{4.40}$$

In the above expressions, **P** is an m x n dimensional matrix whose elements $P_{ij}$ are given by 4.36. Also, $Z^{(1)}$ is an m x m dimensional diagonal matrix, whose elements $z_{ii}^{(1)}$ are the field impedance for the mode i in region 1. Likewise, $Y^{(2)}$ is an n x n dimensional diagonal matrix whose elements $y_{jj}^{(2)}$ correspond to the field admittance for mode j in region 2.

### 4.3.3 Scattering Matrix Formulation

In order to establish the scattering matrix formulation of the mode-matching calculation, it is necessary to relate the coefficients of the backward traveling waves, $B^{(1)}$ and $B^{(2)}$ (in the notation of Eqs. 4.38) to the coefficients of the forward traveling modes, $F^{(1)}$ and $F^{(2)}$. This is given by

$$\begin{aligned} B^{(1)} &= \mathbf{S}_{11}\, F^{(1)} + \mathbf{S}_{12}\, F^{(2)} \\ B^{(2)} &= \mathbf{S}_{21}\, F^{(1)} + \mathbf{S}_{22}\, F^{(2)} \end{aligned} \tag{4.41}$$

These relations define the four scattering matrices. From Eq. 4.41 it is clear that $\mathbf{S_{11}}$ is an m x m dimensional matrix that gives the reflection of the ith mode at the interface due to the incidence of the jth mode, etc.

In what follows the individual scattering matrices will be calculated in terms of

the field impedances (or admittances) of region 1 and region 2, and the coupling coefficients $P_{ji}$. The expressions are quite general, and are not limited only to the coaxial to circular interface shown in Fig. 4.1. In fact, the scattering matrix formulation will be used also to calculate the response at the interface of different dielectric material within the circular waveguide. In addition, the scattering matrices will be derived for the simple case of a uniform section of waveguide of finite electrical length.

#### 4.3.3.1 Interface Regions

From Eq. 4.41, it is clear that in order to identify the scattering matrices, it is necessary to simply obtain an expression for $B^{(1)}$ in terms of $F^{(1)}$ and $F^{(2)}$, and likewise for $B^{(2)}$ in terms of $F^{(1)}$ and $F^{(2)}$. This requires only that Eqs. 4.39 and 4.40 be solved simultaneously for the desired quantities. After some algebra the following expressions are obtained for the scattering matrices[11]

$$\mathbf{S}_{11} = \left[\mathbf{I} + \mathbf{Z}^{(1)}.\mathbf{P}^{T}.\mathbf{Y}^{(2)}.\mathbf{P}\right]^{-1}\left[\mathbf{I} - \mathbf{Z}^{(1)}.\mathbf{P}^{T}.\mathbf{Y}^{(2)}.\mathbf{P}\right] \tag{4.42}$$

$$\mathbf{S}_{12} = 2\left[\mathbf{I} + \mathbf{Z}^{(1)}.\mathbf{P}^{T}.\mathbf{Y}^{(2)}.\mathbf{P}\right]^{-1}\mathbf{Z}^{(1)}.\mathbf{P}^{T}.\mathbf{Y}^{(2)} \tag{4.43}$$

$$\mathbf{S}_{21} = 2\left[\mathbf{I} + \mathbf{P}.\mathbf{Z}^{(1)}.\mathbf{P}^{T}.\mathbf{Y}^{(2)}\right]^{-1}\mathbf{P} \tag{4.44}$$

$$\mathbf{S}_{22} = -1\left[\mathbf{I} + \mathbf{P}.\mathbf{Z}^{(1)}.\mathbf{P}^{T}.\mathbf{Y}^{(2)}\right]^{-1}\left[\mathbf{I} - \mathbf{P}.\mathbf{Z}^{(1)}.\mathbf{P}^{T}.\mathbf{Y}^{(2)}\right] \tag{4.45}$$

#### 4.3.3.2 Uniform Regions

The above equations represent the scattering matrices for any interface between two regions. For a complete description, it is also necessary to obtain expressions for

a homogeneous waveguide region of finite electrical length. For a transmission line of length $\ell$ and having a propagation constant $\gamma$, $\mathbf{S}_{11} = \mathbf{S}_{22} = \mathbf{0}$, and $\mathbf{S}_{12}$ and $\mathbf{S}_{21}$ are both diagonal, having matrix elements given by $(\mathbf{S}_{12})_{ii} = (\mathbf{S}_{21})_{ii} = \exp(-\gamma_i \ell)$.

### 4.3.4 Combination Formulae

Having obtained expressions for the scattering matrices for both interface regions and homogeneous regions, it only remains to determine how the S-matrices are combined together. To illustrate the process, consider the situation shown in Fig. 4.2, in which the total S-matrices for two regions, region a and region b, have already been determined.

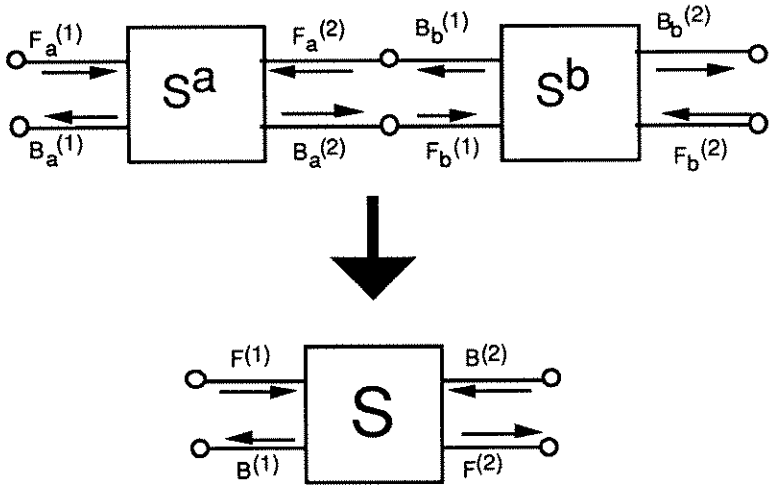


Fig. 4.2. Determination of the combination formulae for the scattering matrices.

It is then desirable to obtain the total S-matrices of the composite structure. Since the S-matrices relate the coefficients of the forward and backward traveling waves incident on each region, the S-matrices of the composite structure can be found by algebraically solving for the coefficients $B_a^{(1)}$and $B_b^{(2)}$ in terms of $F_b^{(2)}$ and $F_a^{(1)}$. Determination of the S-matrices for the composite structure is in practice accomplished by writing down Eqs. 4.41 for regions a and b, and using the relation $F_a^{(2)} = B_b^{(1)}$ and $B_a^{(2)} = F_b^{(1)}$ to eliminate the unwanted coefficients. The result is expressed in terms of the given S-

matrix written in terms of the individual S-matrices of regions a and b[11]

$$\begin{aligned} S_{11} &= S_{11}^{a} + S_{12}^{a}\left(I - S_{11}^{b}S_{22}^{a}\right)^{-1} S_{11}^{b}S_{21}^{a} \\ S_{12} &= S_{12}^{a}\left(I - S_{11}^{b}S_{22}^{a}\right)^{-1} S_{12}^{b} \\ S_{21} &= S_{21}^{b}\left(I - S_{22}^{a}S_{11}^{b}\right)^{-1} S_{21}^{a} \\ S_{22} &= S_{22}^{b} + S_{21}^{b}\left(I - S_{22}^{1}S_{11}^{b}\right)^{-1} S_{22}^{a}S_{12}^{b} \end{aligned} \tag{4.46}$$

The combination formulae given above can be used to build up the total S-matrices of a more complicated configuration by calculating the S-matrices of the individual interfaces and homogeneous sections, and combining them according to Eqs. 4.46. This procedure is used in what follows to calculate the reflection coefficient $S_{11}$ of the TEM mode in the coaxial transmission line at the location of the coaxial/circular waveguide interface as a function of an arbitrary number of superconducting, normal conducting, and/or dielectric regions in the circular waveguide.

## 4.4 Coaxial to Circular Waveguide Transition

In order to complete the calculation it is necessary to calculate the coupling coefficients $P_{ji}$ for the coaxial to circular waveguide transition. The coupling matrix P between regions of circular waveguide that have different dielectric filling media is simply the unit matrix, since there will be no mixing of different modes for the same geometry. In this section the coupling coefficients for the coaxial to circular transition with the geometry shown in Fig. 4.1 will be calculated. This is simply the evaluation of the integral in Eq. 4.36, using the orthonormal modes for each region that were calculated in section 4.2. The effect of the finite conductivity of the waveguide walls will also be considered.

### 4.4.1 Calculation of the Coupling Coefficients $P_{ji}$

The first set of coefficients to calculate is $P_{j0}$, which correspond to the coupling from the coaxial TEM mode to the $TM_{0j}$ mode in the circular waveguide. Using Eqs. 4.14 and 4.27 in the $P_{ji}$ definition 4.36 gives

$$P_{j0} = \frac{1}{\sqrt{2\pi \ln(b/a)}} \frac{1}{r_0\sqrt{\pi}\, J_1(x_{0j})} \int_0^{2\pi} d\varphi \int_a^b \frac{1}{r} J_1\left(\frac{r}{r_0} x_{0j}\right) r\, dr \tag{4.47}$$

Evaluating the integral gives

$$P_{j0} = \sqrt{\frac{2}{\ln(b/a)}} \frac{1}{x_{0j}\, J_1(x_{0j})} [J_0(x_{0j}b/r_0) - J_0(x_{0j}a/r_0)] \tag{4.48}$$

The corresponding calculation for the coupling coefficients between the coaxial TM and the circular TM can be found by evaluating the following integral, which utilizes the normal modes from Eqs. 4.23 and 4.27

$$P_{ji} = \frac{1}{r_0\pi J_1(x_{0j})\left[b^2Z_1^2(\alpha_{0i}b) - a^2Z_1^2(\alpha_{0i}a)\right]^{1/2}} \int_0^{2\pi} d\phi \int_a^b J_1\left(\frac{r}{r_0} x_{0j}\right) \cdot Z_1(\alpha_{0i}r)\, r dr \tag{4.49}$$

with the result for the remaining $P_{ji}$

$$P_{ji} = \frac{2[b\, J_0(x_{0j}b/r_0)\, Z_1(\alpha_{0i}b) - a\, J_0(x_{0j}a/r_0)\, Z_1(\alpha_{0i}a)]}{J_1(x_{0j}) \cdot \left[b^2Z_1^2(\alpha_{0i}b) - a^2Z_1^2(\alpha_{0i}a)\right]^{1/2}} \cdot \frac{x_{0j}/r_0}{\left[(x_{0j}/r_0)^2 - (\alpha_{0i})^2\right]} \tag{4.50}$$

Recall that $x_{0j}$ is the $j^{th}$ zero of $J_0(x)$, and $\alpha_{0i}$ is found by solving Eq. 4.19, and $Z_1(x)$ is given in section 4.2.3.

### 4.4.2 Finite Conduction Losses

The effect of finite conduction losses in the walls of the circular waveguide is to modify the propagation constant $\gamma_i$ derived in section 4.2.3, by making it in general a complex quantity. In order to obtain an expression valid at and below the cutoff frequency of the mode under consideration, one needs to use the perturbation of boundary conditions technique. The modified expression for the propagation constant

$\gamma$ is given by[10]

$$\gamma^2 = \gamma_0^2 - \frac{2\omega\varepsilon}{r_0}\sqrt{\frac{i\omega\mu_0}{\sigma}} \tag{4.51}$$

where $\gamma_0$ is the unmodified expression for $\gamma$ given in section 4.2.3, $r_0$ is the radius of the waveguide, and $\sigma$ is the conductivity of the walls of the waveguide.

## 4.5 Reflection Coefficient of Dielectric Materials

One immediate application of the above formalism is to evaluate the dielectric constant as a function of frequency of a uniform dielectric material that fills the circular waveguide region. After measuring the frequency-dependent reflection coefficient of a layer of material with unknown dielectric constant, the above formalism can be used to calculate the frequency-dependent reflection coefficient while varying both the real and imaginary parts of the dielectric constant of the unknown layer. The above formalism could also in principle lead to a method by which the dielectric constant of the unknown material as a function of frequency could be directly calculated from the measured reflection coefficient. Such a procedure to determine the dielectric constant vs. frequency in the range 45 MHz-50 GHz would be extremely valuable for determining the dielectric response of some of the exotic dielectric materials used in making superconducting circuits, in particular thin film dielectrics.

The experimental set-up for measuring dielectric samples that is used is the one shown in figure 2.4, with the contacted film and substrate replaced by a dielectric material that uniformly fills the cylindrical copper housing.

### 4.5.1 Air

The simplest dielectric material to study is air, which is easily realized in practice by measuring the reflection coefficient of the empty

copper housing shown in Fig. 2.4. In this geometry the end cap of the housing is removed, along with the spring and copper pedestal. The calculation for such a geometry consists of a layer of uniform material with a relative dielectric constant of 1 + 0i of the appropriate thickness, backed by a uniform impedance of 377Ω, which represents the impedance of free space beyond the cavity.

The measured and calculated frequency response of the magnitude and phase of the reflection coefficient for an air-filled circular waveguide are shown in Fig. 4.3 (magnitude) and Fig. 4.4 (phase). Losses due to the waveguide walls are also included, with $\rho_{walls}=1x10^{-7}$ Ωm. Both the magnitude and the phase show good agreement between the calculation and theory, to within a few percent. The deviations at higher frequencies are most likely due to calibration errors. The most noticeable feature is the resonance that occurs at approximately 23 GHz, which corresponds to the cutoff frequency of the $TM_{01}$ mode in the air-filled circular waveguide.

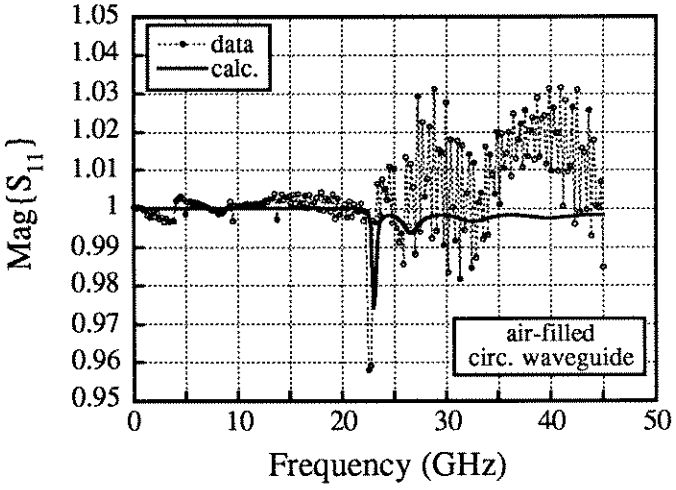


Fig. 4.3. Magnitude of the measured and calculated reflection coefficient of an air-filled circular waveguide as a function of frequency.

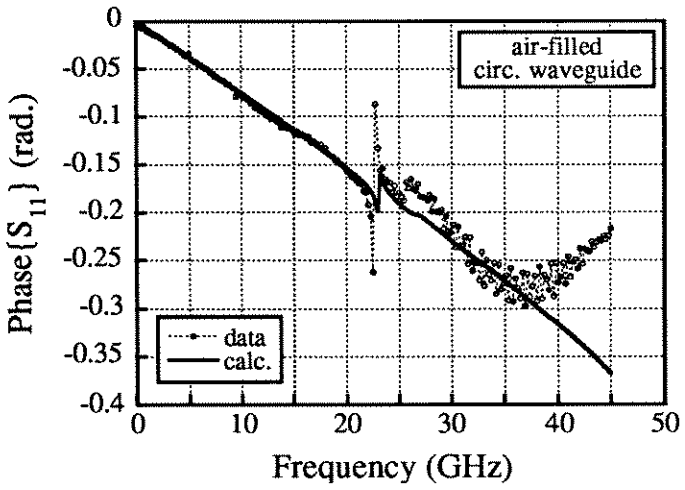


Fig. 4.4. Phase of the measured and calculated reflection coefficient of an air-filled circular waveguide as a function of frequency.

A practical use of this simple measurement could be as a calibration standard. One could use the air dielectric measurement, along with a measurement of a thick normal metal sample (as shown in Figs. 3.4 and 3.5, for example) as more accurate calibration standards for measurements performed utilizing this geometry. Also, by varying the value of the resistivity of the walls in the calculation one can obtain a good estimate for the contribution of the walls to the overall loss.

### 4.5.2 Teflon

Teflon represents a good choice to investigate the utility of the measurement system to obtain dielectric constants of bulk materials, in part because it is easy to machine into a shape which fits snugly into the circular waveguide. In this section, the reflection coefficient measurements of bulk Teflon will be presented for two different configurations, and compared with the calculated results in an effort to see how accurately the measurement system can be used to determine bulk dielectric properties, and to show some of the range of physical situations that can be simulated with the formalism described above.

The first measurement configuration is for a cylindrical sample 2.7 mm long which is inserted into the circular waveguide without a metallic pedestal. In order to simulate this configuration we calculate the response for a layer of dielectric of the appropriate thickness, followed by a layer of air also of the appropriate thickness, all of which is backed by the free space impedance, as discussed in section 4.5.1. The comparison of the measurement and the simulation is shown in Fig. 4.5 (magnitude) and Fig. 4.6 (phase). The calculation shown is for a relative dielectric constant of

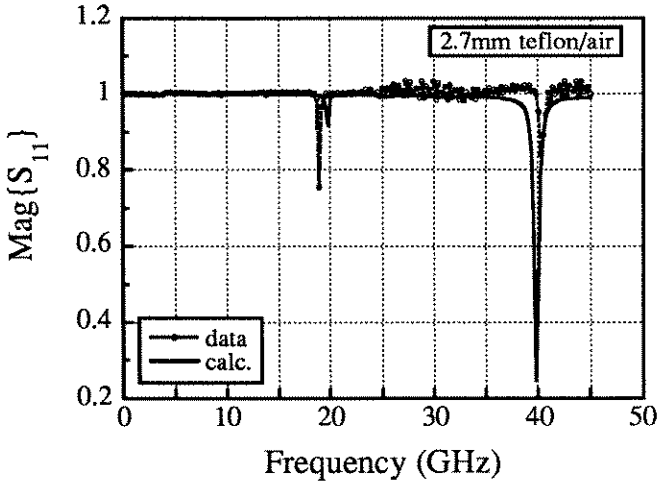


Fig. 4.5. Frequency dependence of the magnitude of the reflection coefficient for the 2.71 mm Teflon sample backed by air.

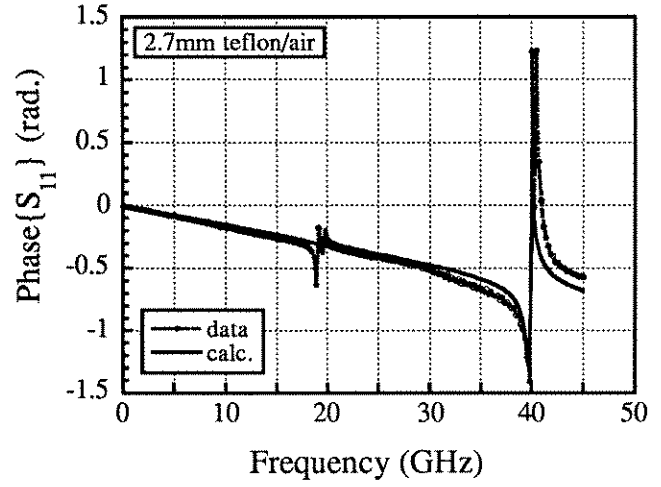


Fig. 4.6. Frequency dependence of the phase of the reflection coefficient for the 2.71 mm Teflon sample backed by air.

$\varepsilon_r$=2.0 -0.02i. The disagreement between data and calculation at high frequencies could be due to a dielectric constant that varies with frequency.

The second measurement configuration is for the a 5.4 mm thick Teflon sample, this time backed by a bulk copper pedestal. The calculation shown below in Figs. 4.7 and 4.8 assumes that the resistivity of the bulk copper pedestal is the same as the waveguide walls, $\rho_{Cu}=1x10^{-7}$ Ωm. In comparison to Figs. 4.5 and 4.6, the thicker Teflon sample shows a greater number of higher-order modes, which is what one would expect qualitatively for a larger sample.

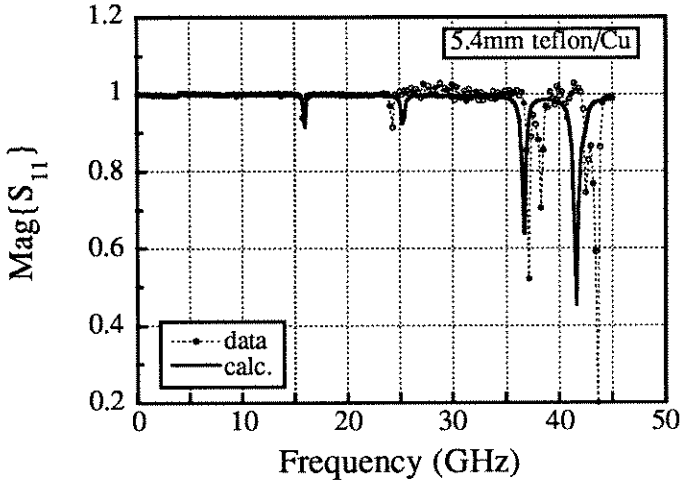


Fig. 4.7. Frequency dependence of the magnitude of the reflection coefficient for the 5.4 mm Teflon sample backed by a copper pedestal.

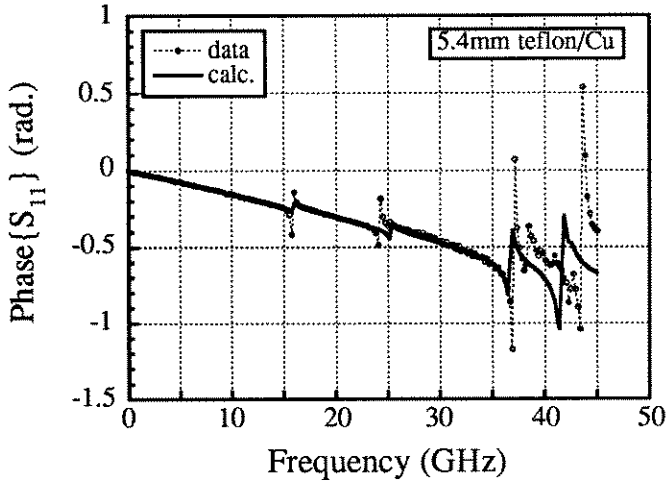


Fig. 4.8. Frequency dependence of the phase of the reflection coefficient for the 5.4 mm Teflon sample backed by a copper pedestal.

### 4.5.3 Sapphire

An example of a material used as a substrate for superconducting films is sapphire. For the dielectric measurements here, circular sapphire substrates were obtained of thickness 0.56 mm and diameter 0.4 inch, so that they would fit as snugly as possible into the circular waveguide. The orientation was R-plane, which is commonly used to grow high $T_c$ superconducting materials, but which has an anisotropic dielectric constant.[12] Figs. 4.9 and 4.10 show the data and simulations for a sapphire substrate, with a value for the relative dielectric constant of $\varepsilon_r$=10 + 0i for the simulation. The data clearly shows the effect of the smaller volume and much higher dielectric constant of sapphire relative to the Teflon, which give many more modes over the same frequency span. Also complicating the measurement is the fact that the dielectric constant in R-plane sapphire is not isotropic. In spite of these problems, however, we do obtain reasonable agreement between the measured phase and the simulation at low frequencies, where the number of propagating modes in the substrate is small.

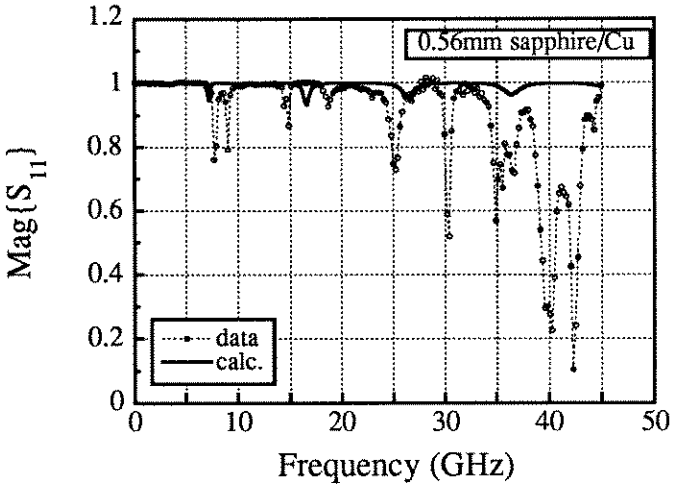


Fig. 4.9. Frequency dependence of the magnitude of the reflection coefficient for the 0.56 mm sapphire substrate backed by a copper pedestal.

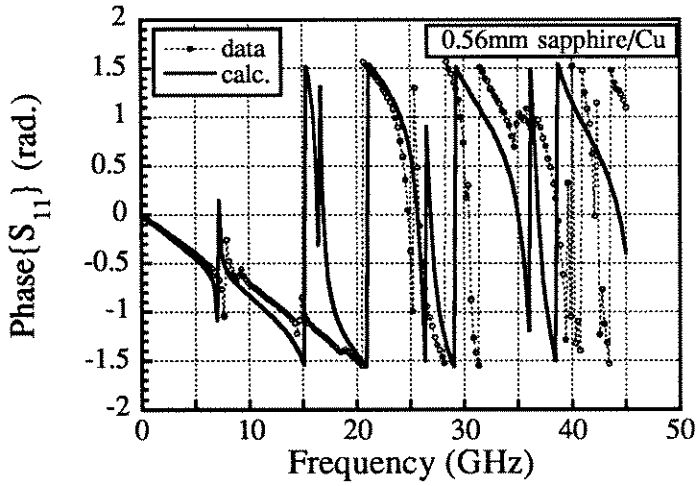


Fig. 4.10. Frequency dependence of the phase of the reflection coefficient for the 0.56 mm sapphire substrate backed by a copper pedestal.

## 4.6 Substrate Effect Calculation

The most useful result that can be obtained from the calculation outlined in this chapter for the work presented here on superconductors is the ability to calculate the contribution to the effective impedance of fields that propagate into the substrate. In section 3.4 a method was outlined by which it is possible to obtain a measure of the effective impedance of the substrate, but the functional form of the frequency-dependent substrate impedance was unknown. In this section that method will be verified by using the same procedure to extract the effective substrate impedance from simulated data, and comparing it directly with the calculated effective substrate impedance. The calculated frequency dependence of the substrate impedance will then be compared with the frequency dependence of the effective substrate impedance derived from normal state measurements of thin superconducting films in section 3.4.

Following the discussion of section 3.4, the first calculation is of the reflection coefficient of a thin normal metal film backed by a dielectric layer on a bulk metallic pedestal. This simulates the effective impedance $Z_s^{eff}(\omega)$ in equation 3.12. In order to simulate the dc resistivity data, the reflection coefficient of the normal metal thin film is

calculated in the limit of infinite substrate impedance (this corresponds to the assumption that at dc the impedance of the substrate is very large). The calculated reflection coefficients are then converted to impedances according to equation 3.1. In Figs. 4.11 and 4.12 the real and imaginary parts of the calculated effective impedance for the two cases are shown. Note that these figures are qualitatively very similar to the corresponding measured quantities shown in Figs. 3.9 and 3.10, which show the frequency response of a superconducting film in the normal state backed by a square substrate.

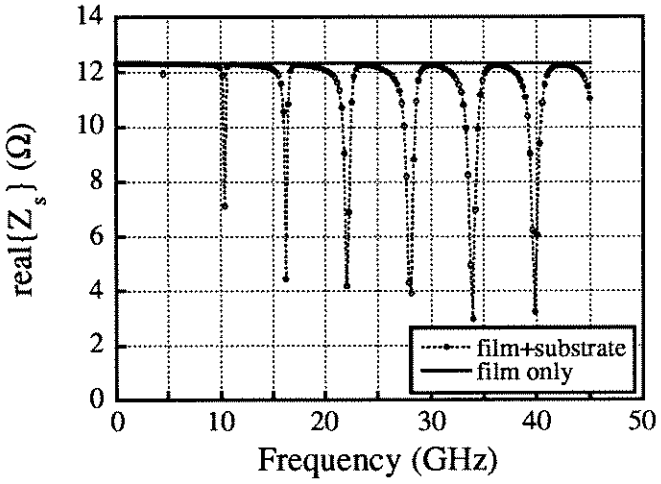


Fig. 4.11. Simulation of the frequency dependence of the real part of the impedance for a thin film plus a substrate, and the thin film alone.

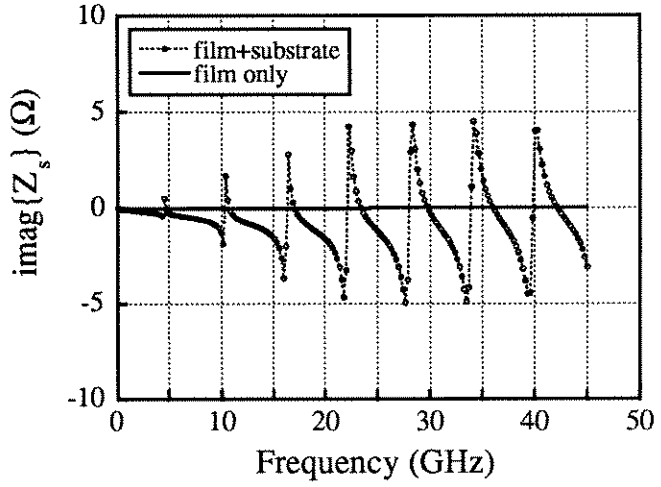


Fig. 4.12. Simulation of the frequency dependence of the imaginary part of the impedance for a thin film plus a substrate, and the thin film alone.

In order to derive the effective substrate impedance, Eq. 3.12 is applied to the simulated data shown above. The effective surface impedance derived in this way is shown in Fig. 4.13, along with the frequency dependence of the substrate impedance, calculated using the same parameters. This figure shows that the procedure outlined in section 3.4 to obtain the substrate impedance is valid. Also note the similar functional dependence on frequency of the calculated substrate impedance, and the substrate impedance derived from measurements in Fig. 3.11.

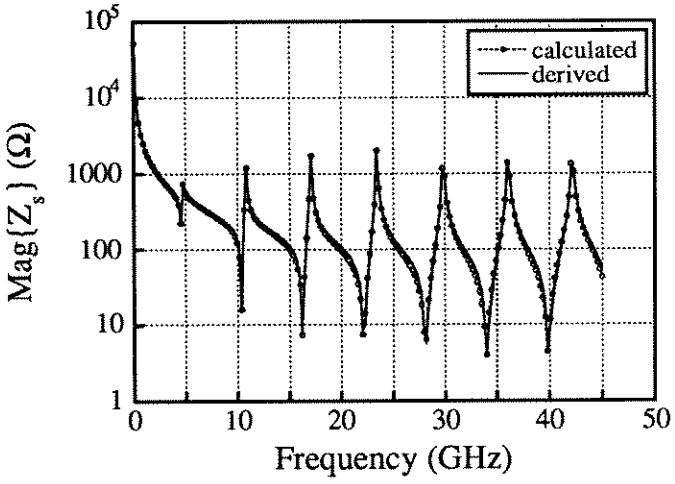


Fig. 4.13. The effective substrate impedance vs. frequency, derived from simulated data and calculated directly.

## Chapter 4 References


[1] Nour-Eddine Belhadj-Tahar, A. Fourrier-Lamar, and H. DeChanterac, IEEE Trans. Microwave Theory Tech. **38**, 1 (1990).

[2] Yan-Zhen Wei and S. Sridhar, Rev. Sci. Instrum. **60**, 3041 (1989).

[3] D. Misra, M. Chabbra, B.R. Epstein, M. Mirotznik, and K.R. Foster, IEEE Trans. Microwave Theory Tech. **38**, 8 (1990).

[4] L. L. Li, N. H. Ismail, L. S. Taylor, and C. C. Davis, IEEE Trans. Biomed. Eng. **39**, 49 (1992).

[5] M.A. Stuchly and S.S. Stuchly, IEEE Trans. Instrum. Meas. **29**, 176 (1980).

[6] E.C. Burdette, F.L. Cain, and J. Seals, IEEE Trans. Microwave Theory Tech. **28**, 414 (1980).

[7] G.B. Gajda and S.S. Stuchly, IEEE Trans. Microwave Theory Tech. **31**, 380 (1983).

[8] M. Razaz and J.B. Davies, IEEE Trans. Microwave Theory Tech. **27**, 564 (1979).

[9] M. A. Saed, S. M. Riad, and W. A. Davis, IEEE Trans. Microwave Theory Tech. **39**, 485 (1990).

[10] J.D. Jackson, Classical Electrodynamics, Second Edition, John Wiley and Sons, New York (1975), p. 339 ff.

[11] G. L. James, IEEE Trans. Microwave Th. Tech. **29**, 1059 (1981).

[12] Z. Y. Shen, High - Temperature Superconducting Microwave Circuits Artech House, Boston (1994).

# Chapter 5
# Fluctuation Effects in the Conductivity of YBCO Thin Films

## 5.1 Introduction -- Fluctuations in Superconductors

Fluctuation effects in the vicinity of phase transitions have drawn much interest in recent years. In the high temperature superconductors it is believed that fluctuation effects are larger, and the region of temperature over which they are important is much wider than in their low temperature counterparts, allowing for fluctuations to be studied in far greater detail in these superconducting systems.[1] The high $T_c$ superconductors may also provide the opportunity to measure critical behavior near the superconducting phase transition,[2] which is precluded in the low $T_c$ systems because the critical regime is unobservably narrow.

The effects of thermal fluctuations near a critical point can be observed in a number of different experimental quantities, such as the specific heat, susceptibility, dc conductivity, etc. In this chapter the effects of fluctuations on the microwave conductivity of high $T_c$ superconductors (primarily above $T_c$) are investigated in detail.

This chapter describes a systematic study of dynamical fluctuation effects in the temperature and frequency dependent conductivity of YBCO thin films measured over three decades of frequency in the microwave range (45 MHz - 45 GHz). Previous observations of the ac fluctuation conductivity have been reported in the temperature dependence of the conductivity of thin lead films at (discrete) microwave frequencies by Lehoczky and Briscoe[3], while Tanner measured the frequency dependence of the fluctuation conductivity at far-infrared frequencies, also using thin lead films.[4] Both experimental studies found quantitative agreement with the 2D Gaussian fluctuation theory, based on time dependent Ginzburg-Landau theory. Previous work on fluctuation conductivity in the cuprates has focused mainly on dc resistivity vs.

temperature measurements in YBCO crystals,[5,6,7] where the measured data was best fit by the 2D Gaussian fluctuation theory well above $T_c$ and 3D Gaussian theory closer to $T_c$. Recently there have been reported measurements of the zero-field fluctuation conductivity at finite frequency in YBCO, observed in the temperature dependence of the conductivity above $T_c$ at 9.6 GHz on single crystals.[8] These measurements also showed 2D Gaussian fluctuations for $T > T_c$, consistent with the dc measurements.

Critical fluctuation effects can be observed when fluctuations become sufficiently large so that the Gaussian approximation treatment of the Ginzburg-Landau free energy is no longer valid. The critical region is identified experimentally by measuring quantities such as the fluctuation lifetime $\tau^{fl}$ and correlation length $\xi$, which diverge differently than predicted by the Gaussian theory as $T \rightarrow T_c$ within the critical region. Evidence of critical behavior in the cuprate superconductors has been reported in the temperature dependence of the microwave penetration depth of YBCO single crystals as $T_c$ is approached from below.[8,9] Such measurements reveal a surprisingly wide critical region below $T_c$ (~ 5-10 K), which exhibits 3D XY critical behavior. Heat capacity data also show 3D XY behavior [ $-0.03 < (2-dv) < 0$ ] for $T = T_c \pm 10$ K.[10] Above $T_c$ there has been no definitive observation of critical effects in the high $T_c$ materials in zero magnetic field. Efforts to observe critical behavior in temperature-dependent conductivity measurements are hampered by the inability to measure closely enough to $T_c$ and are also often clouded by the question of sample homogeneity. It is therefore very important to explore different experimental degrees of freedom in order to determine if a critical region exists above $T_c$ in the high $T_c$ materials, and if so, what are the critical exponents and scaling functions that describe the approach to the phase transition.

The ability of the Corbino reflection technique to extract the frequency dependence of the conductivity in addition to the temperature dependence at

temperatures through $T_c$ provides additional essential information on the nature of the phase transition at $T_c$. By measuring the frequency dependence of the magnitude and phase of the fluctuation contribution to the conductivity, we can extract a measure of the thermodynamic critical temperature and the dynamical critical exponent z (both of which are difficult to determine using solely the temperature dependence). This fact has been utilized in lower frequency measurements to locate a phase transition from a vortex liquid to a vortex solid in finite fields in YBCO films[11,12,13] and in $Mo_3Si$ films[14], where the characteristic time scales are longer. Our access to the frequency dependence also allows us to directly observe the effect of the finite fluctuation lifetime on the conductivity above $T_c$, and also to determine how that lifetime diverges as $T \rightarrow T_c$ in an effort to identify critical phenomena.

In what follows, we will first describe in section 5.2 the current theoretical understanding of fluctuation effects in superconductors. This will be followed in section 5.3 with a detailed analysis of the temperature dependence of the dc resistivity, with the goal of obtaining a measure of the normal state or mean-field contribution to the experimentally measured conductivity. In section 5.4 the frequency dependence of the complex conductivity in the immediate region of the superconducting phase transition will be analyzed in terms of the fluctuation theories outlined above, and in section 5.5 the temperature dependence of the fluctuation contribution to the conductivity will be explored. Finally in section 5.6 the dependence of the fluctuation effects on sample quality will be addressed by analyzing the fluctuation conductivity of samples of varying quality.

## 5.2 Models of Fluctuations in Superconductors

### 5.2.1 Mean-field Theory: Ginzburg-Landau Theory

This section gives a brief summary of the application of Ginzburg-Landau (GL)

theory to calculate the effect of fluctuations of the order parameter on the conductivity of a superconductor. This section is not meant to be a complete description of Ginzburg-Landau theory; more complete treatments are available from a number of sources.[15,16,17,18] In what follows time independent GL theory will first be briefly described, followed by the generalization of GL theory to include time-dependent effects. Then the expressions for the fluctuation conductivity in three dimensions derived from time-dependent Ginzburg-Landau (TDGL) theory will be presented, followed by the corresponding expressions valid for two dimensions.

Consider GL theory for a spatially uniform order parameter. Spatial uniformity can be assured by considering superconducting particles which have all dimensions smaller than the GL coherence length $\xi(T)$. Then the GL free energy of the superconducting state relative to the normal state can be written as an expansion in the order parameter $\psi$

$$\Delta F = V\left(\alpha|\psi|^2 + \frac{\beta}{2}|\psi|^4\right) \tag{5.1}$$

with $\alpha=\alpha_0\varepsilon$, where $\alpha_0$ and $\beta$ are positive constants which are temperature independent near $T_c$, and V is the volume, and $\varepsilon=\ln(T/T_c) \approx (T-T_c)/T_c$. The function $\Delta F$ is plotted as a function of $|\psi|$ for temperatures above and below $T_c$ in Fig. 5.1.

The most probable value for the order parameter $\psi$ is that which gives a minimum in the free energy. For $T<T_c$, it is clear from Fig. 5.1 that the minimum of $\Delta f$ is obtained for a non-zero value of $|\psi|$. For $T>T_c$, the most probable value for the order parameter is $|\psi| = 0$, however, values of the free energy within $k_BT$ of the minimum value are also likely. This means that due to thermal fluctuations it is possible to have a non-zero value for the order parameter above $T_c$, which implies the existence of evanescent Cooper pairs above $T_c$ with finite probability.

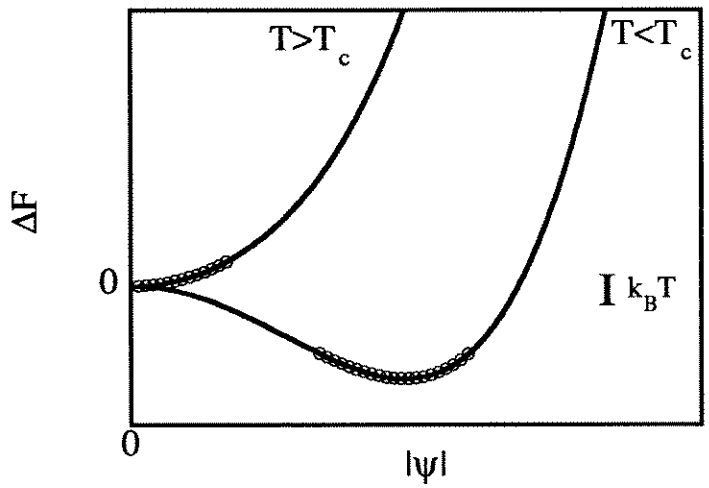


Fig. 5.1. The difference in the free energy of the superconducting state relative to the normal state above and below $T_c$ as a function of order parameter. The circles indicate values of the order parameter that are also probable. After [18].

In order to include spatial variations and magnetic fields the free energy density ($\Delta F = \int f\, dV$) must be modified as follows

$$f = \alpha|\psi|^2 + \frac{\beta}{2}|\psi|^4 + \frac{1}{2m^*}\left|\left(\frac{\hbar}{i}\nabla - e^*\mathbf{A}\right)\psi\right|^2 \tag{5.2}$$

If we can assume that $|\psi|^2$ is small, we can neglect the $\beta|\psi|^4$, and obtain the following expression for the free energy in the Gaussian approximation

$$f = \alpha|\psi|^2 + \frac{1}{2m^*}\left|\left(\frac{\hbar}{i}\nabla - e^*\mathbf{A}\right)\psi\right|^2 \tag{5.3}$$

Expanding $\psi$ in a Fourier series as $\psi(r) = \Sigma_k\, \psi_k \exp(i\mathbf{k}\cdot\mathbf{r})$ gives for the free energy per unit volume with $\mathbf{A}=0$: $f = \Sigma_k\, (\alpha + \hbar^2k^2/2m^*)\, |\psi_k|^2$. It is possible to calculate thermodynamic average quantities by using this form for the free energy functional in the Boltzmann factor and integrating over all possible values of k. The result for the thermodynamic average of $|\psi|^2$ is $\langle|\psi_k|^2\rangle = k_BT/\alpha(1+k^2\xi^2)$, where $\xi$ is the GL coherence length, defined by

$$\xi(T) = \left(\frac{\hbar^2}{2m^*|\alpha|}\right)^{1/2} = \frac{\xi_0}{|\varepsilon|^{1/2}} \tag{5.4}$$

The meaning of $\xi$ physically can be seen by considering the spatial correlation function of the order parameter $g(\mathbf{r},\mathbf{r}')=\langle\psi^*(\mathbf{r})\psi(\mathbf{r}')\rangle$. Writing the relative coordinate $\mathbf{R}=\mathbf{r}-\mathbf{r}'$, valid for a homogeneous system, gives $g(\mathbf{R}) = \sum_k \langle|\psi_k|^2\rangle\exp(i\mathbf{k}\cdot\mathbf{R})$. Converting the sum to an integral and using the above expression for $\langle|\psi_k|^2\rangle$ gives the result

$$g(R) = \frac{m^* k_B T}{2\pi\hbar}\frac{\exp\left(-R/\xi(T)\right)}{R} \tag{5.5}$$

This gives spatial correlations which fall off exponentially over a length scale defined by $\xi(T)$. The quantity $\xi(T)$ therefore gives approximately the spatial extent of the fluctuations.

The functions $\psi(r)$ and $A(r)$ are determined by minimizing the volume integral of the free energy density in (5.3) with respect to $\psi$. In this manner one obtains the time independent GL differential equation

$$\alpha\psi + \beta|\psi|^2\psi + \frac{1}{2m^*}\left(\frac{\hbar}{i}\nabla - e^*A\right)^2\psi = 0 \tag{5.6}$$

By minimizing the free energy with respect to the vector potential A one obtains the following equation for the current density J

$$J = \frac{e^*}{m^*}\,\mathrm{Re}\left\{\psi^*\left(\frac{\hbar}{i}\nabla - e^*A\right)\psi\right\} \tag{5.7}$$

In order to calculate the effect of fluctuations of the order parameter on the conductivity, it is necessary to include a time dependence in the Ginzburg-Landau free energy, since the excess conductivity due to fluctuations will be directly proportional to the lifetime of the fluctuations. The simplest time dependent generalization of (5.6), neglecting electromagnetic potentials, is given by

$$\alpha\psi + \beta|\psi|^2\psi - \frac{\hbar^2}{2m^*}\nabla^2\psi = -\gamma\hbar\frac{\partial}{\partial t}\psi \tag{5.8}$$

The linearized TDGL equation is then obtained by neglecting the non-linear term $\beta|\psi|^2\psi$, and is given by

$$\frac{\partial\psi}{\partial t} = -\frac{1}{\tau}\left(1-\xi^2\nabla^2\right)\psi \tag{5.9}$$

The temperature-dependent relaxation time of the k=0 mode is given by

$$\tau_{GL} = \frac{\hbar\gamma}{\alpha} = \frac{\tau_0}{|\varepsilon|} \tag{5.10}$$

The above formalism can be used to calculate the contribution to the conductivity of superconducting fluctuations. Such a calculation has been carried out by Schmidt,[19] and later by Dorsey[20]. The results for the fluctuation conductivity ($\sigma = \sigma_1 - i\sigma_2$) depend upon the dimensionality of the system, and are given in three dimensions by

$$\begin{aligned}\sigma_1^{3D} &= \sigma_{DC}^{3D}\cdot F_1^{\pm}(\omega\tau)\\ \sigma_2^{3D} &= \sigma_{DC}^{3D}\cdot F_2^{\pm}(\omega\tau)\end{aligned} \tag{5.11}$$

Here $F_1^{\pm}(\omega\tau)$ and $F_2^{\pm}(\omega\tau)$ describe the frequency dependence above (+) and below(-) $T_c$, and $\sigma_{DC}$ is the dc fluctuation conductivity given by

$$\sigma_{DC}^{3D} = \frac{e^2}{32\hbar\xi_0\,\varepsilon^{1/2}} \tag{5.12}$$

where once again $\varepsilon=\ln(T/T_c)$. The expression for the dc fluctuation conductivity was first worked out by Aslamazov and Larkin.[21] In three dimensions, the frequency dependent functions $F^+$ are given for $T > T_c$ by

$$\begin{aligned}F_1^{+}(\omega\tau) &= \frac{8}{3(\omega\tau)^2}\left[1-\left(1+(\omega\tau)^2\right)^{3/4}\cdot\cos\left(\frac{3}{2}\tan^{-1}(\omega\tau)\right)\right]\\ F_2^{+}(\omega\tau) &= \frac{8}{3(\omega\tau)^2}\left[-\frac{3}{2}\omega\tau+\left(1+(\omega\tau)^2\right)^{3/4}\cdot\sin\left(\frac{3}{2}\tan^{-1}(\omega\tau)\right)\right]\end{aligned} \tag{5.13}$$

The functions $F^-$ for $T < T_c$ are given below for reference, also in three dimensions

$$F_1^-(\omega\tau) = \frac{8}{3(1+(\omega\tau)^2)}\left[\sqrt{2} - (1+(\omega\tau)^2)^{-1/4}\cdot\left\{(1-(\omega\tau)^2)\cdot X + 2\omega\tau Y\right\}\right]$$
$$F_2^-(\omega\tau) = \frac{8\,\omega\tau}{3(1+(\omega\tau)^2)}\left[-\sqrt{2} + 2(1+(\omega\tau)^2)^{-1/4}\cdot\left\{X - \frac{(1-(\omega\tau)^2)}{2\omega\tau}\cdot Y\right\}\right] \qquad (5.14)$$

where $X=\cos[(1/2)\cdot\tan^{-1}(\omega\tau)]$, and $Y=\sin[(1/2)\cdot\tan^{-1}(\omega\tau)]$. The fluctuation relaxation time $\tau$ is given by

$$\tau = \frac{\pi\hbar}{16 k_B T_c\,\varepsilon} \qquad (5.15)$$

In two dimensions the results for the fluctuation conductivity are given by the following

$$\sigma_1^{2D} = \sigma_{DC}^{2D}\cdot G_1^{\pm}(\omega\tau)$$
$$\sigma_2^{2D} = \sigma_{DC}^{2D}\cdot G_2^{\pm}(\omega\tau) \qquad (5.16)$$

Corrections 1/21/00

where once again the functions $G^{\pm}(\omega\tau)$ describe the frequency dependence, and the two-dimensional dc fluctuation conductivity is given by

$$\sigma_{DC}^{2D} = \frac{e^2}{16\hbar d\,\varepsilon} \qquad (5.17)$$

Here d is the film thickness. The frequency dependent functions $G^+$ for $T > T_c$ in two dimensions are

$$G_1^+(\omega\tau) = \frac{1}{\omega\tau}\left[\pi - 2\tan^{-1}\left(\frac{1}{\omega\tau}\right) - \frac{1}{\omega\tau}\cdot\ln\left(1+(\omega\tau)^2\right)\right]$$
$$G_2^+(\omega\tau) = \frac{1}{\omega\tau}\left[-2 + \frac{\pi}{\omega\tau} - \frac{2}{\omega\tau}\tan^{-1}\left(\frac{1}{\omega\tau}\right) + \ln\left(1+(\omega\tau)^2\right)\right] \qquad (5.18)$$

while the corresponding expressions for $T < T_c$ are

$$G_1^-(\omega\tau) = \frac{\omega\tau}{(1-\omega\tau)}\left[\pi - 2\tan^{-1}\left(\frac{1}{\omega\tau}\right) - \frac{1}{\omega\tau}\cdot\ln\left(\frac{1+(\omega\tau)^2}{4}\right)\right]$$
$$G_2^-(\omega\tau) = \frac{1}{(1-\omega\tau)}\left[\pi - 2\tan^{-1}\left(\frac{1}{\omega\tau}\right) + \omega\tau\cdot\ln\left(\frac{1+(\omega\tau)^2}{4}\right)\right] \qquad (5.19)$$

$1+(\omega\tau)^2$

The fluctuation relaxation time $\tau$ is the same in two dimensions, given in Eq. 5.15.

### 5.2.2 Scaling Theories

The above treatment of the fluctuation conductivity is valid as long as the order parameter is small enough so that the non-linear terms in Eq. 5.8 can be safely neglected. Under circumstances where the non-linear terms are important, such an expansion of the free energy is no longer valid and other approaches must be adopted. In this section a more general scaling theory will be described, which utilizes dimensional arguments to obtain a form for the conductivity that is valid even when the fluctuations are large.

The general scaling theory for the conductivity[1,20] starts with the assumption that the correlation length $\xi$ diverges as $T \rightarrow T_c$ ($\varepsilon \rightarrow 0$) as

$$\xi(T) = \frac{\xi_0}{\varepsilon^{\nu}} \tag{5.20}$$

where the exponent $\nu$ can take on any value, and is not restricted to be $\nu=1/2$ as in the Gaussian theory (see Eq. 5.4). To describe the behavior of the conductivity, the theory also assumes a fluctuation relaxation time $\tau$ that diverges as $\varepsilon \rightarrow 0$ as $\tau \sim \xi^z$, where z is the dynamical critical exponent. Utilizing the temperature dependence of $\xi$ in Eq. 5.20 gives the temperature dependence of $\tau$ as

$$\tau(T) = \frac{\tau_0}{\varepsilon^{\nu z}} \tag{5.21}$$

Once again, z can take on any arbitrary value and is not limited to the Gaussian value of $z=2$ (which gives $\tau \sim 1/\varepsilon$, see Eq. 5.15).

The form of the fluctuation conductivity at finite frequencies can be determined by dimensional arguments and the requirement that the conductivity remain finite as $T \rightarrow T_c$. This requires that near $T_c$ the finite frequency conductivity scale with the correlation length as

$$\sigma(T,\omega) \approx \xi^{2-D+z}\, S_{\pm}(\omega\tau) \tag{5.22}$$

where D is the dimensionality, z is the dynamical critical exponent, and $S_{\pm}(x)$ are temperature-independent scaling functions above (+) and below (-) $T_c$. The quantity $\tau$ is the fluctuation relaxation time defined above (Eq. 5.21). If we write the conductivity as $\sigma=|\sigma|\exp(i\phi_\sigma)$ then the phase of the conductivity should also scale near the phase transition as

$$\phi_\sigma(T,\omega) = \Phi_{\pm}(\omega\tau) \tag{5.23}$$

where once again $\Phi_{\pm}(x)$ are temperature-independent scaling functions.

The scaling functions $S_{\pm}$ and $\Phi_{\pm}$ take on simple limiting forms when $T=T_c$. Given the fact that relaxation time diverges as $\tau \approx \xi^z$, in order that the conductivity remain finite as the $\xi$ diverges, the magnitude of the conductivity must scale with frequency at $T_c$ as

$$|\sigma(T=T_c)| = c|\omega|^{-(2-D+z)/z} \tag{5.24}$$

At $T=T_c$ the phase of the conductivity is a constant independent of frequency that depends only on the dimensionality of the system D and the dynamical critical exponent z

$$\phi_\sigma(T=T_c) = \frac{\pi}{2}\left[\frac{2-D+z}{z}\right] \tag{5.25}$$

## 5.3 Normal State Behavior: Temperature Dependence of the dc Resistivity

In order to look for fluctuation effects in our YBCO films, we first examine the temperature dependence of the dc resistivity, which is measured in a separate experiment over the entire temperature range from room temperature down to $T_c$, and is shown for sample #NCL705b in Fig. 5.2. The dc resistivity is measured after the gold Corbino contacts are evaporated onto the film, in a three-point configuration, with two contacts on the outer circular contact and one on the inner conductor contact pad (as

shown in Fig. 2.5). Figure 5.3 shows the numerical derivative dρ/dT versus temperature of the same experimental data. Note from the dρ/dT plot that the slope is approximately constant for most of the temperature range from room temperature down to within about 10-20K of $T_c$, at which point the slope begins to increase, indicative of enhanced conductivity as $T_c$ is approached.

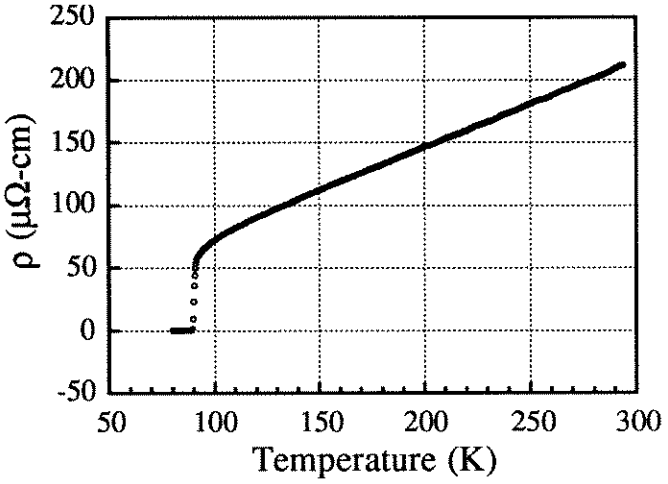


Fig. 5.2. The temperature dependence of the dc resistivity for sample NCL705b.

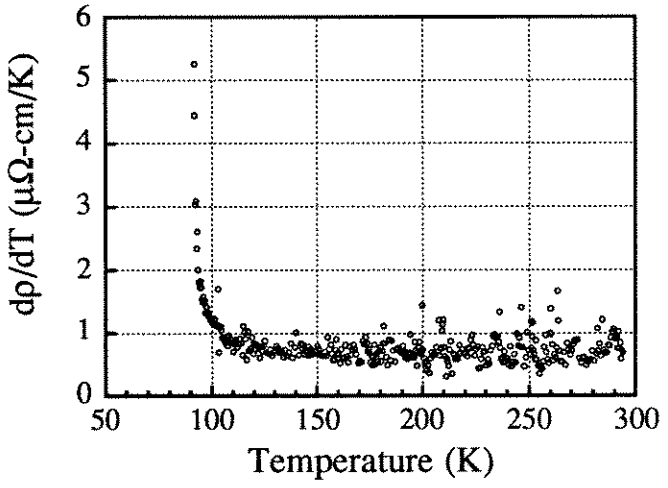


Fig. 5.3. The numerical derivative dρ/dT for the resistivity data in figure 5.2.

The dc resistivity vs. temperature data is relevant to the high frequency measurements presented here for two reasons. First, the behavior of the temperature dependent dc resistivity can be compared directly with the results of other dc resistivity

experiments that show evidence of fluctuation effects. Perhaps more importantly for the finite frequency experiments presented later in this chapter is the fact that an accurate value for the mean-field (or normal state) resistivity can be extracted from these dc measurements. This can be accomplished because the total conductivity can be assumed to be composed of the sum of a mean-field contribution and a fluctuation contribution: $\sigma^{tot}(T,\omega) = \sigma^{mf}(T) + \sigma^{fl}(T,\omega)$, where the mean-field term corresponds to a resistivity that is linear in temperature and frequency independent: $\sigma^{mf}(T) = 1/(r_0+r_1 \cdot T)$. Then by fitting the temperature dependence of the dc resistivity (shown in Fig. 5.2, for example), with an appropriate model for $\sigma^{fl}(T,\omega=0)$, the function $\sigma^{mf}(T)$ can be determined. This mean field contribution is then subtracted from the total conductivity measured at finite frequency to obtain the finite frequency fluctuation conductivity.

The temperature dependence of the dc fluctuation contribution to the conductivity depends on the dimensionality of the system, and is given for three dimensions by Eq. 5.12 and for two dimensions by Eq. 5.17. Because of the layered nature and strong anisotropy of the high $T_c$ superconductors, it is not clear if one should use the three dimensional isotropic form for the fluctuation conductivity, or the two dimensional form with the film thickness given by the copper-oxide layer separation. In order to take into account the anisotropic nature of the cuprates, Lawrence and Doniach[22] created a model for the fluctuation conductivity which essentially interpolates between the 2D and the 3D forms above, and is given by

$$\sigma_{LD}^{fl} = \frac{e^2}{16\hbar d\,\varepsilon} \frac{1}{\left[1 + \frac{1}{\varepsilon}\left(\frac{2\xi_c(0)}{d}\right)^2\right]^{1/2}} \tag{5.26}$$

where here $\xi_c(0)$ is the c-axis correlation length at zero temperature, and d is the inter-layer separation. As can be seen from Eq. 5.26, when the c-axis correlation length is

much less than the inter-layer spacing ($\xi_c(0) << d$), the fluctuation conductivity reduces to the 2D Gaussian expression (Eq. 5.17), while in the opposite limit, when $\xi_c(0) >> d$, Eq. 5.26 reduces to the 3-dimensional form (Eq. 5.12).

With the above forms (2D, 3D, Lawrence-Doniach) for the temperature dependence of $\sigma^{fl}(T,\omega=0)$, the measured dc resistance can be fit to the 2D and 3D Gaussian fluctuation models, as well as to the Lawrence-Doniach model. For the pure Gaussian models, 4 variable parameters are used: $r_0$, $r_1$, $T_c$, and either d or $\xi_0$ (depending on the dimensionality), while for the Lawrence-Doniach model 5 parameters are used: $r_0$, $r_1$, $T_c$, d, and $\xi_c(0)$. We also attempt to fit the data without any fluctuation effects ($\sigma^{fl}=0$), using only 3 parameters: $r_0$, $r_1$, and $T_c$. The results of these fits are given for sample NCL705b in table 5.1. As might be expected, the Lawrence-Doniach model fits the data the best, and this fit is shown along with the data, and also the fit using only the mean-field contribution ($\sigma^{fl}=0$), in Figs. 5.4 and 5.5. The parameters extracted from the Lawrence-Doniach fit seem to be physically reasonable, with an inter-layer separation of d=10.0 Å, and a c-axis coherence length of $\xi_0$ = 0.91 Å. These parameters give 2D fluctuations in the region far above $T_c$, which cross over to 3D fluctuations near $T_c$. The cross-over from 2D to 3D fluctuations occurs when the temperature-dependent correlation length becomes comparable to half the inter-layer spacing ($\xi_c(0)/\sqrt{\varepsilon} \approx d/2$), which occurs at T = 90.58 K for these fit parameters. These parameters seem to be in reasonable agreement with previous temperature-dependent measurements of the dc conductivity of YBCO crystals[5,6,7]. In addition, the values for $r_0$ and $r_1$ for the 2D Gaussian, 3D Gaussian, and mean-field fits give values for the mean field resistivity at temperatures near $T_c$ that differ from the Lawrence-Doniach value by at most 5%.

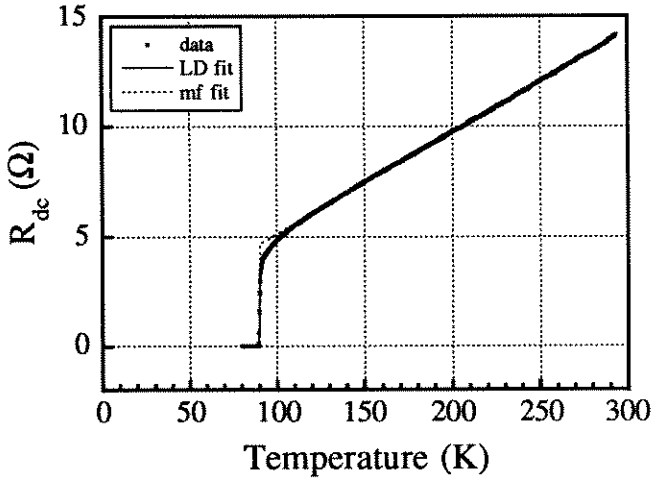


Fig. 5.4. Fits to the dc sheet resistance vs. temperature using both the Lawrence-Doniach model of the fluctuation conductivity (solid line), and using just the mean-field conductivity (dashed line).

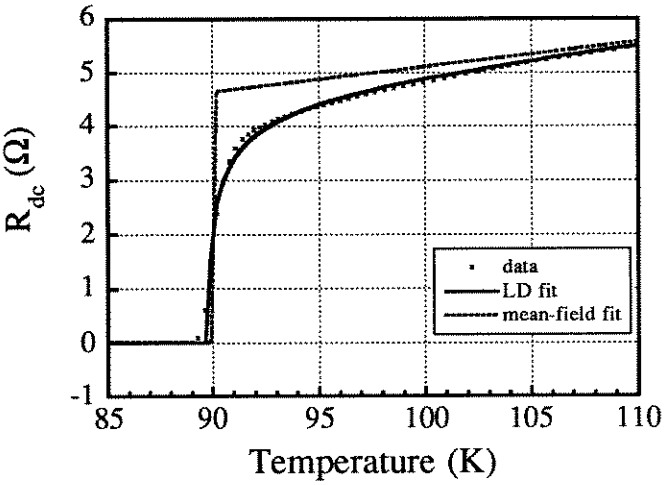


Fig. 5.5. The Lawrence-Doniach (solid line) and mean-field only (dashed line) fits to the dc sheet resistance near $T_c$.

Table 5.1. Parameters for fits to the dc resistance vs. temperature data for sample #NCL705b. The fit quality is in Ω/degree of freedom, and is a minimum for the best fit.

| fit | $r_0$(μΩ-cm) | $r_1$(μΩ-cm) | $T_c$(K) | $\xi_0$(Å) | d(Å) | fit qual. ($\chi^2$) |
|---|---|---|---|---|---|---|
| mf | 7.159 | 0.694 | 90.00 | – | – | 0.076 |
| 2D | 9.649 | 0.699 | 89.52 | – | 13.0 | 0.024 |
| 3D | 4.726 | 0.793 | 89.87 | 1.23 | – | 0.034 |
| LD | 10.490 | 0.700 | 89.83 | 0.91 | 10.0 | 0.023 |

## 5.4 The Complex Resistivity Near $T_c$ in YBCO Films

The main advantage of the Corbino reflection technique is the ability to measure the complex resistivity $\rho^* = \rho_1 + i\rho_2$ over a wide range of frequencies in the microwave range. Figure 5.6 shows the temperature dependence of $\rho_1$ at a number of different measurement frequencies for a typical YBCO thin film. Also shown in Fig. 5.6 is the dc resistivity measured as described above in section 5.3. The main feature of the temperature dependent data is the fact that the transition appears to broaden considerable as the measurement frequency increases. In the normal state, the data at different frequencies (including dc) all describe the same curve, because the normal state scattering rate ($1/\tau_n$) is much greater than the measurement frequency over the entire measurement range.

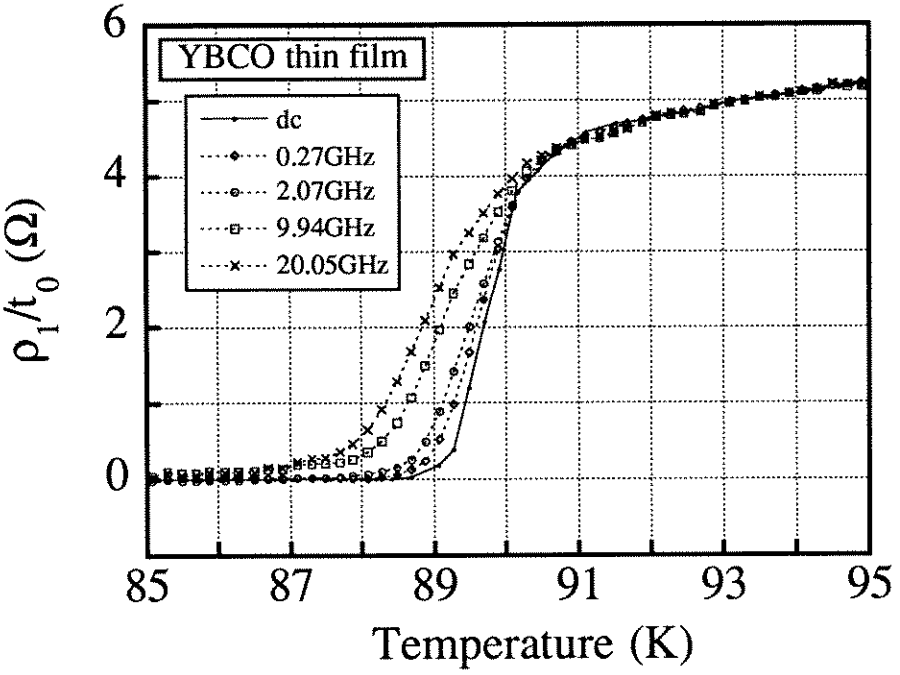


Fig. 5.6. The temperature dependence of $\rho_1/t_0$ at several different frequencies near the superconducting phase transition.

The temperature dependence of $\rho_2/t_0$ is shown in Fig. 5.7 at the same measurement frequencies as Fig. 5.6. In the region below $T_c$, $\rho_2/t_0$ increases as the

measurement frequency increases, and the temperature at which the peak in $\rho_2/t_0$ occurs moves systematically lower for higher frequencies. Also of note is the fact that $\rho_2/t_0=0$ for all frequencies in the normal state, consistent with a normal state resistivity that is completely real.

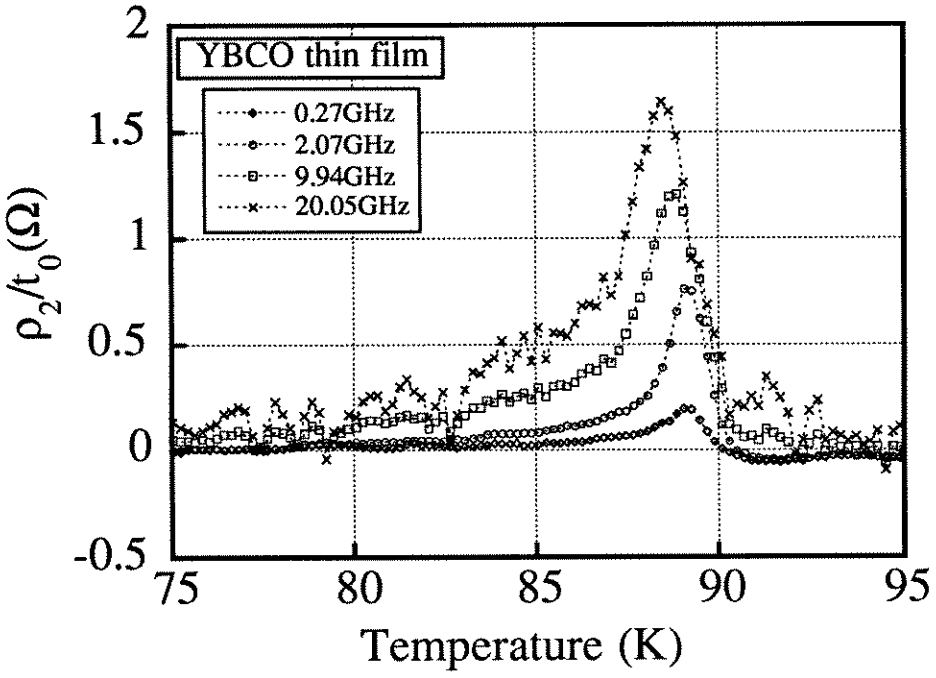


Fig. 5.7. The temperature dependence of $\rho_2/t_0$ at several different frequencies.

Because the Corbino reflection technique is a swept-frequency measurement, it is possible to directly measure the frequency dependence that is apparent in Figs. 5.6 and 5.7. Figures 5.8 and 5.9 display the frequency dependence of the same sample at several different temperatures in the transition region. Above $T_c$ $\rho_1/t_0$ is roughly frequency independent, and $\rho_2/t_0$ is roughly zero, as pointed out in the temperature dependence above. In the midst of transition region both $\rho_1/t_0$ and $\rho_2/t_0$ show considerable frequency dependence. At temperatures well below $T_c$ the $\rho_1/t_0$ is small, and $\rho_2/t_0$ is approximately linear in frequency, since $\rho_2/t_0 \approx \mu_0\omega\lambda^2(T)/t_0$ for $T<T_c$.

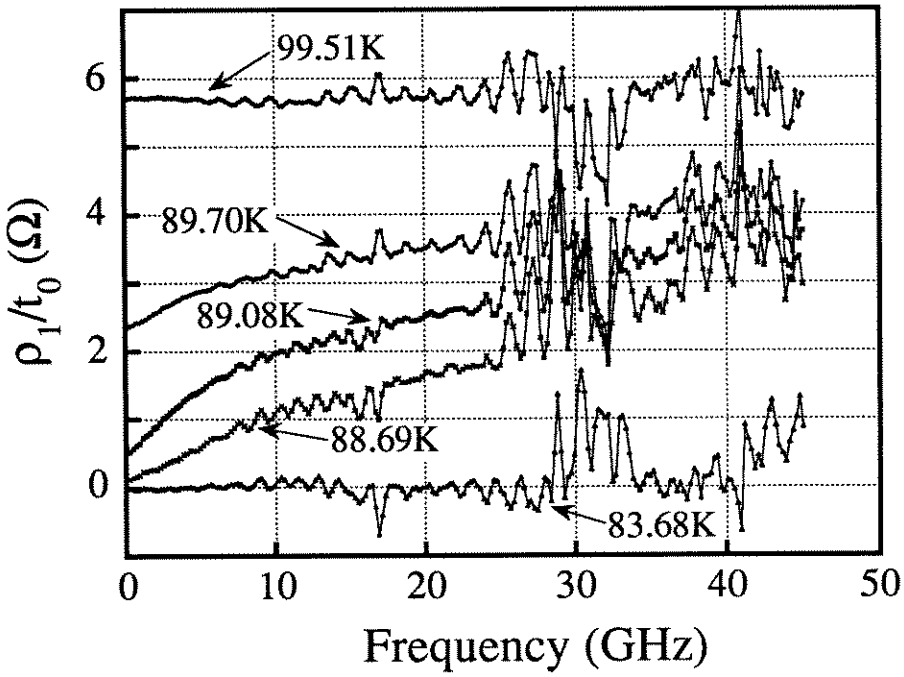


Fig. 5.8. The frequency dependence of $\rho_1/t_0$ at temperatures in the vicinity of $T_c$.

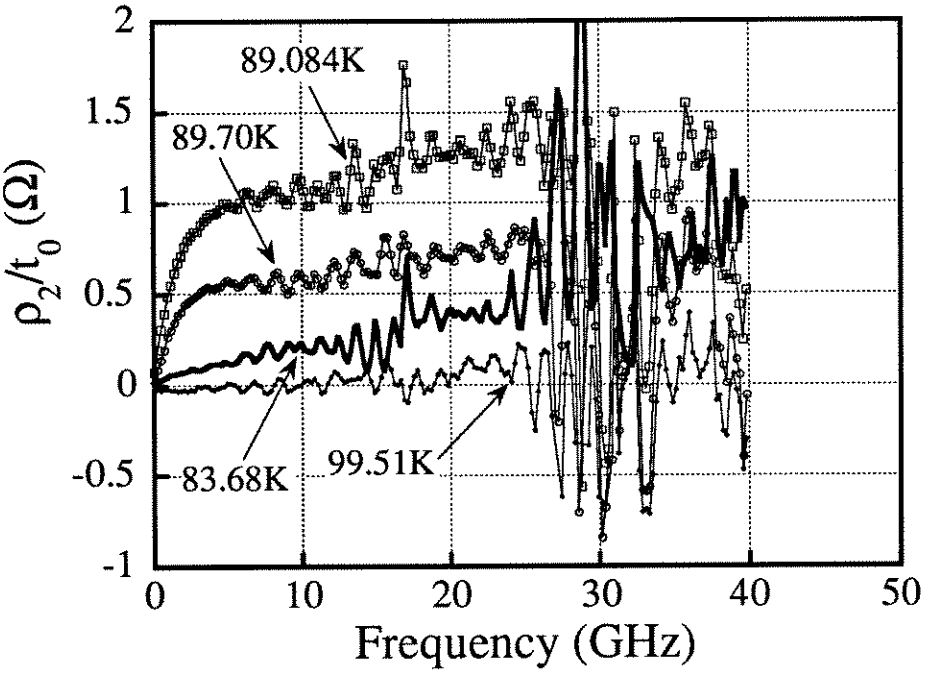


Fig. 5.9. The frequency dependence of $\rho_2/t_0$ at temperatures in the vicinity of $T_c$.

## 5.5 Fluctuation Effects in the Frequency Dependent Conductivity

In order to analyze the frequency dependent data, it is convenient to convert the measured complex resistivity to a conductivity. It is then simple to remove the mean-field contribution as determined from the dc resistivity fits in order to investigate the frequency dependence of the fluctuation conductivity alone.

### 5.5.1 Frequency Dependence at $T=T_c$

The frequency dependence of the fluctuation conductivity magnitude ($|\sigma|=[\sigma_1^2 + \sigma_2^2]^{1/2}$) and phase ($\phi_\sigma=\tan^{-1}[\sigma_2/\sigma_1]$) in the vicinity of the superconducting phase transition are quantities of considerable interest. According to general scaling theory discussed above,[1,20] the phase angle of the fluctuation conductivity should take on a frequency-independent value at the critical temperature $T_c$ that depends only on the dimensionality D of the system and the dynamical critical exponent z (see Eq. 5.25): $\phi_\sigma(T=T_c) =(\pi/2)\cdot(2-D+z)/z$. The corresponding behavior of the magnitude of the fluctuation conductivity is a power-law frequency dependence at $T=T_c$ (see Eq. 5.24): $|\sigma^{fl}(T=T_c)| \sim |\omega|^\alpha$, with $\alpha=(2-D+z)/z$. The frequency dependence of the magnitude and phase of the fluctuation conductivity can therefore be examined to locate the critical temperature, and to obtain a value for the dynamical critical exponent z assuming D is known.

The measured frequency dependence of the magnitude and phase of the fluctuation conductivity is shown in Figs. 5.10 and 5.11 respectively at temperatures in the vicinity of $T_c$. The fluctuation conductivity is extracted from the total measured conductivity by subtracting off the frequency-independent value for the mean-field conductivity. It should be noted that using a different value for $\sigma^{mf}(T)$ within the range given in table 5.1 (roughly ±5%) does not affect the results. To determine the critical isotherm we fit the frequency dependence of the magnitude of the fluctuation

conductivity in Fig. 5.10 to a power law as prescribed by Eq. 5.24, and obtain the best fit for the data at T=89.18 K, where $|\sigma(\omega)| \sim \omega^{-0.62\pm0.02}$. Examination of Fig. 5.11 shows that the fluctuation conductivity phase angle takes on a roughly constant value also for the T=89.18 K data set, with a mean value of $\phi_\sigma = 0.64 \cdot (\pi/2)$ and a standard deviation of $0.12 \cdot (\pi/2)$. Note that for temperatures above (below) 89.18 K, the phase is an increasing (decreasing) function of frequency. The frequency dependence at T = 89.18 K shows that the value of the power law of the fluctuation conductivity magnitude and the value of the (constant) reduced phase angle are the same (within experimental error), in agreement with the prediction of the scaling theory (Eqs. 5.24 and 5.25).

The values of the phase angle and the magnitude power law determine the value of the dynamical critical exponent z. However, since the data sets are taken at 0.2 K intervals, there exists some uncertainty in the exact determination of $T_c$ from the frequency dependence of the conductivity. This uncertainty is estimated to be roughly half the separation in temperature between the data sets, which is 0.1 K. Due to this uncertainty in $T_c$ there also exists a corresponding uncertainty in the determination of the critical phase angle and power law values. We can therefore conclude from the behavior of the frequency dependent fluctuation conductivity that the thermodynamic critical temperature for this sample is $T_c = 89.18 \pm 0.1$ K and the value of the dynamical critical exponent (with the assumption that D=3) is in the range z = 2.35-2.95. Other samples give values for z as high as z=3. In all cases our results for the value of the dynamical critical exponent are significantly larger than the Gaussian prediction of z=2. Since the fluctuation relaxation time $\tau^{fl}$ diverges as $\tau \sim \xi^z$, the fact that $z > 2$ suggests critical behavior in our samples. Determination of the dynamical critical exponent z from non-linear dc resistivity measurements give widely varying results, from z=2.2±0.4[23] up to z=8.3±0.3.[24]

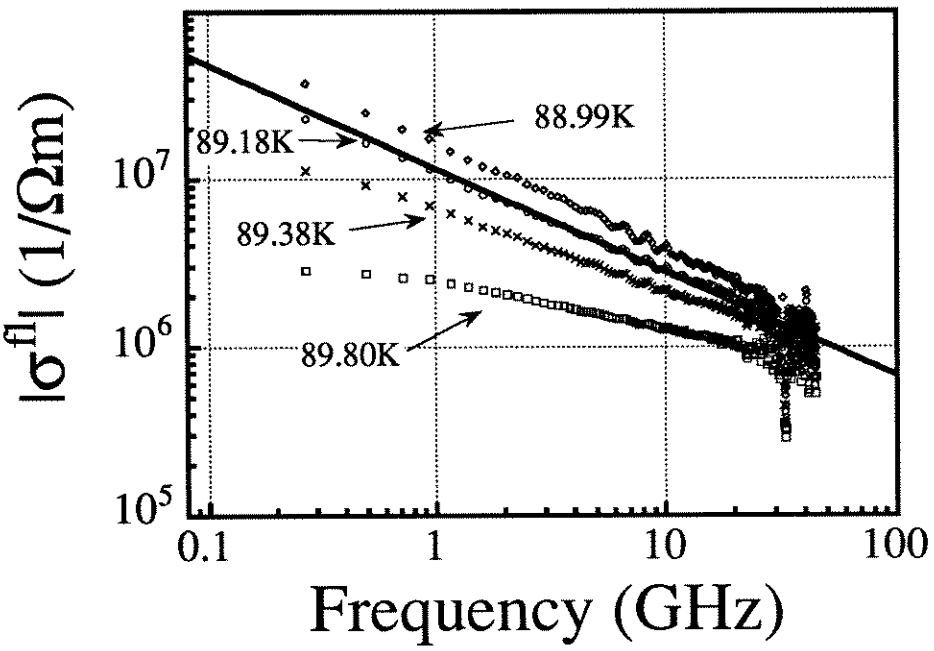


Fig. 5.10. Magnitude of the fluctuation conductivity in the vicinity of $T_c$. The solid line is a power law fit to the T=89.18K with a power of -0.62.

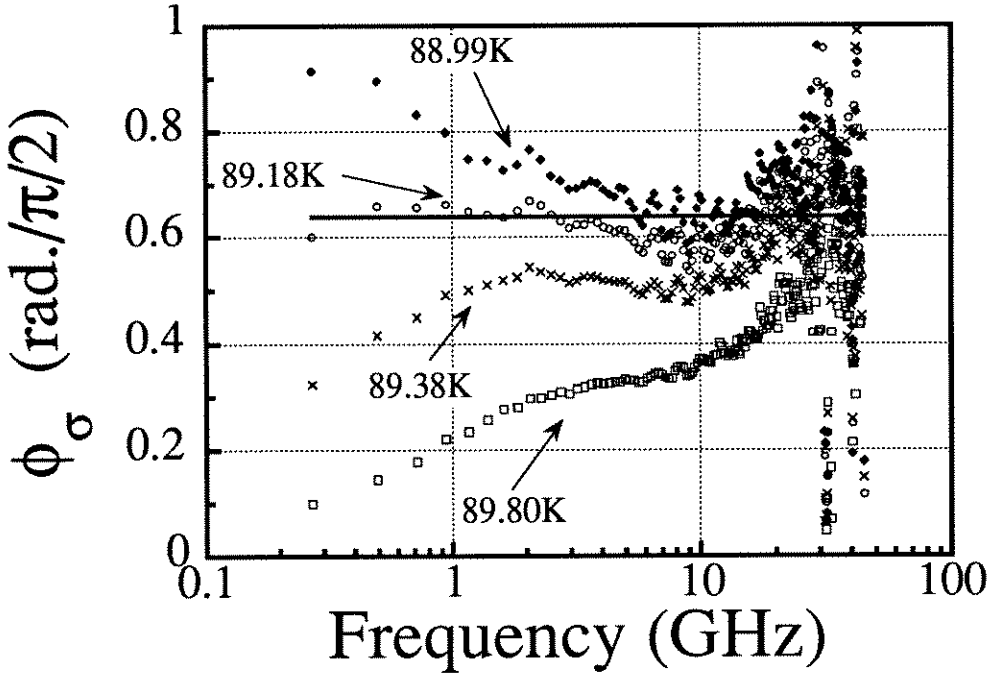


Fig. 5.11. Reduced phase of the fluctuation conductivity in the vicinity of $T_c$. The solid line is a constant value of 0.64.

### 5.5.2 Scaling of the Frequency-dependent Conductivity above $T_c$

The results obtained in section 5.5.1 for the dynamical critical exponent at $T_c$ suggest that we look for scaling behavior in the frequency-dependent fluctuation conductivity at temperatures above $T_c$. From scaling theory it is expected that in the vicinity of a phase transition, the fluctuation conductivity should scale with the appropriate power of the (temperature-dependent) correlation length $\xi$ and the fluctuation lifetime $\tau^{fl}$, as shown in Eq. 5.22. The function $S_+$ ($S_-$) in Eq. 5.22 is the universal scaling function above (below) $T_c$, which should be the same for all members of a given universality class, as should be the critical exponents $\nu$ and z. With the assumption that D=3, Eq. 5.22 implies that the quantity $\sigma/\varepsilon^{-\nu(z-1)}$ plotted vs. the scaled frequency $\omega\varepsilon^{-\nu z}$ should yield the universal scaling function $S_{\pm}$. We can determine if our measured data obeys Eq. 5.22 by plotting the scaled conductivities, measured at different temperatures, vs. the scaled frequency and varying the parameters $\nu$, z, and $T_c$ until the different data sets all collapse onto the same universal curve. We have determined already from the behavior of the critical isotherm (section 5.5.1) that $T_c = 89.18 \pm 0.1$ K and $z \approx 2.6$, leaving just the value of $\nu$ which can be adjusted to collapse the data.

Figure 5.12 shows conductivity data from 5 different temperatures which collapses onto a single curve when scaled as described above with $T_c = 89.10$, z=2.6, and $\nu$=1.2. In the inset to Fig. 5.12 we have plotted the magnitude of the scaling function for D=3 in the Gaussian theory, which was first derived by Schmidt.[19] The two functions are qualitatively similar, however the scaling function that describes the data approaches a power law of -0.62 at large argument, while the 3D Gaussian scaling function approaches a power law of -0.50. The scaling behavior is relatively insensitive to the ultimate choice of $T_c$ (within the above quoted error), although the value of $\nu$ varies in the range ($1.0 < \nu < 1.2$) as a result of the specific choice of $T_c$. If

the value of ν is fixed at ν = 2/3 (which is the prediction of the 3D XY model), then the data does show scaling behavior if the value of z is increased to approximately z= 3.5. Such a large value of z is inconsistent, however, with the conclusions of section 5.5.1.

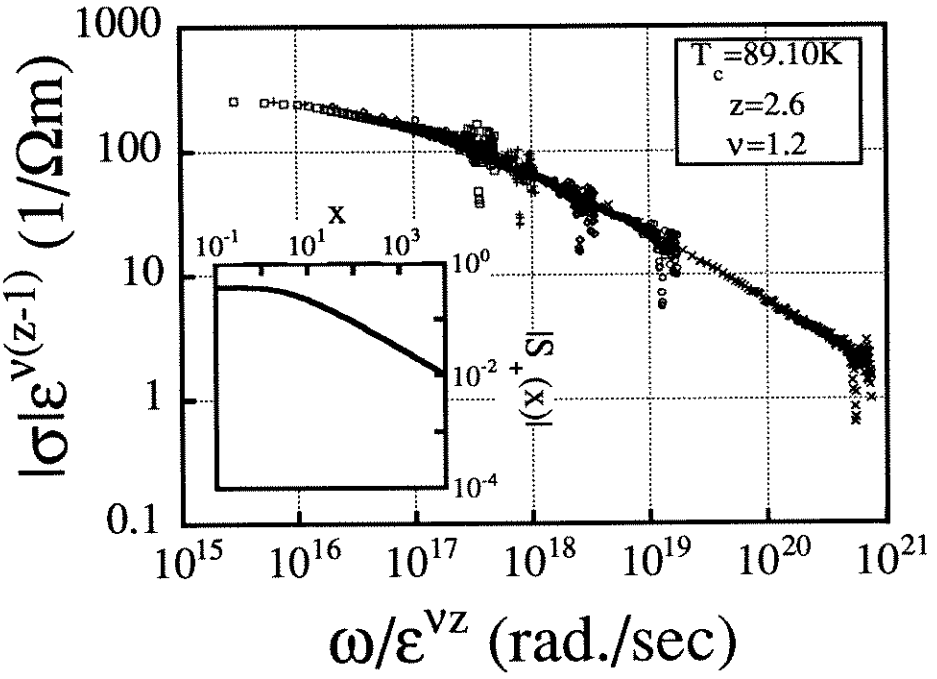


Fig. 5.12. Scaling behavior of the magnitude of the fluctuation conductivity. The data sets shown are 89.18 K (x's), 89.38K (circles), 89.58K (diamonds), 89.80K (+'s), and 90.00K (squares).

While the magnitude of the fluctuation conductivity obeys the scaling relation given by Eq. 5.22, the phase of the fluctuation conductivity scales with the relation given by Eq. 5.23. When we plot our (unscaled) measured conductivity phase angles vs. the scaled frequency, **with the same values for ν, z, and $T_c$ that we used to scale the magnitude of the conductivity**, we obtain the results shown in Fig. 5.13. Although the phase data shows more uncertainty than the magnitude data, it confirms the scaling behavior seen in the conductivity magnitude data. We have also plotted the 3D Gaussian scaling function for the conductivity phase angle in the inset to Fig. 5.13, which shows a similar functional dependence to our data, but reaches a

maximum value of 0.5 for large argument, whereas the function that describes our data approaches roughly 0.64.

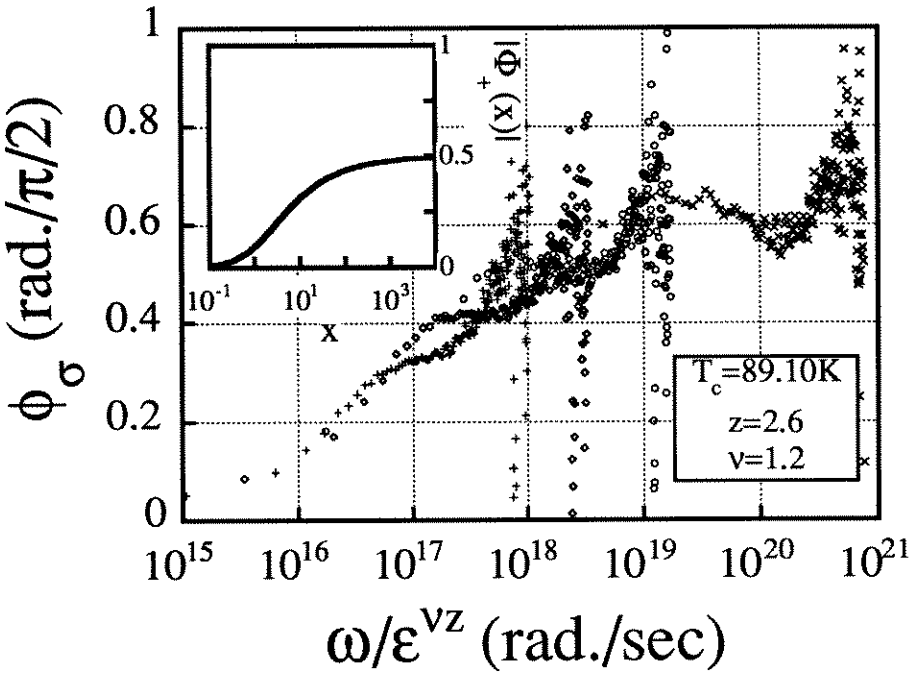


Fig. 5.13. Scaling of the fluctuation conductivity phase. The data sets shown are 89.18 K (x's), 89.38K (circles), 89.58K (diamonds), and 89.80K (+'s).

We conclude from the frequency dependent data that both the magnitude and phase of our measured fluctuation conductivities show scaling behavior with ~ 1 K of $T_c$ with the same values for the critical exponents $\nu \approx 1.0-1.2$ and $z \approx 2.35-2.95$. In spite of the uncertainty in the exact values of the critical exponents $\nu$ and z, these results mean physically that the fluctuation lifetime diverges as $T \rightarrow T_c$ from above roughly as $\tau^{fl} \sim 1/\varepsilon^{\nu z} \approx 1/\varepsilon^3$, which is significantly faster than the Gaussian prediction of $\tau^{fl} \sim 1/\varepsilon$. Our measurements therefore represent a direct observation of the critical slowing down of the fluctuation relaxation rate $1/\tau^{fl}$ as $T \rightarrow T_c$ from above.

## 5.6. Temperature Dependence of the Fluctuation Conductivity

In order to view our fluctuation conductivity data from a different perspective,

we plot in figure 5.14 the temperature dependence of the fluctuation conductivity at several fixed frequencies. The value of $T_c$ used to calculate $\varepsilon$ is $T_c$=89.10 K, as determined from the critical scaling above, and the mean field contribution $\sigma^{mf}(T)$ has been subtracted off. This figure illustrates the effect of the fluctuation relaxation rate $1/\tau^{fl}$ passing through the measurement frequencies. At dc, the fluctuation conductivity diverges as $\varepsilon \rightarrow 0$. At finite frequency the existence of a finite fluctuation lifetime means that the fluctuation conductivity divergence will be cut off when $\omega \sim 1/\tau^{fl}$. The points indicated by arrows indicate the estimated temperature at which $\omega\tau_{fl} \sim 1$ for measurement frequencies of 10 GHz, 2 GHz, and 0.5 GHz. If the conductivity obeyed the Gaussian theory, all the curves would remain together until $\varepsilon \sim 1 \times 10^{-3}$ for

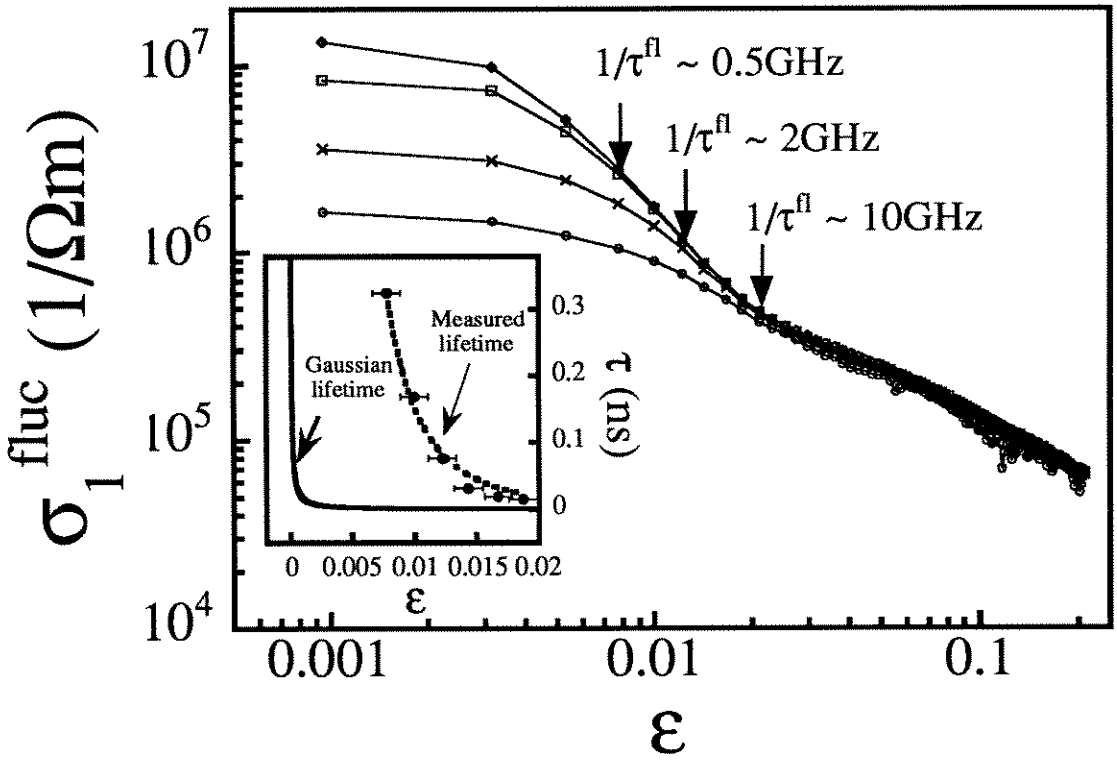


Fig. 5.14 The fluctuation conductivity $\sigma_1$ vs. $\varepsilon$=ln(T/Tc), at 10 GHz (circles), 2 GHz (x's), 0.5 GHz (squares), and 0.27 GHz (diamonds). The arrows indicate approximately where $1/\tau^{fl}$ is equal to the measurement frequency. The inset shows the temperature dependence of $\tau^{fl}$ derived in this manner, along with the temperature dependence of $\tau^{fl}$ in the Gaussian theory.

the measurement frequencies in Fig. 5.14. In the inset to Fig. 5.14 we plot the $\varepsilon$ dependence of $\tau^{fl}$ derived as described above, along with the strict Gaussian calculation of $\tau^{fl}$ (~$1/\varepsilon$), Eq. 5.15. The dashed line is a power law fit to $\tau^{fl} \sim 1/\varepsilon^3$, which is consistent with the $\varepsilon$ dependence of $\tau^{fl}$ determined from the frequency dependence ($\tau^{fl} \sim 1/\varepsilon^{\nu z} \approx 1/\varepsilon^{3.1}$), within experimental error. Figure 5.15 represents further evidence that the fluctuation lifetime diverges much faster than the Gaussian prediction as $\varepsilon \rightarrow 0$.

Using the critical exponents for this sample determined from the frequency dependence analysis, we should also be able to scale the temperature dependence of $\sigma_1$ in Fig. 5.13 according to the scaling relation in Eq. 5.22, so that the data within the critical region will collapse together. This is just what we observe in Fig. 5.15, where the scaled temperature dependence measured at three discrete frequencies is plotted along with the scaled frequency dependence of $\sigma_1$ measured at 6 different temperatures, all with the same values of $T_c$, $\nu$, and z. This figure shows dramatically

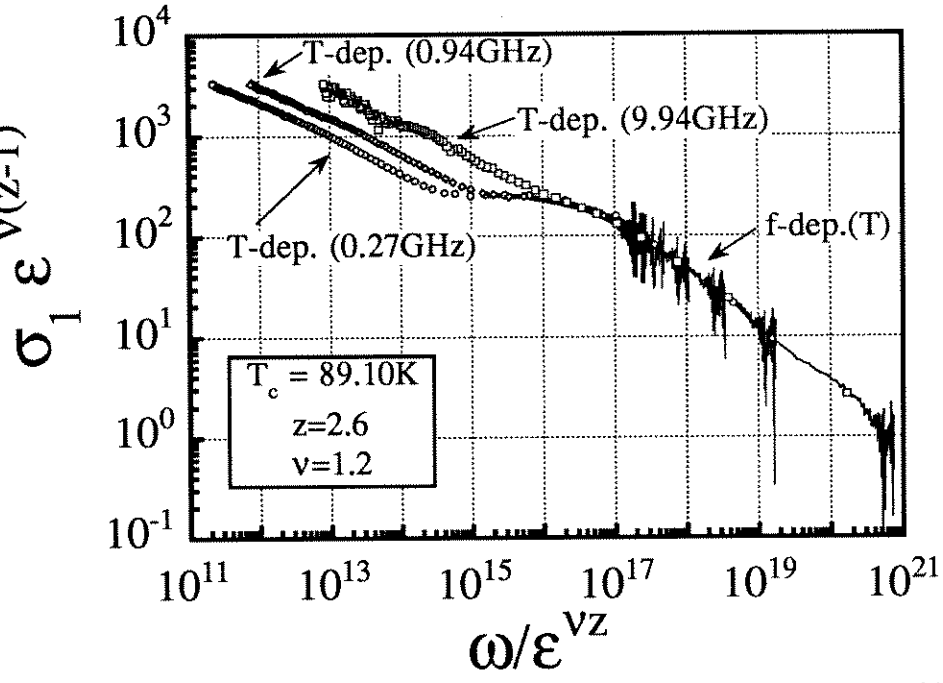


Fig. 5.15. The scaled temperature dependence of $\sigma_1$ at fixed frequency (symbols), along with the scaled frequency dependence at six different fixed temperatures (solid lines), all with $T_c$=89.10K, $\nu$=1.2, and z=2.6.

how both the temperature dependence and the frequency dependence of the fluctuation conductivity are both described by the single universal scaling function $S_+$ within the critical regime. The point at which the temperature-dependent data deviate from the universal curve indicate the temperature at which the sample leaves the critical regime ($T \sim T_c + 2$ K).

## 5.7. Sample Dependence of Fluctuation Effects

Before concluding it is necessary to address the question of what effect the presence of material disorder and inhomogeneity have on the above results. We address this question experimentally by measuring samples with varying amounts of disorder, as measured by high resolution x ray diffraction.[25] If our samples all belong to the same universality class then we expect them all to follow the same universal function with the same critical exponents as described above. In Fig. 5.16 we plot the scaled temperature dependence (with $\nu$=1.2 and z=2.6) of the fluctuation conductivity for thin film #NCL705b, along with the scaled temperature dependence of a second thin film (thin film #RAY7) and also a single crystal, all measured at approximately 10 GHz. The conductivity of the single crystal was measured using a cavity perturbation method[8]. Sample RAY7 has a broader resistivity transition width than film NCL705b, and the high resolution x ray diffraction results show that film RAY7 has a larger distribution of oxygen content, from which we conclude that film RAY7 is the more disordered of the two films.

In order to have the data from these 3 very different samples collapse onto the same curve, it is necessary only to adjust the non-universal values of $\tau_0$ and $\xi_0$ in the quantities $\xi = \xi_0/\varepsilon^{\nu}$ and $\tau = \tau_0/\varepsilon^{\nu z}$ in Eqs. 5.20 and 5.21. The relative values for $\tau_0$ and $\xi_0$ used to scale the data in Fig. 5.16 are given in table 5.2. If the single crystal is assumed to represent the least disordered sample, than table 5.2 indicates that the

"bare" relaxation time $\tau_0$ decreases with increasing disorder. Fig. 5.16 illustrates that our scaling results are relatively insensitive to disorder. This might be expected from the Harris criterion,[26] which predicts that if the specific heat exponent $\alpha$ is negative (which appears to be the case for YBCO[10]), then disorder should not affect the universality of the critical exponents and scaling functions.

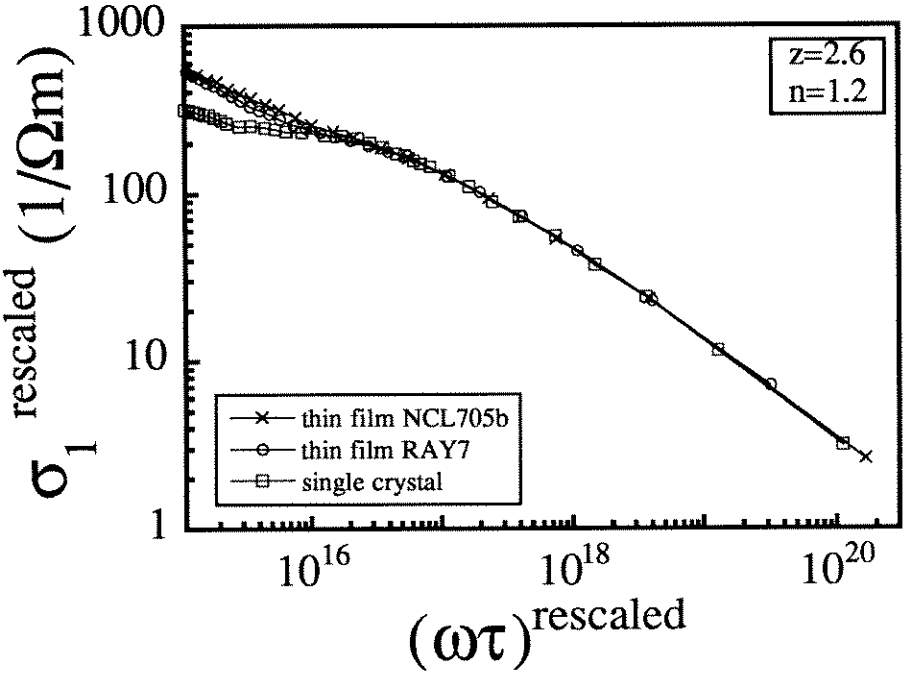


Fig. 5.16. The scaling of the temperature dependence of the fluctuation conductivity measured at approx. 10 GHz for 2 different thin film samples and a single crystal sample.

Table 5.2. Relative values of the non-universal parameters $\tau_0$ and $\xi_0$ for the different samples shown in Fig. 5.16.

| Sample | $\xi_0/(\xi_0^{\text{film\#NCL705b}})$ | $\tau_0/(\tau_0^{\text{film\#NCL705b}})$ |
|---|---|---|
| thin film # NCL705b | 1 | 1 |
| thin film #RAY7 | 0.625 | 0.5 |
| single crystal | 1 | 11 |

## Chapter 5 References


[1] D. S. Fisher, M. P. A. Fisher, and D. Huse, Phys. Rev B **43**, 130 (1991).

[2] C.J. Lobb, Phys. Rev. B **36**, 3930 (1987).

[3] S. L. Lehoczky, and C. V. Briscoe, Phys. Rev. Lett. **24**, 880 (1970); S. L. Lehoczky, and C. V. Briscoe, Phys. Rev B **4**, 3938 (1971).

[4] D. B. Tanner, Phys. Rev B **8**, 5045 (1973).

[5] M. B. Salamon in "Physical Properties of High Temperature Superconductors I", D. Ginsberg, Ed.,World Scientific, Singapore (1989).

[6] S. J. Hagen, Z. Z. Wang, and N. P. Ong, Phys. Rev B **38**, 7137 (1988).

[7] T. A. Friedmann, J. P. Rice, J. Giapintzakis, and D. M. Ginsberg, Phys. Rev B **39**, 4258 (1989).

[8] Steven M. Anlage, J. Mao, J. C. Booth, Dong Ho Wu, and J. L. Peng, Phys. Rev B **53**, 2792 (1996).

[9] S. Kamal, D. A. Bonn, N. Goldenfeld, P. J. Hirschfeld, Ruixing Liang, and W. N. Hardy, Phys. Rev. Lett. **73**, 1845 (1994).

[10] N. Overend, M.A. Howson, I.D. Lawrie, Phys. Rev. Lett. **72**, 3238 (1994).

[11] H. K. Olsson, R. H. Koch, W. Eidelloth, and R. P. Robertazzi, Phys. Rev. Lett. **66**, 2661 (1991).

[12] H. Wu, N. P. Ong, and Y. Q. Li, Phys. Rev. Lett. **71**, 2462 (1993).

[13] D.H. Wu et al., Phys. Rev. Lett. **75**, 525 (1995).

[14] N.-C. Yeh, D. S. Reed, W. Jiang, U. Kriplani, C. C. Tsuei, C. C. Chi, and F. Holtzberg, Phys. Rev. Lett. **71**, 4043 (1993).

[15] T.P. Orlando and K.A. Delin, "Foundations of Applied Superconductivity", Addison-Wesley, Reading, MA (1991).

[16] P.G. deGennes, "Superconductivity of Metals and Alloys", Addison-Wesley, Reading, MA (1966).

[17] M. Tinkham, "Introduction to Superconductivity", Robert E. Krieger Publishing Company, Malabar, FL (1975).

[18] W.J. Skocpol and M. Tinkham, Rep. Prog. Phys. **38**, 1049 (1975).

[19] H. Schmidt, Z. Phys. **216**, 336 (1968); H. Schmidt, Z. Phys. **232**, 443 (1970)

[20] A. T. Dorsey, Phys. Rev B **43**, 7575 (1991).

[21] L. G. Aslamazov and A. I. Larkin , Fiz. Tverd. Tela **10**, 1104 (1968) [Sov. Phys. Solid State **10**, 875 (1968)].

[22] W. E. Lawrence and S. Doniach, Proceedings of the Twelfth International Conference on Low-Temperature Physics, Kyoto, 1970, edited by E. Kanda (Keigaku, Tokoyo, 1970), p. 361.

[23] C. Dekker *et al.*, Physica C **185-189**, 1799 (1991).

[24] J.M. Roberts *et al.*, Phys. Rev. B **51**, 15281 (1995).

[25] E.F. Skelton et al., SPIE Proceedings **1516**, 160, W. Yun, Ed. (1995).

[26] A.B. Harris, J. Phys. C **7**, 1671(1974).

# Chapter 6
# Magnetic Field Measurements – Vortex Dynamics in YBCO Thin Films

## 6.1 Introduction

Information obtained from microwave measurements about vortex motion in the high $T_c$ superconductors is important for fundamental reasons, as well as for many technological applications of high $T_c$ superconductivity. Of fundamental interest is the question of what general laws govern vortex motion in superconductors. There has been a tremendous amount of theoretical and experimental work on the properties of the high $T_c$ superconductors in an external magnetic field, which has uncovered a large number of interesting phenomena. The relevant physical parameters of the high $T_c$ materials, such as the high accessible temperatures, small coherence length, and strong anisotropy mean that these systems are much more susceptible to different kinds of disorder than their low $T_c$ counterparts. Experiments that focus on vortices in high $T_c$ superconductors give one the opportunity to study the role of quenched disorder, thermal disorder, and quantum disorder, which can lead to new and exotic phases such as a vortex glass phase, or an entangled vortex liquid phase.[1] There is also the possibility of observing phase transitions within the vortex system, such as the melting of the vortex glass phase.[2] All of these considerations make the study of the mixed state in the high $T_c$ superconductors a rich and extremely interesting field.

Much of the experimental and theoretical work to date on vortices in high $T_c$ superconductors has focused on dc transport properties. While this effort has resulted in a more detailed understanding of vortex response subject to a dc driving current, it is not clear if all of the conclusions from dc investigations are directly applicable, or even relevant, at ac frequencies. In the study of vortex motion at finite frequencies, many

fundamental issues have yet to be resolved. For instance, it is not clear if single particle phenomenological models[3,4] can adequately describe vortex motion at rf and microwave frequencies. Alternative theories of vortex motion predict the existence of vortex core excitations and unusual optical activity[5], which should be observable in microwave surface impedance measurements. In addition, the investigation of collective properties of the vortex state, such as phase transitions and melting,[2] also provide motivation for a careful study of vortex dynamics in superconductors using high frequency techniques. High frequency experiments have the advantage of using very small current densities in order to probe reversible oscillations of vortices, and may be less sensitive to flux creep than dc experiments.[6]

An understanding of vortex motion at rf and microwave frequencies is important also for practical reasons, since some of the most promising near-term significant applications of high $T_c$ superconductivity are in rf and microwave subsystems and components. Many of these applications require superconducting devices to operate under non-optimum conditions, such as large magnetic fields and/or high microwave power. Under such conditions, where high microwave power may induce an rf critical state,[7] the most significant limitations to the widespread use of high $T_c$ components are the considerable power dependence exhibited by both passive and active devices, and intermodulation distortion caused by non-linearities in the surface impedance. Many of these limitations are directly related to the generation and/or motion of magnetic vortices under the influence of rf or microwave fields. The frequency range from 45 MHz to 50 GHz includes many technologically important applications, such as cellular telephone, PCS, and radar systems, and many devices that operate at these frequencies will therefore need to explicitly take into account the effects of vortex motion if they are expected to operate at high powers or fields. Also, such information is essential for non-reciprocal devices such as circulators and

isolators that require a fixed magnetic field to operate.[8]

This chapter will examine primarily the effect of the driving frequency on vortex motion in the high $T_c$ superconductors. Section 6.2 will briefly review some of the fundamental properties of magnetic vortices in the mixed state of type II superconductors. In section 6.3 some of the relevant theoretical models of the dynamics of vortices at high frequencies will be introduced, and some of the experiments used to test these models will be described. Then in section 6.4 some of the details of measurements of vortex dynamics in the Corbino geometry are discussed. In section 6.5 the main experimental results on the frequency dependence of vortex dynamics in YBCO thin films are presented, and in section 6.6 the implications of these findings for the technological applications of high $T_c$ superconductors are briefly discussed. The main conclusion of this chapter is that the response of the mixed state in high $T_c$ superconductors depends sensitively on the driving frequency, with a given response at low frequencies ($\leq$ 1 GHz), and a very different response for high frequencies ($\geq$ 10 GHz) for many temperatures and magnetic field strengths.[9]

## 6.2 The Mixed State in Type II Superconductors

The coherence length in the high $T_c$ superconductors is much smaller than the penetration depth, making these materials extreme type II superconductors. The fact that the mixed state covers most of the B-T phase diagram in these materials makes it very important to understand how vortices respond to an applied current in the high $T_c$ superconductors. The mean-field phase diagram for a general type II superconductors can be described as follows. At fields and temperatures above the lower critical field $H_{c1}(T)$ one enters the mixed state, where the magnetic field penetrates the superconductor in the form of quantized magnetic vortices. The mixed state is characterized by a rigid triangular (Abrikosov) vortex lattice that persists until the upper

critical field, $H_{c2}(T)$, is exceeded and the superconductor is driven into the normal state. For a superconductor in the mixed state, an applied current produces a Lorentz force on a vortex: $F_L=\phi_0 \mathbf{n} \times \mathbf{J}$, where n is a unit vector directed along the vortex, and $\phi_0$ is the flux quantum. Vortices that move under the influence of this force produce loss in the superconductor. The presence of material defects in the superconductor will provide pinning sites for vortices, which serve to prevent vortex motion and restore the ability of the superconductor to carry a current without dissipation. In the conventional superconductors the rigid vortex lattice means that only a few material defects can effectively pin the entire vortex lattice.

The response of a superconductor in the mixed state to an applied dc current can then be described as follows. For small currents, the vortex lattice is effectively pinned, and the superconductor can carry a current with zero dissipation. As the driving current increases, however, the Lorentz force will eventually overcome the pinning forces, and the vortices will begin to move under the influence of the Lorentz force and cause dissipation. The current at which the depinning occurs is called the critical current $J_c$, and represents the maximum dc current that a superconductor can carry without loss. So for dc considerations, $J_c$ is the important material parameter by which a superconductor can be characterized.

There exists another mechanism by which dissipation due to flux motion can occur, even for currents less than $J_c$. In this case, vortex motion occurs by thermally activated jumps over pinning barriers, a phenomenon referred to as flux creep. Since it is an activated process, however, the losses due to flux creep are usually very small in the conventional superconductors, except very near $T_c$, due to the low temperatures and large activation barriers. In the HTSC, however, it is expected that flux creep processes may be much more important.

## 6.3 Vortex Motion at rf and Microwave Frequencies

This section will attempt to describe the current understanding of vortex motion in superconductors at rf and microwave frequencies. The discussion will be simplified whenever possible by examining separately the low frequency and high frequency limits in the context of the various theoretical models. The relevant experimental evidence supporting the different theories will also be discussed.

### 6.3.1 Vortex Motion in Conventional Superconductors

In conventional type II superconductors, one understands the low frequency ac response in terms of the same mean-field phase diagram that one uses at dc. The response of the superconductor in the mixed state at low frequencies is therefore governed by the critical current of the material, with "superconducting" (or lossless) behavior observed as long as the ac current density is less than the critical current density $J_c$.

As the ac driving frequency increases, however, one can observe dramatically different behavior from that described above:[3] the sudden onset of loss occurs in the superconductor as one passes a characteristic frequency (called the "depinning frequency"), even with subcritical ac current densities. For driving frequencies above this depinning frequency the entire vortex lattice executes small oscillations about the equilibrium pinning position, giving the same response as one would observe if the pinning were absent. Hence for conventional superconductors in the mixed state, one can clearly demarcate two distinct regions in frequency: a low-frequency, lossless regime in which the vortex lattice is effectively pinned ($f<f_{depin}$) , and a high-frequency, lossy regime ($f> f_{depin}$) in which the response of the vortex lattice is the same as if the pinning were absent and the vortices were free to move.

Gittleman and Rosenblum[3] described the observed ac response of the mixed

state in type II superconductors in terms of an equation of motion for a single particle in a periodic pinning potential acted on by a driving force and a viscous force. With the assumption that the vortex displacement is small, the effect of the pinning potential can be approximated by a linear restoring force. With that simplification, the following equation of motion is obtained for the vortex displacement x:

$$m\ddot{x} + \eta\dot{x} + \kappa_p x = J\,\phi_0 \tag{6.1}$$

In this equation m is the effective vortex mass, $\eta$ is the viscosity coefficient, and $\kappa_p$ is the pinning force constant, while J is the component of the current density perpendicular to the vortex, and $\phi_0$ is the flux quantum. Equation 6.1 is valid only for small vortex displacements, where the approximation of a linear restoring force is valid. Also note that Eq. 6.1 describes a vortex interacting with a single pinning potential, which represents the interaction between the entire vortex lattice and the pinning sites in the material. By assuming a periodic time dependence for all quantities, Eq. 6.1 can be combined with Faraday's law to obtain an expression for the complex resistivity due to vortex motion. With the further assumption that the vortex mass can be neglected, the complex resistivity resulting from vortex motion is found to be

$$\rho_v = \rho_{ff}\frac{(\omega\tau_0)^2 + i(\omega\tau_0)}{1 + (\omega\tau_0)^2} \tag{6.2}$$

where $\omega_0$ (= $1/\tau_0$) = $\kappa_p/\eta$ is the depinning frequency, and the flux-flow resistivity is given by $\rho_{ff} = B\phi_0/\eta$. For the conventional superconductor PbIn, the depinning frequency is on the order of ~7 MHz at 1.7 K, while for NbTa at 4.2 K the value is ~26 MHz.[3]

Equation 6.2 is important because it forms the basis for more sophisticated treatments of vortex motion that are applied to the high $T_c$ superconductors. The real

and imaginary parts of $\rho_v/\rho_{ff}$ given by Eq. 6.2 are plotted as a function of frequency in Fig. 6.1. Note that the losses as measured by real$\{\rho_v\}$ increase dramatically at $\omega=\omega_0$, and approach $\rho_v/\rho_{ff} = 1$ at high frequency. Since $\rho_{ff}$ is the resistivity one would measure for free vortex motion, Fig. 6.1 implies that at high enough frequency the vortices behave as if the pinning were absent; hence the term depinning frequency. Note also that imaginary$\{\rho_v\}$ is a maximum at the depinning frequency $\omega=\omega_0$. Therefore at higher frequencies the pinning constant $\kappa_p$ becomes the relevant material parameter for describing the strength of pinning in a material, rather than the critical current density $J_c$, which is the measure of pinning strength for dc considerations.

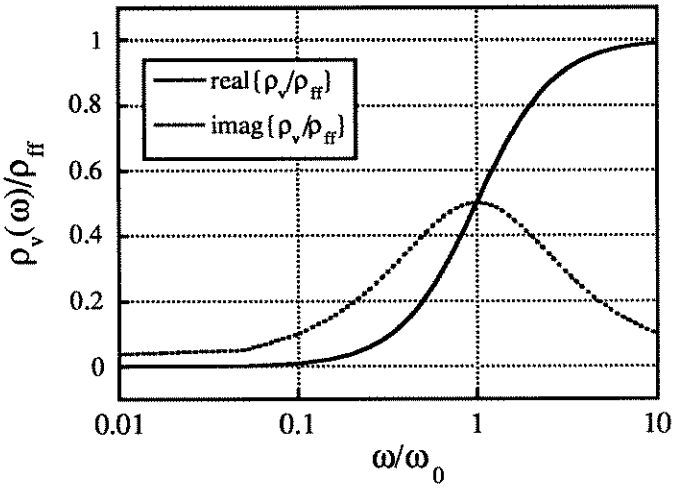


Fig. 6.1. The real and imaginary parts of the vortex resistivity as a function of frequency, as calculated from Eq. 6.2.

### 6.3.2 Scaling Models in HTSC

In the high $T_c$ superconductors a number of factors, such as the short coherence lengths, strong anisotropy, and large thermal energies conspire to make the situation in the mixed state more complicated than in conventional superconductors. In the low frequency limit the main effects on the mixed state are the following: (a) the vortex lattice state is replaced by a novel vortex glass state, in which the long range crystalline order of the vortex lattice is destroyed by pinning disorder and thermal fluctuations,

and (b) the appearance of a "vortex liquid" state at fields and temperatures well below the upper critical field $H_{c2}(T)$. Fig. 6.2 shows a possible phase diagram for the high $T_c$ superconductor YBCO.[10] The vortex glass state remains a "true superconducting" state in which the losses go to zero in the limit of zero current. For large currents, however, the current-voltage response in the vortex glass state can become very non-linear. The vortex liquid state is characterized by finite losses in the superconductor for arbitrarily small dc currents. This means, among other things, that any practical device that makes use of superconducting properties must be operated well below the vortex "melting" transition $H_m(T)$.[11]

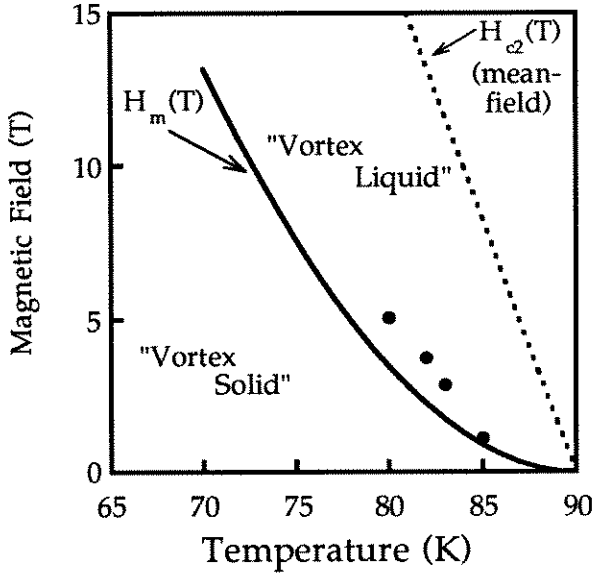


Fig. 6.2. Possible vortex phase diagram for YBCO. The "melting" line $H_m(T)$ separates a vortex solid state from a vortex liquid state. The data points represent an experimental determination of the phase boundary as discussed in section 6.5. The Meissner state is very near H=0 on this scale.

The existence of a vortex glass state and the associated glass to liquid transition was predicted by Fisher, Fisher, and Huse.[2] Experimental evidence for such a transition in the high $T_c$ materials has been observed in measurements of the non-linear dc current-voltage (I-V) characteristics in the presence of a large external magnetic

field.[12] These experiments support the existence of a vortex phase transition using scaling arguments that predict the collapse of I-V curves measured at different temperatures onto a single pair of curves, when scaled by the appropriate power of the vortex glass transition temperature $T_g$. Such scaling treatments of the non-linear I-V curves yield, along with $T_g$, the critical exponents $\nu$ and z that describe the vortex glass to liquid phase transition. Experiments of this type have been performed on both YBCO films[12]and crystals[13,14], all of which show the predicted scaling behavior with critical exponents that vary somewhat. The scaling of behavior of the I-V curves is very robust, and has been seen in many different types of samples, including proton-irradiated YBCO crystals[15], underdoped YBCO films[16], Al-doped YBCO films[17], and with varying magnetic field angle[18], and with varying sample size[19]. Scaling of the I-V curves has also been observed in other materials, such as BSCCO thin films[20] and crystals[21], and even in $Mo_3Si$ thin films[22]. The values of the critical exponents vary somewhat for all these different measurements, with the static critical exponent $\nu$ ranging from 0.7-2.0 and the dynamical critical exponent z in the range 3.4-6.0.

Experimental evidence for the existence of a vortex-liquid to -glass phase transition has also been observed in measurements of the frequency dependent resistivity, which make use of a different set of scaling relations[2]. These measurements show that the frequency-dependent conductivity in YBCO thin films can be collapsed using scaling relations over the frequency range from 100 kHz - 500 MHz[23], $10^{-1}$ - $10^5$ Hz[24], and 1-600 MHz[25]. Such frequency-dependent scaling has also been shown for YBCO single crystals, over the frequency range 3 Hz - 3 MHz[26], from 100 Hz - 2 MHz[27], and from 4 - 100 kHz[28]; and also for $Mo_3Si$ films (100 Hz - 3 MHz).[22] The finite-frequency measurements in general yield critical exponents that are consistent with the dc measurements, but still show some

spread in the actual values (see ref.[26], for example).

The finite frequency measurements show that at the liquid to glass transition the frequency dependence of the real and imaginary parts of the complex resistivity can be described by power laws:

$$\rho_1(\omega) \sim \omega^{\alpha_1}$$
$$\rho_2(\omega) \sim \omega^{\alpha_2} \qquad (6.3)$$

with $\alpha_1 = \alpha_2$ ($\cong 0.73$) at the vortex liquid to glass transition[25], and with $\alpha_1 > (<) \alpha_2$ below (above) the glass to liquid transition. The ac measurements described above did not extend into the microwave regime, with the highest measured frequency being approximately 600 MHz. It should be pointed out that in the conventional superconductors this "melting" transition occurs essentially at the upper critical field $H_{c2}(T)$ and the vortex liquid region in the H-T phase diagram is unobservably narrow.

### 6.3.3 Single-Particle Models in HTSC

For the high $T_c$ superconductors one might also expect qualitatively different behavior if the driving frequency is sufficiently high. This is because as the measurement frequency increases, the probing time scale becomes shorter, not allowing vortex lines enough time to interact with other vortices. Hence for high frequencies one might expect mean field models such as those employed for conventional superconductors to be more appropriate than the vortex interaction based glass/liquid models mentioned above. In this limit the vortices behave as individual flux lines. However, the short coherence length and disordered pinning potential in the high $T_c$ superconductors mean that the interaction between the pinning potential and the vortices may be more complicated than for the conventional superconductors, where it is assumed that the rigid vortex lattice interacts with a single pinning potential.[3]

Coffey and Clem provided a generalization of the treatment of vortex motion

discussed in section 6.3.1 to include the influence of both pinning and thermally activated effects in a unified theory of vortex response.[4] In their treatment, the vortex equation of motion (Eq. 6.1) is modified by including a random or Langevin force on the right hand side, in addition to the usual Lorentz force, in order to account for thermally activated effects. This modeling of the problem is similar to the treatment of a particle undergoing Brownian motion in a periodic potential. With this generalization, the resulting vortex motion resistivity is modified from Eq. 6.2 as

$$\rho_v(\omega) = \rho_{ff} \frac{\varepsilon + (\omega\tau)^2 + i(1-\varepsilon)\,\omega\tau}{1 + (\omega\tau)^2} \tag{6.4}$$

Here $\rho_{ff} = B\phi_0/\eta$, as before. However, there appears an additional term $\varepsilon$ in Eq. 6.4, which is called the flux-creep factor, and accounts for thermally activated vortex motion over a barrier of height $U_0$. The expression for $\varepsilon$ is given by $\varepsilon = 1/I_0^2(\nu)$, where $I_0$ is a modified Bessel function of the first kind of order zero, and the temperature-dependent argument $\nu$ is given by $\nu = U_0(T)/2k_BT$. Note that $\varepsilon$ is bounded between 0 and 1. In addition to the appearance of the flux-creep factor $\varepsilon$, the vortex relaxation time $\tau$ is modified as

$$\tau = \tau_0 \frac{I_0^2(\nu) - 1}{I_1(\nu)\, I_0(\nu)} \tag{6.5}$$

where $\tau_0 = \eta/\kappa_p$, as in Eq. 6.2, and $I_0$ and $I_1$ are modified Bessel functions.

Note that the appearance of the pinning force constant $\kappa_p$ in the above treatment means that it is assumed that the vortices all interact with a single pinning potential characterized by the single parameter $\kappa_p$, as in Eq. 6.1. While this is a good approximation for the conventional superconductors, where the pinning is collective, it is not clear that it is a good approximation for the high $T_c$ materials at microwave frequencies, where the pinning is largely individual.[6] In addition, the effect of

disorder in the individual pinning regime also needs to be considered.

Equation 6.4 gives the complex resistivity due to vortex motion in a superconductors in terms of three independent parameters: $\kappa_p$, $\eta$, and the flux-creep argument $\nu$, all of which are temperature and/or magnetic field dependent. In order to unambiguously determine all three parameters, measurements at different frequencies are required. When such measurements at different frequencies are performed, it is found that in order for Eq. 6.4 to consistently describe the data, at least some of these three parameters must be frequency-dependent.[28] Also, in the limit where $\omega\tau<<1$ (and $\varepsilon<<1$), Eq. 6.4 predicts a frequency dependence of $\rho_1 \sim \omega^2$, while experiments show $\rho_1 \sim \omega^{1.2}$.[29]

In spite of the above difficulties, many experiments performed on YBCO films at microwave frequencies (1-35 GHz)[29-38] have been successfully interpreted using such mean-field based models.[4] Many of these experiments work at low fields and temperatures in order to minimize the effects of flux creep, thereby reducing the number of parameters necessary for a complete description from three to two. Such measurements utilize a variety of techniques, and examine a wide variety of different YBCO samples, from thin films to single crystals. The results for the value of the pinning force constant $\kappa_p$ are surprisingly consistent, with $\kappa_p(T=0) \sim 1\text{-}2 \times 10^5$ N/m$^2$. The observed temperature dependence is also very similar among the different experiments, showing that $\kappa_p$ decreases with increasing temperature, with a functional dependence of approximately $(1-(T/T_c)^2)^2$.[39] Also, $\kappa_p$ seems to be independent of magnetic field, indicating that the pinning is individual in these experiments.[6]

Such microwave experiments also yield values for the viscosity coefficient $\eta$ and the depinning frequency $\omega_0$ in YBCO. At temperatures in the range 65-90 K, $\eta$ varies in the range $0.1 \times 10^{-7}$ to $2 \times 10^{-7}$ Ns/m$^2$, and decreases with increasing temperature, and is also independent of magnetic field. Values for the depinning

frequency $\omega_0/2\pi$ are in the range 20-100 GHz, and decrease slightly with increasing temperature. These values for the "depinning frequency" in YBCO are much higher than for the conventional materials, which would imply, for example, a much wider operational frequency range for a high $T_c$ device at a given temperature.

Measurements at still higher frequencies, for example in the terahertz regime[40] (500 GHz-1 THz), are also well described by the mean-field (or single-particle) picture. In addition, far infrared measurements[41] are also in agreement with single-particle models[5] that neglect vortex-vortex interactions. The large number of experiments that can be more or less consistently described by mean-field models strongly suggests that there is at least some degree of relevance to the single-particle descriptions. However, these results seem to be in contradiction with the lower frequency experiments that support the vortex glass-based models described in section 6.3.2.

## 6.4 Vortex Dynamics in the Corbino Geometry

Given the above considerations, measurements of the mixed state of high $T_c$ superconductors that span a wide frequency range in the rf, microwave, and millimeter-wave regimes seem very desirable. In addition to the access to a wide frequency range (45 MHz - 50 GHz), the Corbino reflection technique offers several other advantages when studying vortex dynamics. The Corbino disk geometry (recall that the annular region of the film exposed between the inner and outer conductors defines a Corbino disk) is advantageous because the edges of the sample are effectively eliminated and do not contribute to the creation and/or pinning of vortices. The coaxial geometry also means that the same mode (TEM) can be used to measure at all frequencies, as opposed to stripline or microstrip resonators,[29,34] which use different modes, and hence different field distributions, for different (discrete)

frequencies. Another result of using the coaxial TEM mode, in addition to the absence of a lower cut-off frequency, is that the field distribution in the film is particularly simple, with the fields and currents proportional to 1/r (where r is the distance from the center of the disk), and uniform throughout the film thickness (for sufficiently thin films).

The Corbino reflection technique is applied to measure the response of the superconducting mixed state over a very wide and technologically important frequency range (45 MHz - 50 GHz) in the rf and microwave regime. The sensitivity allows for measurement of changes in the complex resistivity $\rho$ of $\sim 10^{-9}$ $\Omega$m at low frequencies for a typical film thickness of 1000 Å. The ac current density can also be varied, by changing the microwave power, and can be used along with a dc current bias, to study the detailed form of the pinning potential in the high $T_c$ materials. For the measurements described here the ac current density was kept small, approximately 80-200 A/cm$^2$. Measurements were carried out on several c-axis YBCO thin films of thickness ~1000 Å fabricated by pulsed laser deposition on $LaAlO_3$ substrates.

## 6.5 Vortex Response in YBCO Thin Films at Microwave Frequencies

### 6.5.1 Frequency Dependence

The goal of the measurements described here is to test directly the validity of the vortex glass-based scaling models at frequencies much higher than previously examined. To accomplish this goal, measurements are performed from 45 MHz - 50 GHz in the vicinity of the melting line in the mixed state phase diagram (one possible phase diagram for YBCO is shown in Fig. 6.2, for example).

Data from one such measurement of the mixed state of a YBCO thin film is shown in Figs. 6.3 and 6.4, which exhibit the frequency dependence of the real and imaginary parts respectively of the complex resistivity at a temperature of 80.2 K and

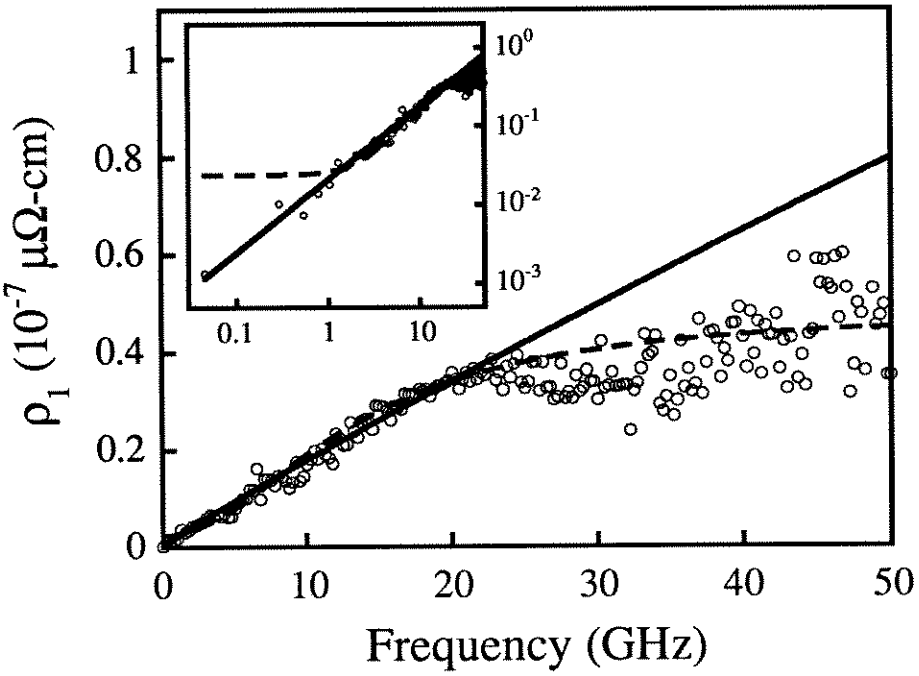


Fig. 6.3. The frequency dependence of $\rho_1(\omega)$ for a YBCO c-axis thin film at T=80.2 K and H=0.4 T. The solid line represents $\rho_1 \propto \omega^{\alpha 1}$, with $\alpha_1 = 0.81$, and the dashed line represents the mean-field fit. The inset shows the same data on a log-log plot.

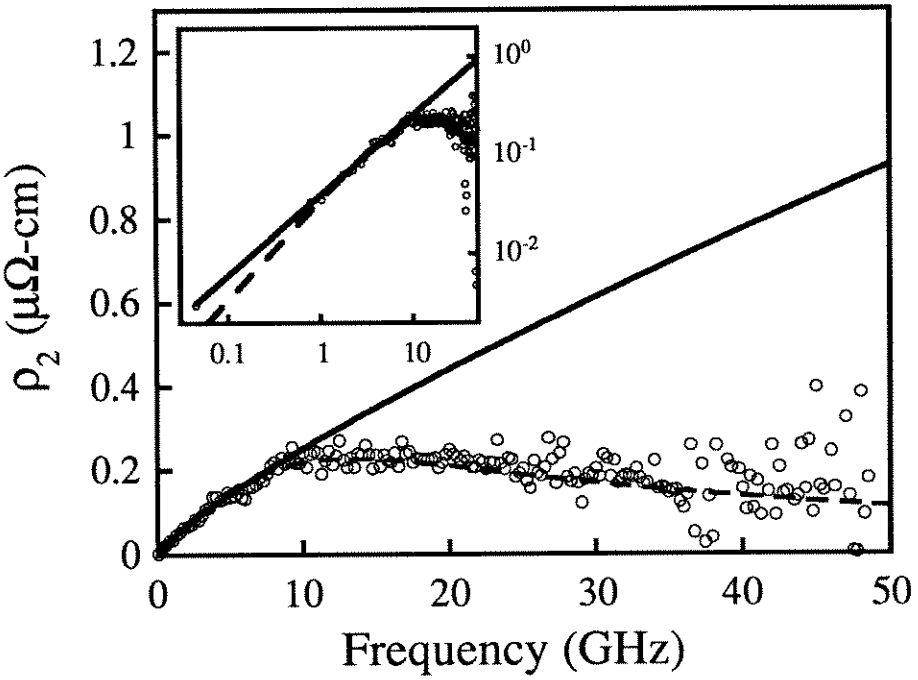


Fig. 6.4. The frequency dependence of $\rho_2(\omega)$ for a YBCO c-axis thin film at T=80.2 K and H=0.4 T. The solid line represents $\rho_2 \propto \omega^{\alpha 2}$, with $\alpha_2 = 0.93$, and the dashed line represents the mean-field fit. The inset shows the same data on a log-log plot.

an applied magnetic field of 0.4 T. Recall that the complex resistivity $\rho$ relates the time dependent electric field to the time dependent current density according to $E=\rho J$. The real part of the complex resistivity $\rho_1$ is a measure of the energy loss, while the imaginary part $\rho_2$ is a measure of the reactance, or energy stored. Also shown in Figs. 6.3 and 6.4 are mean-field fits to the data (dashed lines), and fits to the vortex solid to liquid scaling forms $\rho_1 \sim \omega^{\alpha}1$ and $\rho_2 \sim \omega^{\alpha}2$ (solid lines). The fitting function for the mean field fits is given by Eq. 6.4.

Figs. 6.3 and 6.4 clearly show one of the major results of our work: at low frequencies the data follow the vortex solid to liquid scaling models (evident in the log-log plots shown in the insets), while at high frequencies the data deviate from the scaling predictions and rather show good agreement with a mean field description. The cross-over frequency from scaling to mean-field behavior occurs for the data in Figs. 6.3 and 6.4 at about 10 GHz, and the data shows a smooth transition from the low-$\omega$ regime to the high-$\omega$ regime. The values for $\alpha_1$ and $\alpha_2$ derived from the data shown in Figs. 6.3 and 6.4 (0.81 and 0.93, respectively) indicate that this point in the mixed state phase diagram (80.2 K and 0.4 Tesla) is on the vortex solid side of the vortex liquid/solid boundary. In order to investigate the vortex liquid side of the phase boundary, similar data is obtained at higher temperature and magnetic field strength and is shown in Figs. 6.5 and 6.6. This data also shows the same crossover from scaling behavior at lower frequencies to mean-field behavior at higher frequencies.

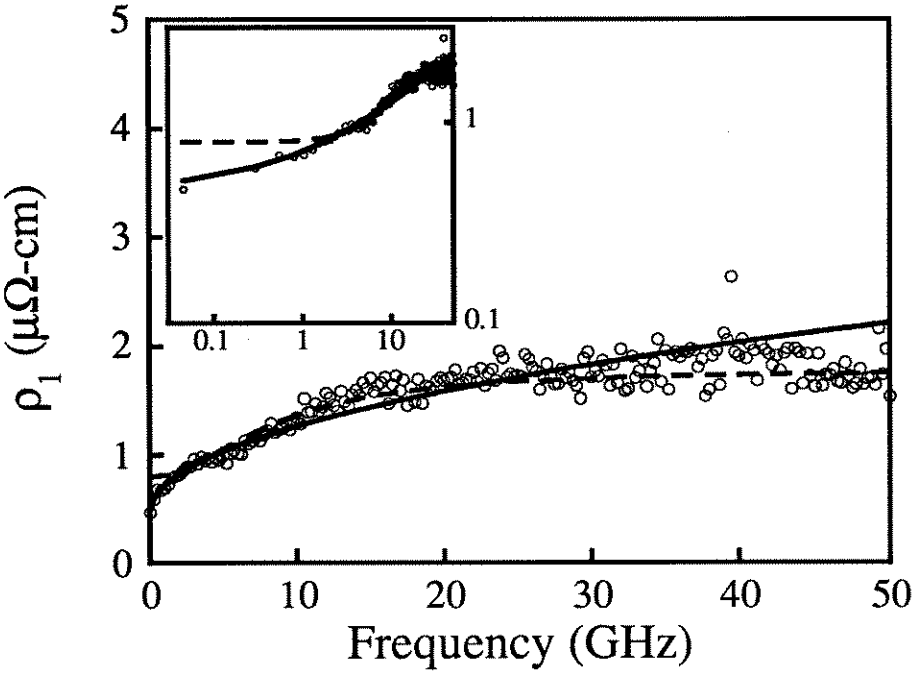


Fig. 6.5. The frequency dependence of $\rho_1(\omega)$ for a YBCO c-axis thin film at T=83.6 K and H=4 T. The solid line represents $\rho_1 = \rho_1 + a_1\ \omega^{\alpha 1}$, and the dashed line represents the mean-field fit. The inset shows the same data on a log-log plot.

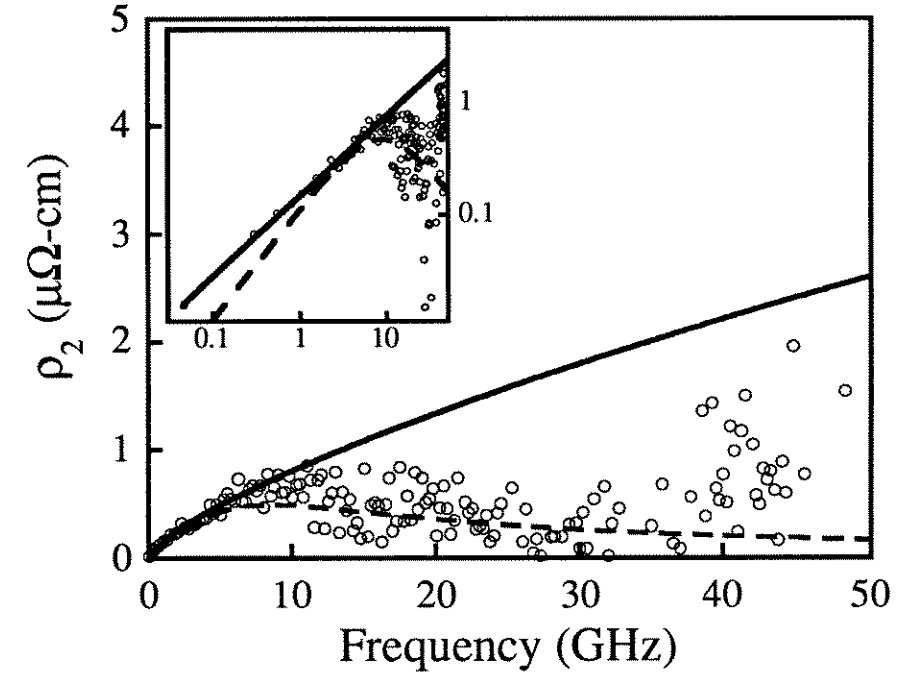


Fig. 6.6. The frequency dependence of $\rho_2(\omega)$ for a YBCO c-axis thin film at T=83.6 K and H=4 T. The solid line represents $\rho_2\ \alpha\ \omega^{\alpha 2}$, and the dashed line represents the mean-field fit. The inset shows the same data on a log-log plot.

Another quantity of considerable interest is the phase angle of the complex resistivity, defined by $\rho = |\rho|e^{i\phi}$, so that $\phi = \tan^{-1}(\rho_2/\rho_1)$. The frequency dependence of the resistivity phase angle is shown for three different points in the mixed state phase diagram in Fig. 6.7. At the location of the vortex solid/liquid boundary, the resistivity phase angle is predicted by scaling theory to be a constant value, independent of frequency, while above (below) the boundary the phase angle should be an increasing (decreasing) function of frequency. The data shown in Fig. 6.7 exhibit this behavior at low frequency, but for all the curves, the high frequency data show a phase angle that decreases as $1/\omega$, which is just what is expected from mean-field theory. The behavior of the frequency dependence of the resistivity phase angle therefore also shows a crossover from scaling to mean-field behavior as the frequency increases.

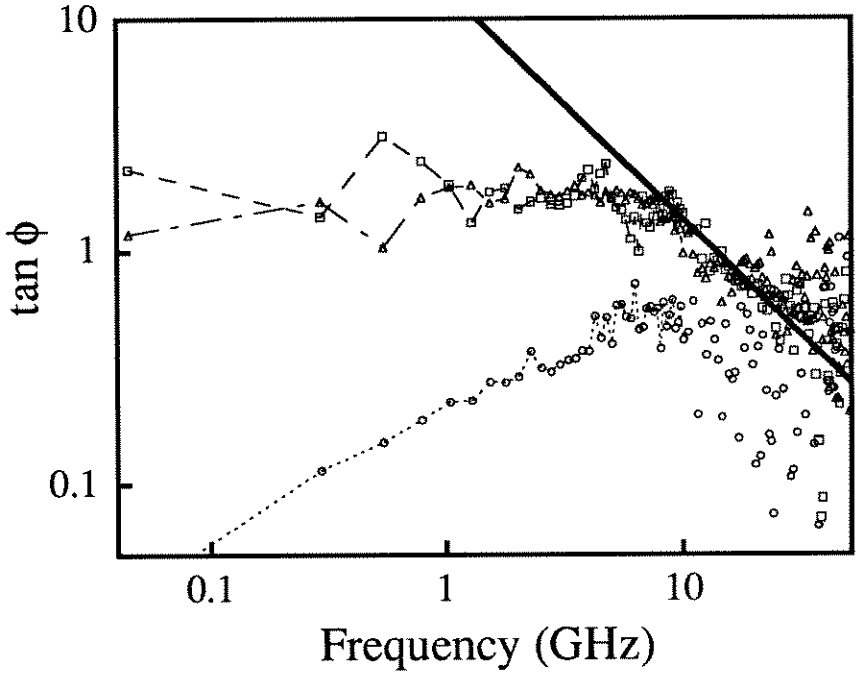


Fig. 6.7. The phase angle tanϕ vs. frequency for various temperatures and field strengths, given by T=80.2K and H=0.4T (dashed line); T=86K, H=0.3 T (dash-dotted); and T=83K, H=4T (dotted).

We can obtain a measure of the characteristic vortex relaxation time $\tau$ (which gives the "depinning frequency" $f_{depin} \sim 1/\tau$) from the mean-field fit to the high frequency data. We find for instance at T=78 K and H=0.3 T, that $1/\tau \sim 13 \times 10^9$ $sec^{-1}$, which is somewhat larger than earlier results from YBCO crystals,[39] but smaller than that obtained for a thick (~1μm) YBCO film.[31] Also, using the value of $\rho_f$ obtained from the fit, we extract $\eta \sim 2 \times 10^{-8}$ Nsec/$m^2$ for T=80.2 K and $H_{dc} = 0.4$ T. The mean-field fits also give values of $\varepsilon$ in the range $0.05 < \varepsilon \leq 0.5$ for 80 K < T < 86 K and $0 < H_{dc} < 1$ T.

### 6.5.2 Magnetic Field Dependence

We can also gain some insight into the nature of vortex motion from the detailed shape of the $\rho_1$ vs. $H_{dc}$ curves shown in Fig. 6.8, which displays $\rho_1(H)$ measured at T=83.5 K for various frequencies, along with mean-field fits. The mean-field fits are obtained using the full expressions for $\rho$ (given in Eq. 6.4). Note that $\nu$ can be written as $\nu = H^*/H$ if we assume the barrier height depends on the magnetic field as $U_0 \sim 1/H$, so that $H = H^*$ represents the field at which $U_0(H) = 2k_BT$ and significant flux creep begins to occur. The data measured at 11 and 13 GHz follow the mean-field description for all fields. The 11 and 13 GHz fits yield values for $H^* \sim 3.5$ Tesla, $\eta \sim 3.2 \times 10^{-8}$ Nsec/$m^2$ and a pinning force constant $\kappa_p = 3.5\text{-}4.5 \times 10^3$ N/$m^2$. The low frequency data (f=3 GHz and 6 GHz), however, cannot be reconciled with the mean-field fit with reasonable parameter values. The magnetic field dependence therefore corroborates the conclusion drawn from the frequency dependent data: the mean-field description is adequate for the high frequency data ($f \geq 10$ GHz) while the low frequency data requires consideration of vortex-vortex interactions for a quantitative description. Note that the values for the mean-field parameters $\eta$ and $\kappa_p$ derived from the magnetic-field dependent fits are consistent with the values obtained from the mean-

field fits to the frequency dependence.

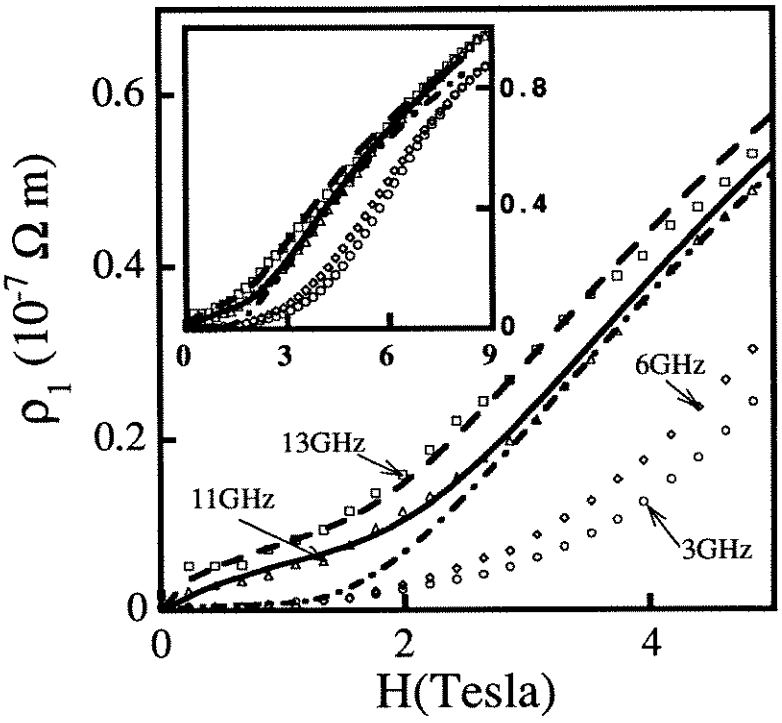


Fig. 6.8. Magnetic field dependence of $\rho_1$ for a YBCO thin film for various frequencies at T=83.5 K. Dashed-dot line is a mean field fit for 3 GHz. Solid line and dashed line are mean field fits for 11 and 13 GHz respectively. Inset: $\rho_1$ (H) for $0 \leq H \leq 9$ T.

The $\rho_1$ vs. H curves for the high frequency data can also be used to locate approximately the "melting transition" in the H-T phase diagram. If we take as a criterion for melting that $\rho_1(H_m) \approx 0.1\rho_n$, where $\rho_n$ is the normal state resistivity at $T_c$, then one obtains for the "melting line" the points shown in Fig. 6.2. The field for which this criterion is satisfied also corresponds to a peak in the quantity $\rho_2(H)/H$ vs. H, shown in Fig. 6.9, which is the imaginary part of the dynamic mobility of the vortex in the mean field picture[4] ($\rho^* = B\phi_0\mu^*$, where $\mu^*$ is the complex dynamic mobility). Although this is not a stringent criterion for the melting of the vortex lattice,[11] it provides an order of magnitude estimate for $H_m(T)$.

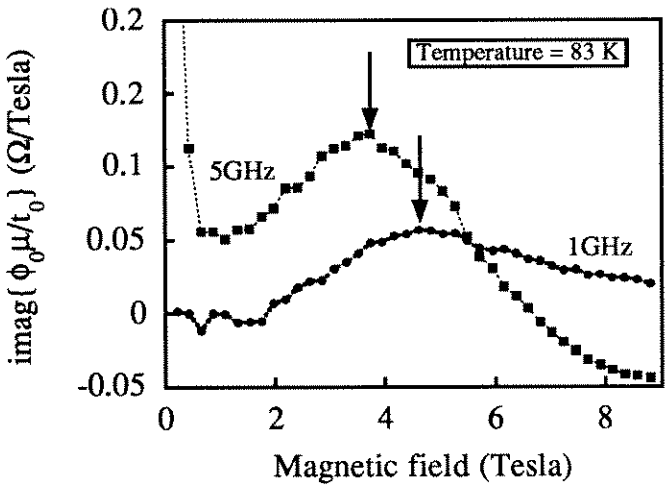


Fig. 6.9. The imaginary part of the dynamic mobility at frequencies of 1 GHz and 5 GHz.

## 6.6. Implications of Frequency Dependent Measurements

The frequency dependent measurements presented above serve to connect two seemingly contradictory sets of experimental results. The dc and low frequency experiments show much evidence for the existence of a vortex glass/liquid state. However, microwave, THz, and far-infrared experimental results are well described by the mean-field models. Our experiments show that both sets of results are in fact consistent, with the broad frequency range of our measurements providing a bridge between these two very different regimes. The crossover from the vortex glass/liquid scaling behavior to the mean-field-like behavior as the frequency increases is likely related to a crossover from **intervalley transitions**,[42] where the vortices move collectively by thermally activated hops between different metastable states in the random pinning potential, to **intravalley oscillations**,[42] where the vortices move individually and the motion is dominantly confined within the random pinning potential well. Here we will consider the implications of such a picture for practical devices expected to operate at rf and microwave frequencies.

The lack of a theory for the finite frequency response of both the vortex glass and vortex liquid states away from the glass-to-liquid transition makes it difficult to accurately predict the response of a device operated in these regions of phase space. Our results indicate that one must go to high frequencies (> 10 GHz for the temperatures and field strengths investigated here) before the details of the pinning potential and vortex viscosity become more relevant. It is therefore necessary to further study the ac response, particularly of the vortex glass state, to better predict the behavior of a practical device operated in this (large) region of the B-T phase diagram.

Note that the scaling theory predicts the behavior of $\rho(\omega)$ at the vortex glass-to-liquid transition will be universal, independent of the microscopic details of the system, so that there is little one can do experimentally to engineer the vortex behavior at the glass-to-liquid transition. However, if one wants highly reproducible surface impedance properties in a magnetic field, the vortex glass-to-liquid transition is very attractive. To take advantage of this, one can design a non-reciprocal device to operate at a magnetic field strength and temperature which is near, but just below, the vortex glass-to-liquid transition.

The complicated mixed state response of the high $T_c$ superconductors has many other consequences for applications. The existence of a "melting" transition well below the upper critical field imposes additional design constraints for high $T_c$ devices. To fully exploit the advantages offered by superconducting materials, such devices should be operated below the "melting" line $H_m(T)$ shown in Fig. 6.2. Therefore, for both dc and rf/microwave devices, it is important to maximize the pinning strength of the material, in order to push the melting line $H_m(T)$ to the highest possible fields and temperatures.

The existence of a "depinning frequency" also implies a maximum operable frequency for an ac device at a given field and temperature. The mean-field

expression[4] for $f_{depin} = 1/\tau \sim \kappa_p/\eta$ shows that increasing the strength of the pinning also helps to increase the "depinning frequency." Above this frequency the pinning strength of the material becomes less and less important, and materials controls lose their effectiveness.

In summary, understanding the behavior of vortices in high $T_c$ superconductors at rf and microwave frequencies is necessary for the development and operation of many practical high $T_c$ devices. To that end, we have shown experimental evidence for a crossover in the frequency response of the mixed state of the high $T_c$ superconductor YBCO from a low-frequency regime that can be described by vortex glass/liquid models to a high frequency regime which can be well described by mean-field models. Such experimental results provide important insights into the power dependence and non-linearities of high $T_c$ microwave and rf devices, which helps to remove these barriers to the more widespread application of high $T_c$ superconductivity at rf and microwave frequencies.

## Chapter 6 References


[1] G. Blatter, M.V. Feigel'man, V.B. Geshkenbein, A.I. Larkin, and V.M. Vinokur, Rev. Mod. Phys **66**, 1147 (1994).

[2] D.S. Fisher, M.P.A. Fisher, and D.A.Huse, Phys. Rev. B **43**, 130 (1991).

[3] J.I. Gittleman and B. Rosenblum, Phys. Rev. Lett. **16**, 734 (1966); J. I. Gittleman and B. Rosenblum, J. Appl. Phys. **39**, 2617 (1968).

[4] M.W. Coffey and J.R. Clem, Phys. Rev. Lett. **67**, 386 (1991).

[5] T.C. Hsu, Physica C **213**, 305 (1993).

[6] M. Golosovsky, M. Tsindlekht, and D. Davidov, "High-Frequency Vortex Dynamics in $YBa_2Cu_3O_7$," to appear in Superconductor Science and Technology.

[7] C. C. Chin, D. E. Oates, G. Dresselhaus, M. S. Dresselhaus, Phys. Rev. B **45**, 4788 (1992).

[8] A. Fathy, E. Denlinger, D. Kalokitis, V. Pendrick, H. Johnson, A. Pique, K. S. Harshavardhan, E. Belohoubek, 1995 IEEE MTT-S Symposium Digest **1**, 195 (1995).

[9] D.H. Wu, J.C. Booth, and S.M. Anlage, Phys. Rev. Lett. **75**, 525 (1995).

[10] The upper critical field is approximated as $H_{c2}(T) = 1.65(T_c-T)$, while the melting line is approximated by $H_m(T) =[ T_c (-dH_{c2}/dT)] A [1-T/T_c]^2/\{1 + [1+B (1-T/T_c)]^{1/2}\}^2$, with A=8 and B = 1, and $H_{c2}$ given above, and with $T_c = 90$ K (see reference Farrel).

[11] For a much more thorough discussion of melting and the vortex liquid-to-solid transformation, see D. E. Farrell in "Physical Properties of High Temperature Superconductors IV", D. M. Ginsberg, Ed. (World Scientific, Singapore,1994), p. 7.

[12] R. H. Koch, V. Foglietti, W. J. Gallagher, G. Koren, A. Gupta, and M. P. A. Fisher, Phys. Rev. Lett. **63**, 1511 (1989).

[13] P.L. Gammel, L.F. Schneemeyer, and D.J. Bishop, Phys. Rev. Lett. **66**, 953 (1991).

[14] N.C. Yeh, W. Jiang, D.S. Reed, U. Kripliani, and F. Holtzberg, Phys. Rev. B **47**, 6146 (1993).

[15] W. Jiang, N.-C. Yeh, D.S. Reed, U. Kriplani, T.A. Tombrello, A.P. Rice, and F. Holtzberg, Phys. Rev. B **47**, 8083 (1993).

[16] L. Hou, J. Deak, P. Metcalf, and M. McElfresh, Phys. Rev. B **50**, 7226 (1994).

[17] D.G. Xenikos, J.-T. Kim, T.R. Lemberger, Phys. Rev. B **48**, 7742 (1993).

[18] P.J.M. Woltgens, C. Kekker, J. Swuste, and J.W. de Wijn, Phys. Rev. B **48**, 16 826 (1993).

[19] Y. Ando, J. Kubota, S. Tanaka, Phys. Rev. Lett. **69**, 2851 (1992).

[20] H. Yamasaki, K. Endo, S. Kosaka, M. Umeda, S Yoshida, and K. Kajimura, Phys. Rev. B **50**, 12 959 (1994).

[21] H. Safar, P.L. Gammel, D.J. Bishop, D.B. Mitzi, and A. Kapitulnik, Phys. Rev. Lett. **68**, 2672 (1992).

[22] N.-C. Yeh, D.S. Reed, W. Jiang, U. Kriplani, C.C. Tsuei, C.C. Chi, and F. Holtzberg, Phys. Rev. Lett. **71**, 4043 (1993).

[23] H. K. Olsson, R. H. Koch, W. Eidelloth, and R. P. Robertazzi, Phys. Rev. Lett. **66**, 2661 (1991).

[24] J. Deak, M. McElfreah, R. Muenchausen, S. Foltyn, and R. Dye, Phys. Rev. B **48**, 1337 (1993).

[25] H. Wu, N. P. Ong, and Y. Q. Li, Phys. Rev. Lett. **71**, 2462 (1993).

[26] J. Kotzler, M. Kaufmann, G. Nakielski, R. Behr, and W. Assmus, Phys. Rev. Lett. **72**, 2081 (1994).

[27] D.S. Reed, N.-C. Yeh, W. Jiang, U. Kripliani and F. Holtzberg, Phys. Rev. B **47**, 6150 (1993).

[28] Y. Ando, J. Kubota, Y. Sato, and I. Terasaki, Phys. Rev. B **50**, 9680 (1994).

[29] N. Belk, D.E. Oates, D.A. Feld, G. Dresselhaus, and M.S. Dresselhaus, Phys. Rev. B **53**, 3459 (1996).

[30] J. Owliaei, S. Sridhar, and J. Talvacchio, Phys. Rev. Lett. **69**, 3366 (1992).

[31] M. S. Pambianchi, D. H. Wu, L. Ganapathi, and S. M. Anlage, IEEE Trans. Appl. Supercond. **3**, 2774 (1993).

[32] M. Golosovsky, M. Tsindlekht, H. Chayet, and D. Davidov, Phys. Rev. **B** 50, 470 (1994).

[33] B.A. Willemsen, S. Sridhar, J.S. Derov, and J. H. Silva, Appl. Phys. Lett. **67**, 551 (1995).

[34] S. Revenaz, D.E. Oates, D. Labbe-Lavigne, G. Dresselhaus, and M. Dresselhaus, Phys. Rev. B **50**, 1178 (1994).

[35] S. Ghosh, L.F. Cohen, J.C. Gallop, A.D. Caplin, and R. Somekh, Physica C **235-240**, 3157 (1994).

[36] D.C. Morgan, K. Zhang, D.A. Bonn, R, Liang, W.N. Hardy, C. Kallin and A.J. Berlinsky, Physica C **235-240**, 2015 (1994).

[37] P. Xavier, O. Buisson and J. Richard, Physica C **235-240**, 3229 (1994).

[38] Y. Matsuda, N.P. Ong, Y.F. Yan, J.M. Harris, and J.B. Peterson, Phys. Rev. B **49**, 4380 (1994).

[39] D. H. Wu and S.Sridhar, Phys. Rev. Lett. **65**, 2074 (1990).

[40] B. Parks, S. Spielman, J. Orenstein, D. T. Nemeth, F. Ludwig, J. Clarke, P. Merchant, D. J. Lew, Phys. Rev. Lett. **74**, 3265 (1995).

[41] E.-J. Choi, H.-T. S. Lihn, H. D. Drew, and T. C. Hsu, Phys. Rev. B **49**, 13271.

[42] V. B. Geshkenbein, V. M. Vinokur, R. Fehrenbacher, Phys. Rev. B **43**, 3748 (1991).

# Chapter 7
# Conclusions and Future Work

## 7.1. Results and Conclusions

We have described in this work the successful development and implementation of a unique broadband experimental tool capable of measuring the surface impedance of a variety of materials over the unusually wide microwave frequency range of 45 MHz - 50 GHz. In order to utilize this experimental method to study the response of superconducting thin films we have developed a novel low-temperature calibration scheme that has been employed to accurately calibrate our measurement system from 45 MHz - 50 GHz over temperatures from 4.2 - 300 K. In order to understand quantitatively the frequency response of the samples studied, a mathematical model of a coaxial to circular waveguide transition was developed, which was used to simulate the effect of stray fields in the actual experimental geometry, and which also showed promise as a means to determine dielectric properties of materials over a wide frequency range.

A number of physical systems have proven to be very interesting to study using this frequency-dependent technique. We have applied the Corbino reflection technique to examine the effect of thermal fluctuations on the microwave conductivity at the superconducting phase transition in zero magnetic field in thin films of the high $T_c$ superconductor YBCO. We find that at a specific temperature the magnitude of the fluctuation contribution to the ac conductivity is a pure power law in frequency, and that the phase of the fluctuation conductivity is independent of frequency, throughout three decades in frequency. This is consistent with the predictions of general conductivity scaling theories for $\sigma^{fl}(\omega)$ at $T=T_c$. We have used this information to locate the thermodynamic critical temperature of our samples, and also to extract a

measure of the dynamical critical exponent z, which is found to be in the range z=2.35-3.0 for the thin film samples studied here. This is significantly larger than the value of z=2 calculated in the Gaussian treatment of fluctuation conductivity based on time-dependent Ginsburg-Landau theory. We also find that at temperatures within 1-2 K of $T_c$ both the magnitude and phase of the fluctuation conductivity exhibit scaling behavior in the frequency dependence, with critical exponents given by $z = 2.35 - 3.0$ and $\nu = 1.0\text{-}1.5$. These results together describe a lifetime $\tau^{fl}$ of fluctuations above $T_c$ that diverges much more quickly than predicted by Gaussian theory as the transition temperature is approached from above. In addition, the scaling behavior allows for the experimental determination of the magnitude and phase of the universal scaling function, which is found to be qualitatively similar to the Gaussian function, but with quantitative differences in the limit of large argument. We believe that this work represents the first observation of the critical slowing down of the fluctuation relaxation rate $1/\tau^{fl}$ in the conductivity at the superconducting phase transition in zero magnetic field.

Examination of the temperature dependence of the fluctuation conductivity at different fixed frequencies shows the saturation of the fluctuation conductivity as the fluctuation relaxation rate passes through the measurement frequency. This allows us to directly determine experimentally the temperature dependence of the fluctuation relaxation time, and gives a temperature dependence of $\tau \sim 1/\varepsilon^3$, which is consistent with the divergence of $\tau$ implied by the critical exponents ($\tau \sim 1/\varepsilon^{\nu z} \approx 1/\varepsilon^{(2.35\text{-}3.55)}$), within experimental error. In addition, both the temperature dependence and the frequency dependence of the fluctuation conductivity can be collapsed onto the same universal curve utilizing the critical exponents given above, dramatically illustrating the reduction of two independent variables to one that is accomplished with the scaling hypotheses.

The effects of sample inhomogeneity and disorder on the fluctuation effects have been investigated by examining the temperature dependence of the fluctuation conductivity of samples of differing quality as determined by high resolution x ray diffraction. It is found that the fluctuation conductivity of different quality thin films and also of a single crystal can all be described with the same universal functions and exponents described above, with systematic differences only in the non-universal quantities $\tau_0$ and $\xi_0$.

A second system that has been studied in detail using the frequency dependent Corbino reflection technique is the mixed state in YBCO thin films at high temperatures and magnetic fields. It is found that for a range of temperatures and fields, the response of the magnetic vortices depends sensitively on the frequency of the driving signal. In the region of the mixed state near the vortex liquid to glass transition, our swept-frequency measurements confirm that (below a characteristic frequency) the response of the vortex system can be well described by scaling theories based on the liquid to glass phase transition, which explicitly take into account vortex-vortex interactions. At frequencies above a cross-over frequency $f_x$, however, the experimental data is more successfully described by conventional single-particle (or mean-field) theories of vortex motion, which ignore inter-vortex interactions. We attribute this change in character of the frequency dependent response to a crossover from intervalley vortex oscillations to intravalley oscillations as the probing time scale becomes shorter.

In the mean-field region, we are able to extract the parameters that govern the dynamics of the vortex motion (the viscosity coefficient $\eta$, the pinning force constant $\kappa_p$, and the the diffusion barrier $U_0/k_BT$) directly from our frequency dependent measurements. From complementary magnetic-field dependent measurements, the effectiveness of pinning appears to decrease with increasing frequency. In addition,

the vortex motion parameters that we extract from the high-frequency magnetic field dependent measurements agree well with other experimental determinations, and also agree well with the parameters extracted from the frequency dependent measurements. Our frequency-dependent measurements therefore serve to connect two seemingly contradictory sets of experimental results on vortex motion, and also elucidate an important new characteristic time scale ($1/f_x$).

## 7.2. Technological Implications

In addition to addressing fundamental physical questions, understanding the behavior of vortices in high $T_c$ superconductors at rf and microwave frequencies is necessary for the development and operation of many practical high $T_c$ devices. Much of the B-T parameter space investigated is an inherently non-linear region, where the electrodynamic response of the superconductor depends strongly on the magnitude of the driving current. It is likely that at least some of the power dependent properties and non-linearity observed in the high $T_c$ materials at microwave frequencies can be attributable directly to vortex motion. To that end, our experimental results on vortex motion at microwave frequencies provide important insights into the cause of non-linearities in high $T_c$ based microwave and rf devices, and contribute to the elimination of these barriers to the more widespread application of superconductivity at rf and microwave frequencies.

## 7.3. Further Experiments

The work described in this thesis is by no means an exhaustive treatment of the frequency dependence of the surface impedance of high $T_c$ superconductors. There remain a large number of fundamentally and practically important questions to be answered in regard to the high temperature superconductors and their electrodynamic

response at microwave frequencies. Just a few obvious extensions of this work are given below.

An extension of the measurement technique itself can be accomplished by utilizing additional source(s) in order to measure the surface impedance at lower frequencies. As mentioned previously, the TEM mode can be used at frequencies all the way down to dc, so that extremely broadband measurements are in theory possible. Such measurements in practice may be easier to implement in a transmission, rather than reflection, geometry.

One obvious question raised by this work is regarding the universality of the scaling behavior of the fluctuation conductivity in the high $T_c$ superconductors. A systematic experimental investigation of different high $T_c$ superconducting materials (NCCO, YPrBaCuO, for example) would go a long way to establishing the universality of the scaling functions and exponents, and also toward establishing to which universality class the high $T_c$ superconductors belong. Another fruitful avenue of research would be to study the effect of increasing disorder on the fluctuation properties, and to draw parallels with previous work on fluctuations in disordered systems in liquid helium.[1] In addition, the ability to manufacture single unit cell and multilayer samples provides another excellent opportunity to study fluctuation effects in reduced dimensionality, because fluctuation effects should be larger in lower-dimensional systems. In systems of reduced dimensionality this technique could also be used to study the frequency dependence at the Kosterlitz-Thouless transition.

Another obvious extension of the work presented here is to study fluctuation effects in magnetic fields. It would be extremely interesting to see how the critical exponents and scaling functions that are measured in zero magnetic field are modified as a magnetic field is applied. The subject of fluctuations in a magnetic field is to some degree a more complicated problem than fluctuations in zero magnetic field investigated

here, but the importance of fluctuations in understanding the properties of the high $T_c$ materials is only just beginning to be appreciated. Frequency dependent measurements could also provide information about the value of $H_{c2}(T)$ in the high $T_c$ materials.

A more practically-oriented extension of this work is to studies of the vortex state in the high $T_c$ superconductors. The ability of the Corbino reflection technique to mix ac and dc driving currents of variable magnitude, along with ac and dc measurements, makes the technique extremely useful for studying pinning effects at microwave frequencies, since many current and future high $T_c$ devices will need to operate in modest to high magnetic fields. By varying the dc bias current, the rf current density, and the rf frequency one can effectively map out the form of the pinning potential in the high $T_c$ materials. Also, it has been shown that a dc bias current can depin the vortex lattice in YBCO, making it possible to measure the high frequency response of vortices in the limit of zero pinning.[2] In addition, the ability to make measurements as a function of absolute power means that this technique could be very useful in studying non-linear properties of the vortex state.

## Chapter 7 References


[1] P.C. Hohenberg and B.I. Halperin, Rev. Mod. Phys. **49**, 435 (1977).

[2] J.M. Harris, Y.F. Yan, O.K.C. Tsui, Y. Matsuda, and N.P. Ong, Phys. Rev. Lett. **73**, 1711 (1994).